Instability of Unidirectional Fiber Composites in Compression

by Jens Lycke Wind

Instability of Unidirectional Fiber Composites in Compression

Instability of Unidirectional Fiber Composites in Compression

PhD Thesis by

Jens Lycke Wind

Aarhus University Department of Engineering, Denmark

AARHUS
UNIVERSITY
DEPARTMENT OF ENGINEERING

River Publishers

Contents

Abstract

Plastic microbuckling, also called kink band formation, in unidirectional fiber composites is addressed. An individual fiber and matrix 2D finite element model is built and compared to a 2D composite constitutive model on a square geometry. Comparison is made on the applied stress, fiber angle and kink band angle, and a good correlation between the models is seen. Expanding the height to get larger slenderness of the geometry will introduce the opportunity of Euler buckling as well. This is done in a parametric study where the competing failure mechanisms are observed. The prediction of the critical load of a single-edge notch carbon fiber reinforced epoxy composite beam is addressed as well. The superelement technique is used to reduce analysis time. A comparison with a compressive crack approach is made as well, and almost similar results are obtained.

Resumé

Plastisk mikrobuling, også kaldet kinkbåndsformation, i enakset fiberkomposit er behandlet. En individuel fiber og matrix 2D finite element model er bygget og sammenlignet med med en 2D konstitutiv model anvendt på en kvadratisk geometri. Sammenligningen er lavet med påtrykt spænding, fibervinkel og kinkbåndsvinkel. En god sammenhæng er set mellem modellerne. Hvis højden af geometrien udvides, hvorved et større slankhedsforhold opnåes, introduceres muligheden for søjlebuling, også kaldet Eulerbuling. Dette er udført i et parameterstudie, hvor de to konkurrerende fejlmekanismer optræder. Forudsigelsen af den kritiske last i en kærvpårvirket kulfiberforstærket epoxykompositbjælke er også behandlet. Superelementteknikken er anvendt for at spare beregningstid. En sammenligning med kompressionsrevneteknikken er udført, og virkelig lovende resultater er opnået.

Preface

This thesis summarizes the work done during the PhD project period from August 2011 to November 2014 at Aarhus University, Department of Engineering. The thesis is written as a monograph but the publications are attached as well. It is a combination of theoretical work and experimental observations. The experiments were done at a visit to University of Michigan, Aerospace Engineering from August 2013 to December 2013.

I am very grateful to many people that I have worked with during the PhD period. First of all I would like to thank my supervisor Henrik Myhre Jensen who has been a great mentor to me. The collaboration has been really great and I look forward continuing this in the future. Next I want to thank Anthony M. Waas who was my supervisor at the stay in Ann Arbor at University of Michigan. I am very thankful that I got the opportunity to work with him. At the same time I want to thank the Waas research group who helped me a lot. A special thanks should go to Sölver Thorsson who helped me conduct all the experiments and spent a lot of time with me in the lab. I would also like to thank Brian Justusson and Pascal Meyer for daily correspondence and help with various problems.

My office colleges at the Department of Engineering in Aarhus need great thanks as well. Especially thanks to Mads Krabbe, Per Hyldahl and Søren Steffensen for a great daily life both technical as well as social.

Last I also want to thank my fiancée Karen for great support and understanding when I got stuck in problems.

Aarhus, November 6, 2014

Jens Lycke Wind

List of publications

Publication I
Wind, J. L., Steffensen, S., Jensen, H. M., 2014. Comparison of a composite model and an individually fiber and matrix discretized model for kink band formation. International Journal of Non-linear mechanics 67 (December), 319-325.

Publication II
Wind, J. L., Waas, A. M., Jensen, H. M. Initiation of failure at notches in unidirectional fiber composites. Submitted to Composite Structures.

Publication III
Wind, J. L., Jensen H. M. Imperfection sensitivity in Euler buckling and kink band formation for unidirectional composites. Under preparation.

List of symbols

Definitions

$(\ )_{,1}$	Differentiated with respect to 1
$(\ \dot{)}$	Incremental indicator
$(\ )^c$	Composite indicator
$(\ )^m$	Matrix indicator
$(\ )^f$	Fiber indicator
$(\ )^{cr}$	Critical value
$(\ )_E$	Value from experiments
$(\ )_A$	Value from analyses

Lower case letters

a	Remaining width of beam
b	Width of kink band
d	Cut width
d^f	Diameter of fiber
d^m	Width of matrix
g^*	Determinant of deformed metric tensor
h	Amplitude of imperfection
k	Offset from center axis
n	Hardening index
n^f	Number of fibers
n_i	Unit normal of kink band coordinates
n_i'	Unit normal of base material coordinates
s_{ij}	Deviatoric stress tensor
$\boldsymbol{s}_i$	Vectors of nominal stresses
t	Thickness of beam
t_i	Unit tangent of kink band coordinates
t_i'	Unit tangent of base material coordinates
$v_{k,l}$	Gradients of displacement rates
$\boldsymbol{v}$	Vector of displacements

Upper case letters

A	Area of model
C_{ijkl}	Tensor of nominal moduli
E	Young's modules
E_t	Tangent modulus
E_s	Secant modulus
E_{11}	Young's modulus in the 1 direction
E_{22}	Young's modulus in the 2 direction
F	Applied force
F_C	Contact force
G_{12}	Shear modulus in the 12 direction
G	Shear modulus of composite
G^*	Determinant of deformed metric tensor
G_{ij}	Metric tensor of deformed configuration
G_I	Mode I energy release rate
J_2	Second deviatoric stress invariant
K_I	Mode I stress intensity factor
L	Length of beam
L_{ijkl}	Constitutive tensor
L_0	Initial length of model
U	Displacement
W	Width of beam
W_0	Initial width of model

Greek letters

α	Parameter used for decaying function
β	Angle of kink band
β^*	Yield indicator
γ_m	Critical wave number
γ^y	Shear yield strain
δ	End shortening
δ_{ij}	Kronecker delta
$\delta\xi$	Load factor increment

$\delta\boldsymbol{u}$	Displacement vector of sub-increment
$\delta\boldsymbol{f}$	Force vector of sub-increment
$\delta\boldsymbol{u}_r$	Residual displacement vector of sub-increment
$\Delta\boldsymbol{u}$	Displacement vector of increment
$\Delta\boldsymbol{f}$	Force vector of increment
$\Delta\boldsymbol{u}_1$	Initial displacement vector of increment
ε_{ij}	Strain tensor
ζ	Parameter used for decaying function
θ	Cut angle
λ	Slenderness ratio
ν	Poisson's ratio
ν_{12}	Poisson's ratio in the 12 direction
ρ	Notch tip radius
σ_c	Critical compressive stress
σ_e	Equivalent von Mises stress
σ^y	Yield stress
σ_{ij}	Stress tensor
σ_{max}	Maximum stress at notch tip
σ_{11}^{Euler}	Euler buckling stress
τ^y	Shear yield stress
τ_{ij}	Kirchhoff stress tensor
$\hat{\tau}_{ij}$	Jaumann rate of Kirchhoff stresses
ϕ_0	Initial fiber misalignment angle

Introduction

In the design of mechanical structures it is in most cases desirable to have light and strong structures. One opportunity for meeting this need is the use of a lightweight material like aluminum, but another option is the use of composite materials. Some classical examples where fiber composites are used are shown in Fig. 1.1.

The demand for fiber composite is a growing business. In Fig. 1.2 the use of composite in aircrafts is shown. The same tendency is seen in other industries as well. The wind turbine industry is another example. But what to do when, for example, a wind turbine blade is retiring? How about reuse or proper waste handling? These questions have encouraged the use of biological materials. In nature, composite materials are often seen in wood or flax where evolution has shaped and optimized the materials. In Fig. 1.3 two other types of fiber composites are shown. In the review paper by Faruk et al. (2012) they made a collection of the material specification on the most commonly utilized natural fibers and biopolymers. Since the materials are biological, other characteristics need to be taken into account like cellulose contents.

One of the composite material options is to apply layered materials where the lay-up usually is made of materials with different stiffnesses. Each layer, called ply or lamina, is made of a matrix material reinforced by
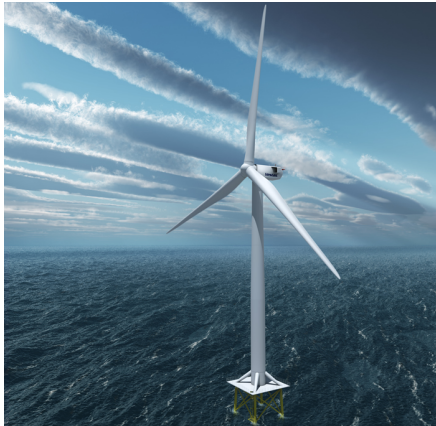
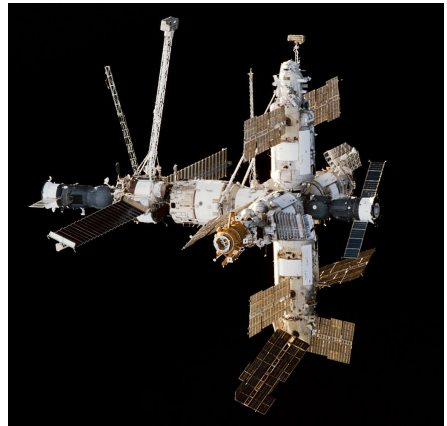**Figure 1.1:** Examples of the use of fiber composites. The BMW i8 (a), the 787 Dreamliner from Boeing (b), the V164 from Vestas (c) and the international spacestation MIR (d).

a stiffer material which together represent a laminate. The reinforcement could be long continuous fibers in which the direction of orientation is crucial for the stiffness of the ply. This means that the fibers can be orientated in a given direction where the high stiffness is wanted.

Woven composite is widely used as well. This produces a strong mechan-
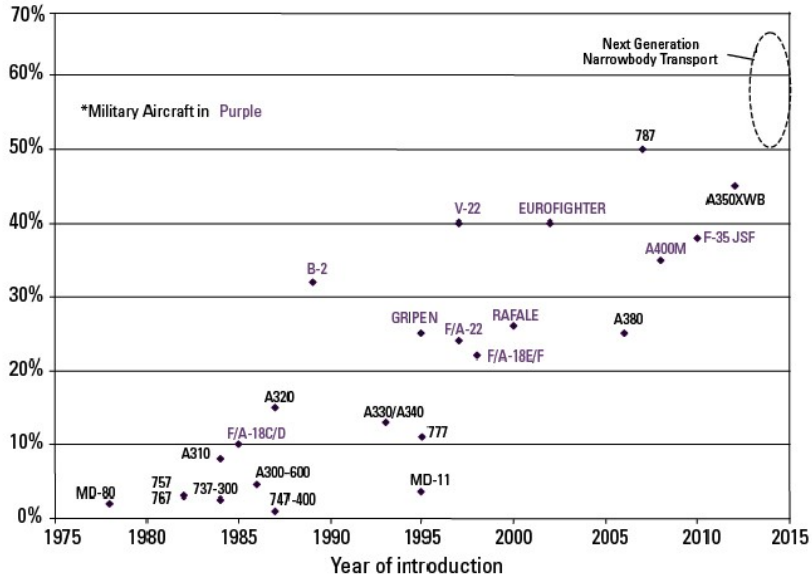
Figure 1.2: Use of composite materials in aircrafts shown as percentage of weight. Source is ATSB.

(a)   (b)

Figure 1.3: Examples of biocomposites. A coconut and bamboo.

ical interlocking of the fibers. Fabrics are woven using the same techniques as in the textile industry in which many different weave styles are adopted. When draping is a problem in complex 3D geometry, weaving the fabric in another way can help solve this problem.

There are many ways of handling the problem of mixing the matrix with the fibers. One way is to use a so-called pre-preg which is a composite where the matrix is embedded and semi-cured prehand of the lay-up. Another approach is to use dry fibers in the lay-up and then use a technique such as injection molding to embed the fibers in the matrix. If a pure unidirectional composite with a constant cross section is wanted, a method called pultrusion could by applied.

A sandwich structure is another way of using composite materials. This type of composite is mostly used where a high bending stiffness is wanted. The sandwich structure principle is to have a lightweight core in a sandwich between fiber composite laminates. This offsetting the stiff laminates from the center axis of the structure increases the bending moment of inertia highly.

Another use of fibers is to chop them up and mix them with the matrix in a random way to produce a reinforced isotropic material. When using chopped up fibers in an injection molding process, for example, the fibers will orientate in the direction of the flow and thereby become stiffer in this direction.

1.1   Unidirectional fiber composite

In many structural components, laminates include one or more plies with fibers located in the direction of the loading. An example of this is in a wind turbine blade that fundamentally acts like a beam in bending. To reduce deformation of the blade a high stiffness is wanted in the direction of the length. The high stiffness comes with a price when the fibers are in compression. For example, the compressive strength of an epoxy matrix reinforced by unidirectional carbon fibers in the direction of the loading is often less than 60% of the tensile strength (Fleck, 1997).
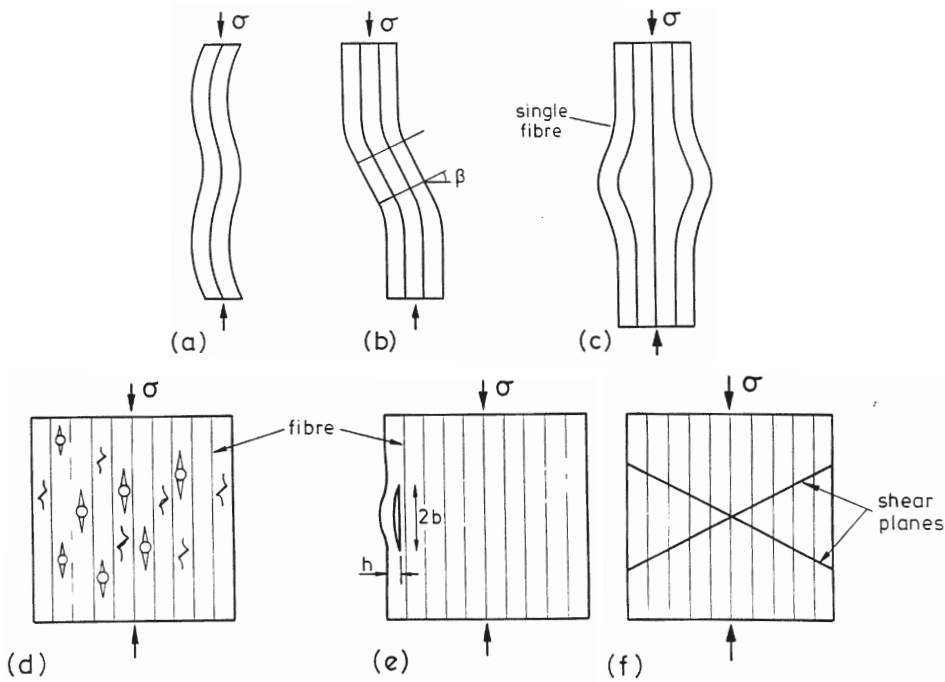
Figure 1.4: Failure modes in unidirectional fiber composite from Fleck (1997).

There are many types of compression mode of failures but the classification is usually made as shown in Fig. 1.4 from Fleck (1997). In Fig. 1.4(a), elastic microbuckling is sketched. Rosen (1965) considered elastic bifurcation of two different modes; a transverse buckling mode and shear buckling mode. Elastic microbuckling is rarely seen in commercial materials like carbon/epoxy composites. Instead plastic microbuckling is the most common compressive failure as sketched in Fig. 1.4(b). A nonlinear response of the matrix is assumed here and will be discussed in section 1.2. In Fig. 1.4(c), the failure mode fiber crushing is shown. This happens when the matrix is sufficiently stiff and strong so that the uniaxial strain reaches the crushing strain of the fibers before any of the other failure modes occur. Another failure mode is splitting, which is shown in Fig 1.4(d). The splitting is seen

as one or more cracks developing in the interface between the fiber and matrix or in the matrix by itself. This failure mode is controlled by the critical stress intensify factor of the matrix. Depending on the loading, the crack can develop as a mode I or a mode II crack. A related failure mode is buckle delamination as seen in Fig. 1.4(e). Hutchinson and Suo (1992) modeled this type of failure as a straight-sided surface layer with infinite extend in the direction transverse to the direction of loading. In Fig. 1.4(f), shear banding is shown. This type of failure is seen in polymer composites with very low fiber volume fractions.

So which type of failure will happen for a given composite? In Fig. 1.5, a 2D failure map is shown with failures indicated for different unidirectional composites exposed to uniaxial compression. On the x-axis, the shear modulus of the composite, G, is used and on the y-axis, the shear yield stress of the matrix, τ^y, normalized with the initial fiber misalignment angle, ϕ_0. From this failure map is is clear that all failures for the given composites
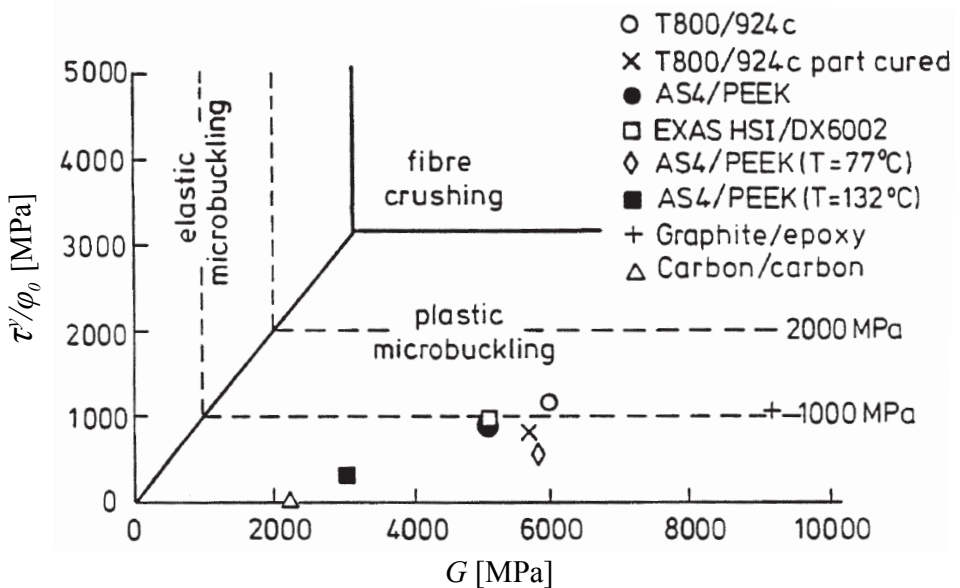

Figure 1.5: 2D failure map from Fleck (1997).

occur as plastic microbuckling. Plastic microbuckling is often seen as the dominant failure mechanism in unidirectional polymer matrix composites. Usually this results in a kink band formation which will be discussed in the next section.

1.2 Plastic microbuckling

Plastic microbuckling is a material instability and results in kink band formation. At the critical stress, i.e. the kinking stress, a narrow band is formed where strains localize which can be seen in Fig. 1.6 for a thermoplastic matrix reinforced by carbon fibers from Vogler and Kyriakides (2001). The phenomenon is seen in different anisotropic materials and was
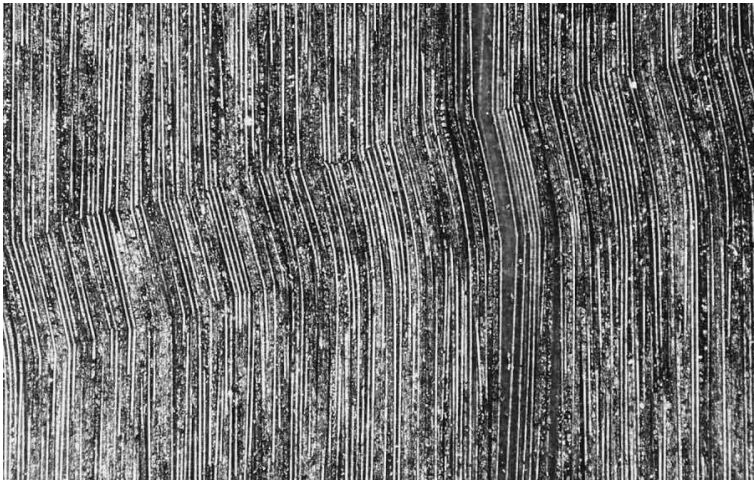

Figure 1.6: Kink band in unidirectional AS4/PEEK.

observed in phyllite by Paterson and Weiss (1966). In the early work on fiber kinking, models were formulated treating the fibers as beams on an elastic foundation. Rosen (1965) suggested a model in which the critical compressive stress, σ_c, for kink band formation is equal to the shear mod-

ulus of the composite, G

$$\sigma_c = G \tag{1.1}$$

which is a linear material formulation. This was not a conservative prediction and experimental results showed σ_c down to 1/4 of the prediction by Rosen. Later Argon (1972) formulated a model for rigid-perfectly plastic matrix using τ^y and ϕ_0 to determine the critical stress as

$$\sigma_c = \frac{\tau^y}{\phi_0} \tag{1.2}$$

Budiansky (1983) incorporated the effect of an elastic-perfectly plastic matrix by use of the shear yield strain of the matrix, γ^y, by

$$\sigma_c = \frac{G}{1 + \phi_0/\gamma^y} \tag{1.3}$$

containing previous results as special cases. In all three predictions, the angle of the kink band, β, is assumed to be zero. It is clear from Fig. 1.6 that this is not the case for a AS4/PEEK composite in unidirectional compression. This will be discussed further in chapter 2.

During the years, several suggestions on more sophisticated modeling of kink band formation have been made. Fleck and Shu (1995) developed a unit cell of a linear elastic Timoshenko beam embedded in a nonlinear elastic-plastic matrix using a couple stress theory. The fiber composite was treated as a smeared-out Cosserat continuum. Christoffersen and Jensen (1996) derived a constitutive model accounting for the microstructure of the composite. Recently Wadee et al. (2012) developed a geometrical kink band model founded on potential energy principles. It was further developed by Zidek and Völlmecke (2014) to include nonlinear material behavior of the matrix.

As suggested by Argon and Budiansky, the fiber misalignment had a big influence on σ_c. These imperfections are introduced during manufacturing and cannot be avoided. Yurgartis (1987) made local measurements of fiber misalignments in continuous fiber composites. He measured the misalignment angle to lie with $\pm 3°$ of the mean fiber direction. A way to reduce the

misalignment is to use the pultrusion technique as discussed earlier. The downside is that usually only a constant cross section can be obtained.

Observing a kink band in a pure compression test can be difficult. When the critical kinking stress is reached, a dramatic load drop will result in a broken specimen in most cases. A way to improve this is to use a non-homogeneous stress field by introducing a notch for example. The stress concentration at the notch tip will force the failure to occur here while there is still load bearing capacity left in the rest of the specimen. Moran and Shih (1998) succeeded in tracking the end-shortening as a function of applied stress in a pure compression setup in a single-edge notched unidi-rectional IM7/PEEK composite. This behavior was similar to that shown by Kyriakides et al. (1995) where they individually modeled the fibers and the matrix in a unidirectional composite using a 2D finite element scheme. Vogler and Kyriakides (2001) managed to observe the same stable phenom-ena in an AS4/PEEK composite in a biaxial test setup. They captured micrographs showing the evolution of the kink band as well.

1.3 Scope of this work

The work in this thesis is divided into three chapters. The first two are build on papers attached where specific parts have been clarified. The last chapter is ongoing work. The first part of this PhD project is introducing an individual fiber and matrix discretized finite element model. The model is built with the intention of making a tool where the constitutive model by Christoffersen and Jensen (1996) can be verified using it in a kink band analysis. Different parameters are used for comparison such as the critical stress, fiber angle and kink band angle.

Next this finite element model is used to predict the failure load of a single-edge notch beam in a four-point bend setup. The prediction is built on experiments made for an epoxy reinforced carbon fiber composite. The hypothesis is that failure occurs as plastic microbuckling, which the finite element model is able to predict. The idea of using a notched beam is to get a non-homogeneous compressive stress state where it is possible to observe

what is actually happening on fiber level in a microscope.

In the last chapter, the transaction from Euler buckling to kink band formation of a composite beam of varying aspect ratio is explored. This means that a parametric study is made using the finite element model varying the width-to-height ratio. The imperfection sensitivity is small in Euler buckling while it is large in kink band formation. The hypothesis is that, in the transition, there is a mixture of the two failure modes which is investigated.

Comparison with a constitutive model

Structural finite element calculations on composite materials on a detailed fiber/matrix level can be attacked from two angles: A detailed discretization of fiber and matrix individually or using a smeared out constitutive model. Making a detailed finite element model of a structure used in practice on the fiber/matrix level will result in a finite element model with a very large number of elements, and in most cases it is not even possible. If the same mechanical behavior with sufficient accuracy can be observed using a smeared out model, that is preferable in most cases. In Fig. 2.1, a sketch of a 2D composite model with a fiber waviness introduced as an imperfection is shown. This figure will be used as a reference in the setup of a constitutive model and in the setup of a detailed finite element model.

In a composite where the stiffness and the yielding stress of the fibers are significantly higher, material nonlinearity of the fibers contributes with a minor effect on the mechanical behavior. It was observed by Christoffersen and Jensen (1996) and Kyriakides et al. (1995) that the critical stress was only slightly affected by nonlinearity in the fibers. The nonlinearity did have an effect on the critical displacement, but the contribution was still small. Due to these findings, it is assumed that only the matrix behaves elastic-
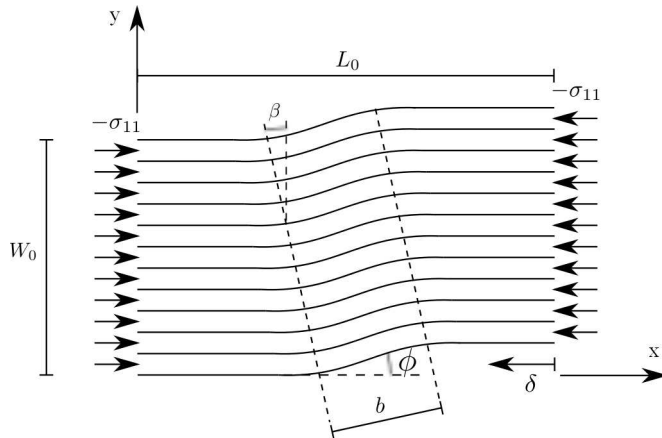
Figure 2.1: Sketch of 2D composite model.

plastic, while the fibers remain isotropic elastic. Many fiber materials are known to have orthotropic material behavior. In a compression scenario in the fiber direction the axial stiffness is of high importance while the radial stiffness is less important. The fiber orthotropic behavior is due to this ignored.

2.1   Constitutive equations

The plasticity of the matrix material is described by the J_2-flow theory with isotropic hardening. The time-independent constitutive tensor L_{ijkl} relating the Jaumann rate of Kirchhoff stresses $\hat{\tau}_{ij}$ to strain rate $\dot{\varepsilon}_{ij}$ is

$$\hat{\tau}_{ij} = L_{ijkl}\dot{\varepsilon}_{kl} \tag{2.1}$$

where the constitutive tensor L_{ijkl} for J_2-flow theory from McMeeking and Rice (1975) using a finite strain formulation (total Lagrangian) as in

Hutchinson (1973) is

$$
\begin{aligned}
L_{ijkl} = & \frac{E}{1+\nu} \left(\frac{1}{2} \left(G_{ik}G_{jl} + G_{il}G_{jk} \right) + \frac{\nu}{1-2\nu} G_{ij}G_{kl} \right. \\
& \left. - \beta^* \frac{3}{2} \frac{E/E_t - 1}{E/E_t - (1-2\nu)/3} \frac{s_{ij}s_{kl}}{\sigma_e^2} \right) \\
& - \frac{1}{2} \left(G_{ik}\tau_{jl} + G_{jk}\tau_{il} + G_{il}\tau_{jk} + G_{jl}\tau_{ik} \right)
\end{aligned}
\tag{2.2}
$$

where G_{ij} are the components of the metric tensor of the deformed configuration, E is the Young modulus of elasticity, ν is Poisson's ratio and E_t is the tangent modulus. s_{ij} are the components of the deviatoric stress tensors and are defined by Kirchhoff stresses τ_{ij} as

$$
s_{ij} = \tau_{ij} - \tfrac{1}{3}G_{ij}G^{kl}\tau_{kl}
\tag{2.3}
$$

σ_e is the equivalent von Mises stress

$$
\sigma_e = \sqrt{\tfrac{3}{2}G^{ik}G^{jl}s_{ij}s_{kl}}
\tag{2.4}
$$

The relation between Kirchhoff and Cauchy stresses is

$$
\sigma_{ij} = \sqrt{\frac{g^*}{G^*}}\tau_{ij}
\tag{2.5}
$$

where g^* and G^* are the determinants of the metric tensor of the undeformed and deformed configuration, respectively. β^* is determined by

$$
\beta^* = \begin{cases} 1 & \text{for } \sigma_e = (\sigma_e)_{\max} \text{ and } \dot{\sigma}_e \geq 0 \\ 0 & \text{for } \sigma_e < (\sigma_e)_{\max} \text{ or } \dot{\sigma}_e < 0 \end{cases}
\tag{2.6}
$$

The relation between the uniaxial logarithmic strain, ε, and the uniaxial Cauchy stress, σ, is described as a Ramberg-Osgood relation for the matrix material by

$$
\varepsilon = \frac{\sigma}{E} + \frac{3\sigma^y}{7E} \left(\frac{\sigma}{\sigma^y} \right)^n
\tag{2.7}
$$

where σ^y is the yield stress and n is the hardening index. The tangent modulus, E_t, is determined by differentiation of (2.7).

2.2   The constitutive model

Christoffersen and Jensen (1996) developed a rate constitutive equation accounting for the microstructure of a 2D unidirectional fiber composite. They treated the problem in the framework of localization of deformation (Rice, 1976). The model allowed for arbitrary elastic-plastic behavior of the constituents. The model was applied in a study of initial fiber misalignments (Jensen and Christoffersen, 1997) and solutions were obtained in a numerical scheme by increasing the fiber angle incrementally and satisfying equilibrium and compatibility across the kink band boundary. An expression is obtained for the composite moduli as a function of constituent moduli and volume fractions by Christoffersen and Jensen (1996). The plane constitutive model is based on continuity and equilibrium across layer interfaces on a constituent level rather that on global composite level. The model is briefly reviewed in this section.

   In the following, superscript c denotes constituents (fiber or matrix) and properties without superscript denote composite properties. Assuming that the fibers are orientated along the x_1 axis (see Fig. 2.1), the constitutive relation between the nominal stress rates $\dot{s}_{ij}$ and the gradients of displacement rates $v_{i,j}$ is

$$\dot{s}^c_{ij} = C^c_{ijkl} v^c_{k,l} \ , \ i,j,k,l \in \{1,2\} \tag{2.8}$$

for the constituents (matrix and fiber individually) where C^c_{ijkl} is the tensor of nominal moduli. With the state of Cauchy stresses σ^c_{ij} of the fiber and matrix assumed known, the constitutive tensor can be expressed as

$$C^c_{ijkl} = L^c_{ijkl} - \tfrac{1}{2}\delta_{il}\sigma^c_{kj} - \tfrac{1}{2}\delta_{ik}\sigma^c_{lj} - \tfrac{1}{2}\sigma^c_{il}\delta_{kj} + \tfrac{1}{2}\sigma^c_{ik}\delta_{lj} \tag{2.9}$$

written in an updated Lagrangian formulation. Symmetry conditions apply for L^c_{ijkl} as

$$L^c_{ijkl} = L^c_{ijlk} = L^c_{jikl} = L^c_{klij} \tag{2.10}$$

Equation (2.8) may for convenience be written as

$$\dot{\boldsymbol{s}}^c_\alpha = \boldsymbol{C}^c_{\alpha\beta} \boldsymbol{v}^c_{,\beta} \ , \ \alpha,\beta \in \{1,2\} \tag{2.11}$$

where the vectors $\dot{\boldsymbol{s}}^c$ denote the rates of nominal stresses by

$$\dot{\boldsymbol{s}}_1^c = \begin{Bmatrix} s_{11}^c \\ s_{12}^c \end{Bmatrix} , \quad \dot{\boldsymbol{s}}_2^c = \begin{Bmatrix} s_{21}^c \\ s_{22}^c \end{Bmatrix} \tag{2.12}$$

and the vector $\boldsymbol{v}^c$ is

$$\boldsymbol{v}^c = \begin{Bmatrix} v_1^c \\ v_2^c \end{Bmatrix} \tag{2.13}$$

The matrix $\boldsymbol{C}_{\alpha\beta}$ is decomposed as

$$\boldsymbol{C}_{11}^c = \begin{bmatrix} L_{1111}^c - \sigma_{11}^c & L_{1112}^c - \sigma_{12}^c \\ L_{1211}^c - \sigma_{12}^c & L_{1212}^c - \frac{\sigma_{22}^c - \sigma_{11}^c}{2} \end{bmatrix},$$

$$\boldsymbol{C}_{12}^c = \begin{bmatrix} L_{1112}^c & L_{1122}^c \\ L_{1212}^c - \frac{\sigma_{22}^c + \sigma_{11}^c}{2} & L_{1222}^c \end{bmatrix},$$

$$\boldsymbol{C}_{21}^c = \begin{bmatrix} L_{1211}^c & L_{1212}^c - \frac{\sigma_{11}^c + \sigma_{22}^c}{2} \\ L_{2211}^c & L_{2212}^c \end{bmatrix},$$

$$\boldsymbol{C}_{22}^c = \begin{bmatrix} L_{1212}^c - \frac{\sigma_{11}^c - \sigma_{22}^c}{2} & L_{1222}^c - \sigma_{12}^c \\ L_{2212}^c - \sigma_{12}^c & L_{2222}^c - \sigma_{22}^c \end{bmatrix} \tag{2.14}$$

Applying the constitutive model comes with a number of assumptions:

(A) Material lines parallel with the fibers are subjected to a common stretching and rotations.

(B) Planes parallel with the fibers transmit identical tractions.

(C) The material of the constituents is elastic or elastic-plastic.

(D) No bending stiffness of the fibers is included.

Assumption (A) corresponds to a Voigt estimate for effective material properties parallel with the fibers. It corresponds to the fact that the displacement gradients $\boldsymbol{v}_{,1}^c$ are common to both constituents

$$\boldsymbol{v}_{,1}^f = \boldsymbol{v}_{,1}^m = \boldsymbol{v}_{,1} \tag{2.15}$$

using the notation $\boldsymbol{v}_{,1}$ without superscript which corresponds to the overall displacement gradient. For overall compatibility of a representative volume element

$$c^f \boldsymbol{v}_{,2}^f + c^m \boldsymbol{v}_{,2}^m = \boldsymbol{v}_{,2} \qquad (2.16)$$

where c^f and c^m are the volume fractions and have the relation

$$c^f + c^m = 1 \qquad (2.17)$$

which may change during deformation as the strains and material properties in the fibers and matrix differ.

Assumption (A) is not realistic perpendicular to the fibers for which reason assumption (B) is imposed which is the Reuss estimate for composites. This means that

$$\dot{\boldsymbol{s}}_2^f = \dot{\boldsymbol{s}}_2^m = \dot{\boldsymbol{s}}_2 \qquad (2.18)$$

and for overall equilibrium

$$c^f \dot{\boldsymbol{s}}_1^f + c^m \dot{\boldsymbol{s}}_1^m = \dot{\boldsymbol{s}} \qquad (2.19)$$

Balances of forces together with assumption B gives us

$$c^f \sigma_{11}^f + c^m \sigma_{11}^m = \sigma_{11} \ , \ \sigma_{12}^f = \sigma_{12}^m = \sigma_{12} \ , \ \sigma_{22}^f = \sigma_{22}^m = \sigma_{22} \qquad (2.20)$$

Assumption (C) indicates that (2.8) and (2.11) are valid. Through combination of (2.11) and (2.15) - (2.20), it is shown by Christoffersen and Jensen (1996) that the overall constitutive equations for the composite can be written as

$$\boldsymbol{C}_{\alpha\beta} = c^f \boldsymbol{C}_{\alpha\beta}^f + c^m \boldsymbol{C}_{\alpha\beta}^m - c^f c^m \left(\boldsymbol{C}_{\alpha2}^f - \boldsymbol{C}_{\alpha2}^m \right) \boldsymbol{C}_{22}^{*\,-1} \left(\boldsymbol{C}_{2\beta}^f - \boldsymbol{C}_{2\beta}^m \right) \qquad (2.21)$$

where $\boldsymbol{C}_{22}^{*\,-1}$ denotes the inverse of the matrix

$$\boldsymbol{C}_{22}^* = c^m \boldsymbol{C}_{22}^f + c^f \boldsymbol{C}_{22}^m \qquad (2.22)$$

The first two terms of (2.21) is the Voigt estimate. The rest of the terms is a correction according to assumption (B) perpendicular to the fibers.

Assumption (D) is implicit in the model as no bending stiffness of the fibers is included. This means that no finite kink band width can be found. The kink band width will be discussed in section 2.3.2.

The equations (2.15) - (2.20) takes care of the continuity between the fiber and matrix. The use of (2.21) in a kink band analysis requires continuity equations between the base material and the kink band (Jensen, 1999). The continuity of displacement gradients across the boundary requires that

$$v'_{i,j}t'_j t'_i = v_{i,j}t_j t_i \qquad v'_{i,j}t'_j n'_i = v_{i,j}t_j n_i \qquad (2.23)$$

where a primed symbol relates to the base material coordinates and an unprimed to the kink band coordinates. t_i, t'_i n_i and n'_i are, respectively, the unit tangent and the unit normal of the boundary between base material and kink band expressed in the base material coordinates and the kink band coordinates. Continuity of traction rates between the two regions requires that

$$\dot{s}'_{ij}n'_i n'_j = \dot{s}_{ij}n_i n_j \qquad \dot{s}'_{ij}n'_i t'_j = \dot{s}_{ij}n_i t_j \qquad (2.24)$$

Note that the kink band analysis using (2.23) and (2.24) is carried out on the overall composite level using (2.21) as constitutive equation.

2.2.1 Implementation in a finite element analysis

Sørensen et al. (2009) implemented the constitutive model in the commercial finite element software ABAQUS. The implementation was done in a user subroutine. In Fig 2.2, a load-displacement curve is shown for different number of elements in the model. As expected, there is a big difference in the postbuckling regime. This is because of the difference in the kink band width shown in Fig. 2.3 which leads to different elastic unloading paths. The kink band width is mainly controlled by the fiber bending stiffness as will be discussed in section 2.3.2. Since there is no bending stiffness included in the constitutive model, the kink band width will not converge. The high mesh dependency comes in because of the only length scale introduced is the size of the mesh. The critical load is converging as more elements are used. If the analysis was continued, it would be expected that
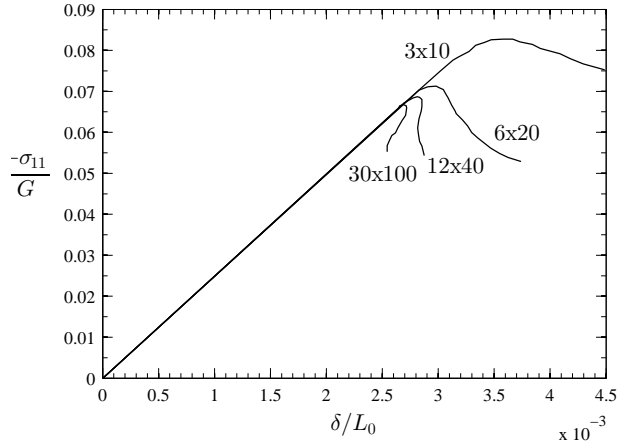
Figure 2.2: Mesh dependency on load path using the constitutive model in a finite element analysis. Results are from Sørensen et al. (2009).
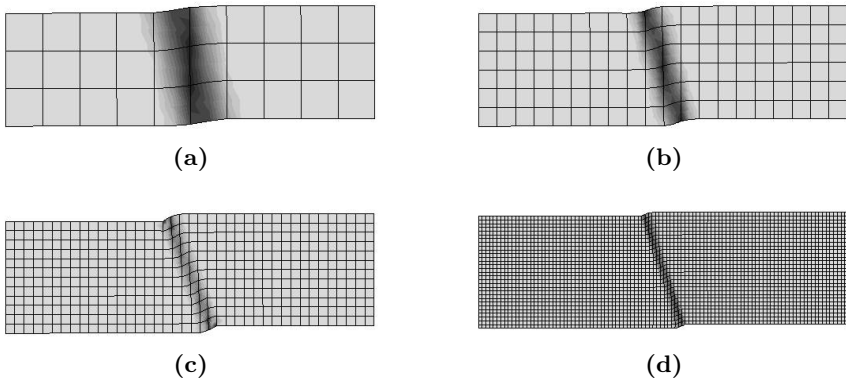

Figure 2.3: Mesh sensitivity on deformations using the constitutive model in a finite element analysis. The darker region indicate plastic strains. Results are from Sørensen et al. (2009).

the different mesh sizes will converge to the same steady state load. This is expected because the steady state load is weakly dependent on the fiber

bending stiffness.

2.3 The detailed finite element model

The finite element model is build in a comparable scheme to Kyriakides et al. (1995). The commercial finite element code Marc from MSC Software is used for the analysis. The numerical scheme is chosen as an updated Lagrangian formulation. The model is build of alternating fiber and matrix layers with one 8 node bi-quadratic plane strain element per individual fiber and matrix layer. The mesh in generated manually using MATLAB and imported into the pre- and postprocessor Marc Mentat from MSC Software. It was observed by Borg (2003) that using 1 element per layer compared to 3 gave a deviation on the kink stress by only 3 %. The grid in Kyriakides et al. (1995) is also made of 1 element per layer.

The imperfection in Fig. 2.1 is to simulate a fiber misalignment and is imposed as a cosine function in the area marked by the dashed lines. The imperfection is imposed as

$$x_2 = \frac{h}{2}\left(1 - cos\left(\frac{\pi x_1}{b}\right)\right) \qquad (2.25)$$

where h is determined from the misalignment angle ϕ_0

$$h = \frac{2b\tan(\phi_0)}{\pi} \qquad (2.26)$$

and b is the width of the imperfection. The angle of the imperfection, β, determines in combination with b the area where the imperfection from (2.25) applies. The fibers outside this area are straight. When $b = L_0$ there are no straight fibers and the misalignment is applied to the whole model. This type of misalignment is referred to as *global* imperfection. When $b < L_0$, the misalignment is referred to as *local* imperfection.

The fiber volume fraction, c^f, is specified in the setup of the model. The matrix volume fraction, c^m, is determined by (2.17). The width, W_0, and the length, L_0, are fixed values in the model. This leads to the fiber

diameter d^f being a variable determined by

$$d^f = \frac{W_0\, c^f}{n^f} \qquad (2.27)$$

where n^f is the number of fibers in the model. The width of the matrix is then

$$d^m = \frac{W_0 - d^f n^f}{n^f - 1} \qquad (2.28)$$

Using (2.27) and (2.28) requires that the outer elements on both sides are fiber elements.

Since this 2D model represents a slice of a 3D composite, the 2D fiber volume fraction and 2D fiber diameter can be determined in different ways. Gutkin et al. (2010) stated three ways:

(i) 2D fiber volume fraction equals 3D; $c^f_{2D} = c^f_{3D}$

(ii) A hexagonal fiber arrangement; $c^f_{2D} = \sqrt{\frac{2\sqrt{3}}{\pi} c^f_{3D}}$

(iii) 2D bending stiffness of the fiber equals 3D; $d^f_{2D} = \left[\frac{12}{64}\pi (d^f_{3D})^4 \right]^{1/3}$

In a τ-σ failure envelope there was not much of a difference between methods (i) and (iii). In method (ii) the results were less conservative. Keeping the same volume fraction and fiber diameter in 2D as in 3D as in method (i) is therefore chosen.

Since the equilibrium path may experience snap-through and snap-back, the numerical technique for incremental solution is chosen as the arc-length method first introduced by Riks (1979). A linear constraint is chosen as described in Krenk (2009) so that the sub-increment $(\delta \boldsymbol{u}, \delta \boldsymbol{f})$ lies in a hyperplane orthogonal to the current total increment $(\Delta \boldsymbol{u}, \Delta \boldsymbol{f})$ and is expressed by the condition

$$(\Delta \boldsymbol{u}, \Delta \boldsymbol{f}) \cdot (\delta \boldsymbol{u}, \delta \boldsymbol{f}) = 0 \qquad (2.29)$$

where $\boldsymbol{u}$ is the displacement vector and $\boldsymbol{f}$ is the force vector. The load factor increment, $\delta\xi$, is calculated as

$$\delta\xi = -\frac{\Delta\boldsymbol{u}^T\delta\boldsymbol{u}_r}{\Delta\boldsymbol{u}^T\Delta\boldsymbol{u}_1} \tag{2.30}$$

where $\delta\boldsymbol{u}_r$ is the sub-increment residual displacement vector and $\Delta\boldsymbol{u}_1$ is the initial displacement vector in the current increment. The edges at $x = 0$ and $x = L_0$ are fixed for rotation.

2.3.1 Kink band process

In Figure 2.4 several different stages at the load-displacement curve is marked. This is to illustrate the deformations. The applied stress, $-\sigma_{11}$, is normalized with the elastic shear modulus, G, of the composite

$$G = \frac{G^m G^f}{\nu^f G^m + \nu^m G^f} \tag{2.31}$$

Stage (0) refers to the initial stage which is shown in Figure 2.1. The deformation stages in connection with Fig. 2.4 are shown in Fig. 2.5. Stage (a) is where the equivalent von Mises stress of the matrix first exceeds the yielding stress. The zone of yielding is shown as plastic strains in the darker region for all the stages. At stage (b), the maximum stress is reached, i.e. the kinking stress. From stage (a) to (b) it is worth noting that the zone of plastic strains becomes smaller even before the kinking stress is reached. It is clear from Figure 2.4 that the load drops dramatically from stage (b) to (c) as well as the current length is increased due to snap-back behavior. This is due to the localization of deformation into a kink band which entails elastic unloading of the fibers outside the kink band. The amount of load drop and snap-back behavior is dependent on the imperfection, the material parameters of the matrix, the size of the specimen, and the bending stiffness of the fibers. In section 2.3.2 the kink band width will be discussed. In stage (c) the deformation is fully localized and the fibers start to rotate more rapidly. As the load keeps dropping from stage (c) to (d), the current length of the model starts increasing again. As the fibers rotate, the kink band

angle, β, will also rotate. This is clear if a comparison is made between stage (c) and stage (f), for example. After stage (f) the load reaches a steady state value and a continuous compression will result in kink band broadening or a possible fiber breakage. Kink band broadening is discussed by Jensen (1999) and Moran et al. (1995).
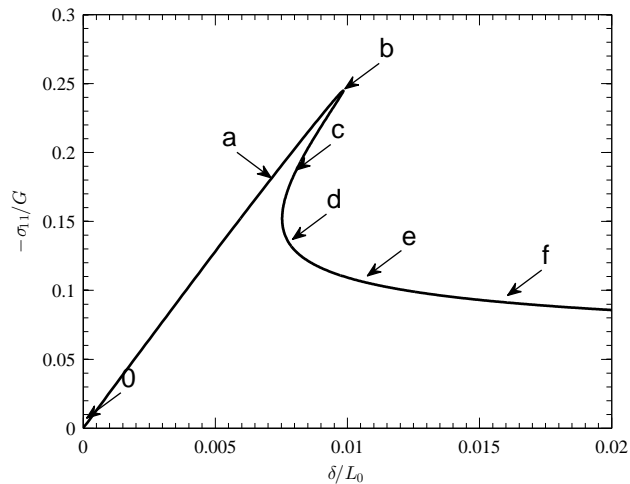

Figure 2.4: Applied normalized stress as a function of normalized end shortening.

2.3.2 Convergence and kink band width

To determine how many fibers are needed in the model to obtain a satisfying result, a convergence study on the number of fibers is made. Since the geometry of the model is fixed as a square with fixed side lengths, changing the number of fibers will change the diameter of the fibers. This will affect the response in different ways and will be outlined next. The data used in this convergence study is shown in Tab. 2.1. The imperfection is imposed as a global imperfection, i.e. $b = L_0$. In Fig. 2.6, the applied stress as a function of end-shortening for a range of fibers from $n^f = 40$ to $n^f = 200$ is shown. In the linear elastic pre-buckling stage from stage (0) to stage (a) there is no difference. A small deviation comes in at the critical stress,
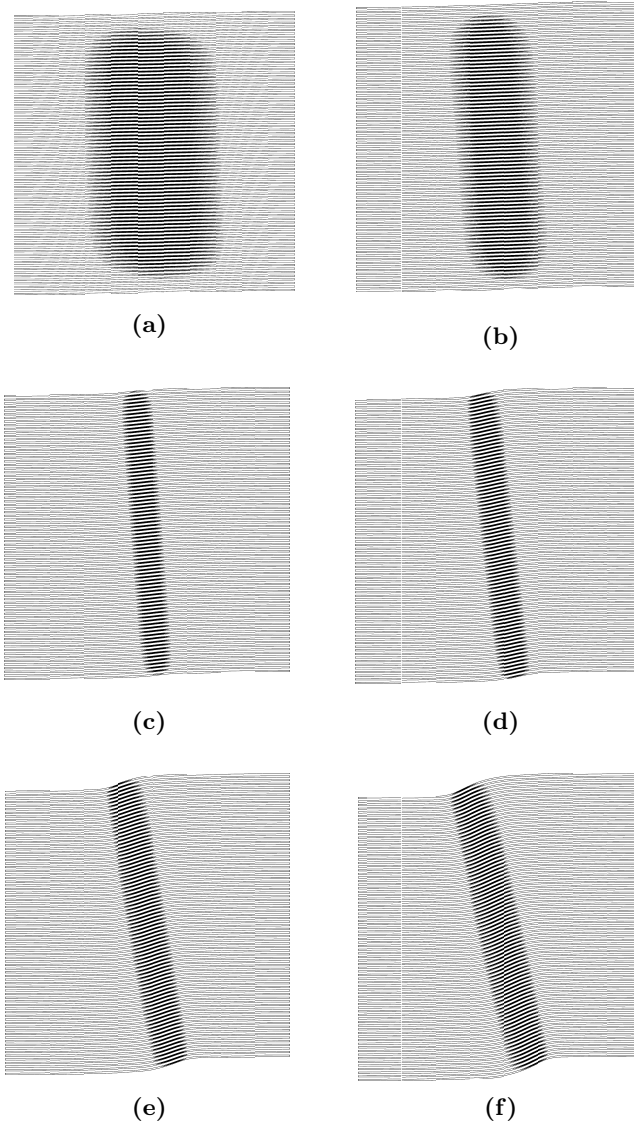
(a)

(b)

(c)

(d)

(e)

(f)

Figure 2.5: Deformation plots at different stages illustrating localization of deformation and rotation of kink band. The darker region indicate plastic strains in the matrix elements. The stages refer to Fig. 2.4.

23

E^f/E^m	35
ν_f	0.263
ν_m	0.356
σ^y/E^m	0.013
n	4
ϕ_0	$1°$

Table 2.1: Parameters used in convergence study.
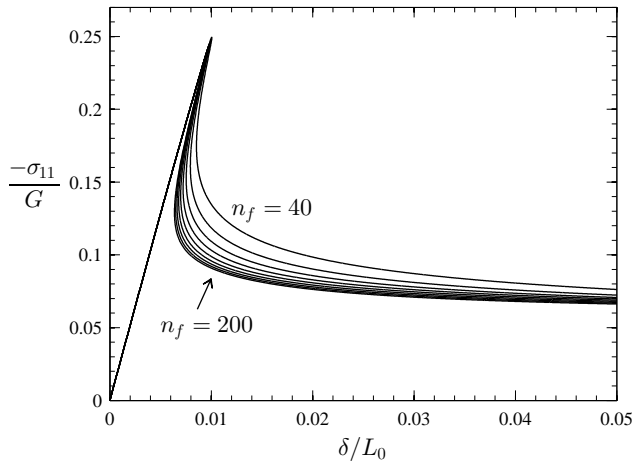
Figure 2.6: Applied stress as a function of end shortening. n^f steps by 20 from $n^f = 40$ to $n^f = 200$.

σ_{11}^{cr}, in stage (b). In Fig. 2.7 it can be observed that changing n^f only has a slight effect on σ_{11}^{cr}. As suggested by Budiansky (1983), the critical stress is mainly dependent on material parameters and the fiber misalignment which support the results in Fig. 2.7. When the critical stress is reached in stage (b), a deviation starts to kick in as the kink band is formed at around stage (c) and elastic unloading of the material outside happens. This can be explained by Fig. 2.8 where σ_{11} is shown as a function of b/L_0. As n^f increases, b decreases. This is because the bending stiffness of the fibers
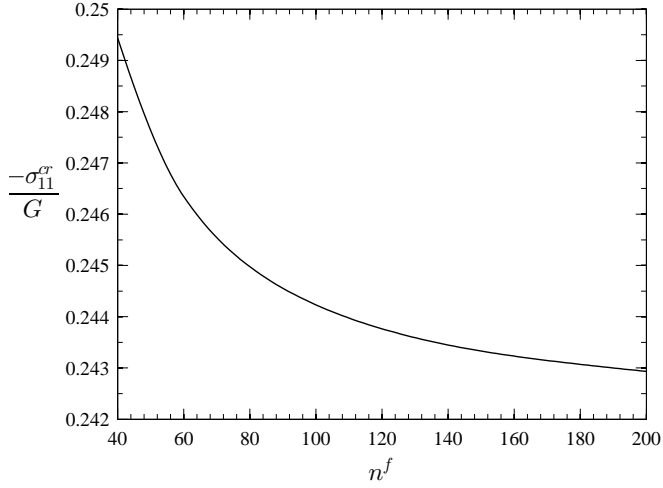
Figure 2.7: Critical applied stress as a function of number of fibers in the model.
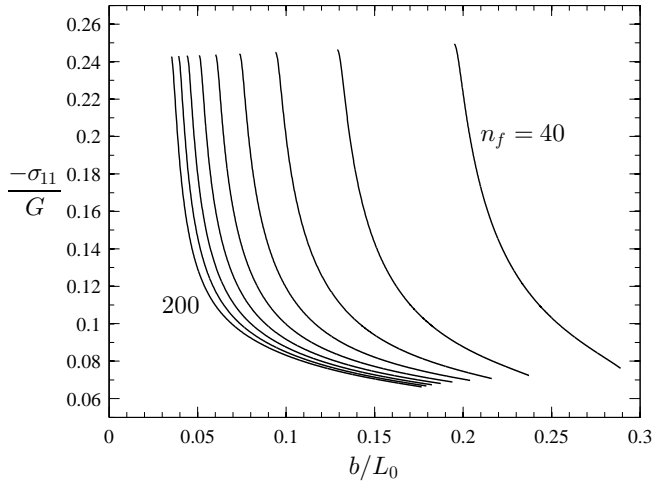

Figure 2.8: Applied stress as a function of kink band width normalized with initial length of model. n^f steps by 20 from $n^f = 40$ to $n^f = 200$.
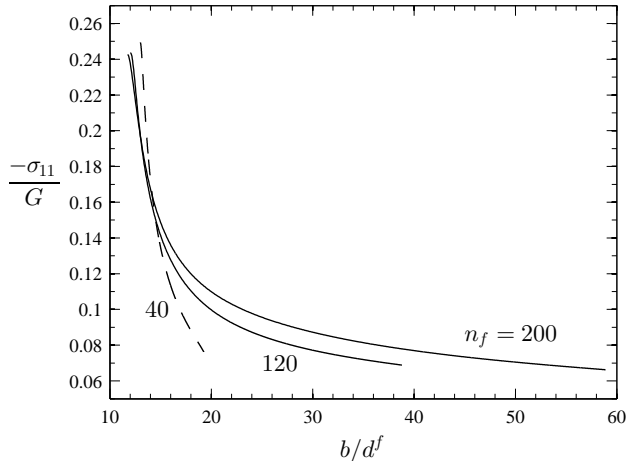
25

Figure 2.9: Applied stress as a function of kink band width. The curve for $n^f = 40$ is dashed for clarity.

decreases as d^f decreases. In Fig. 2.9, b is normalized with d^f instead of L_0. Budiansky (1983) derived an expression for b/d^f for perfectly brittle initially straight fibers and assuming that the matrix is perfectly plastic after the shear yielding stress, τ^y, is reached as

$$\frac{b}{d^f} = \frac{\pi}{4}\left(\frac{2\tau^y}{c^f E^f}\right) \tag{2.32}$$

Calculating τ^y using Von Mises yield criterion

$$\tau^y = \frac{\sigma^y}{\sqrt{3}} \tag{2.33}$$

Using the material parameters from Tab. 2.1 used in this analysis gives a kink width fraction

$$\frac{b}{d^f} = 8.8 \tag{2.34}$$

In Fig. 2.9 it shows that $b/d^f \approx 12.5$ at the initiation of the kink band. This is slightly larger in comparison with (2.34). If using ductile fibers instead

of brittle fibers, a larger b/d^f, as described in Budiansky (1983), would be predicted. This explains why a larger value is found in these analyses where the fibers are not perfectly brittle. Because of the almost identical starting point of b/d^f for varying n^f in Fig. 2.9 it can be concluded that using a simple prediction as (2.32) would give reasonable results for the initiation width of a kink band.

As σ_{11} keeps decreasing rapidly from stage (c), the deviation enlarges until around stage (e). Continuing the load path to stage (f) and further reduces the deviation as the steady state is reached and the kink band broadens. As kink band broadening is happening a deviation in Fig. 2.9 starts to show as well.

In Fig. 2.10 the applied stress is shown as a function of fiber rotation, ϕ. ϕ is measured in the fiber adjacent to $W_0/2$ and in the element at $L_0/2$. In this figure ϕ shows a very weak dependency on n^f.
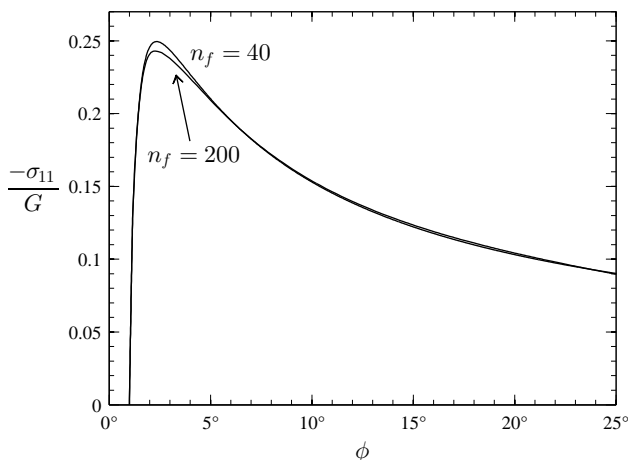

Figure 2.10: Applied normalized stress as a function of fiber rotation, ϕ, for two different number of fibers, $n^f = 40$ and $n^f = 200$. Only two curves are shown because $n^f = 80$ is almost identical to $n^f = 200$, so this is believed to be the converged curve.

27

2.3.3   Kink band angle and fiber rotation

The relation between β and ϕ is shown in Figs. 2.11 and 2.12 for the local and global analysis respectively.   It can be observed in Fig. 2.11 that
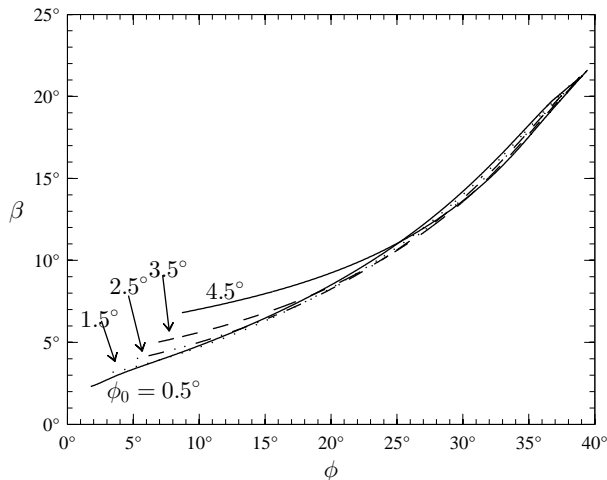

Figure 2.11: Kink band angle, β, as a function of fiber rotation, ϕ, with different initial fiber misalignment for the local analysis.

β rotates with ϕ in a nearly linear manner when $\phi > 20°$ independent of initial fiber misalignment ϕ_0. An approximate relation between β and ϕ has been observed experimentally in different materials to be (Paterson and Weiss, 1966)

$$\phi \approx 2\beta \qquad (2.35)$$

which is in good agreement with Figure 2.11 when $\phi > 20°$. For the global analysis in Fig. 2.12 the same linearity can be observed. The relation in (2.35) thus only seems to apply for small initial fiber misalignment ϕ_0. Usually (2.35) is used as a lock-up condition corresponding to zero volumetric straining of the matrix material (Fleck and Budiansky, 1991).

In the large strain material response of the matrix there is no stiffening incorporated. Stiffening is known to happen for amorphous polymers (e.g.

28

Arruda and Boyce (1993)) when exposed to large strain. With this effect included, the relation between β and ϕ would act differently.

2.4 Comparison

Jensen and Christoffersen (1997) showed that the critical kink band angle β_0^{cr} was not necessarily 0 in contrast to previous theoretical studies. Experimental observations also indicate inclined bands in most cases. This was shown in a $-\sigma_{11}$ vs ϕ plot for initial fiber misalignments angle of $\phi_0 = 0.5°$ and $\phi_0 = 3°$. A comparison with this is made for a global and a local imperfection. The values of β_0 and b for the local imperfection were obtained by the following procedure: The global analysis was conducted, and the point where the kink band has localized, was observed (stage (c) in Fig. 2.4). Then β and b was noted at that stage and used as imperfection values for the local analysis. This means that the equilibrium from the global analysis controls the initial configuration of the local analysis. The com-
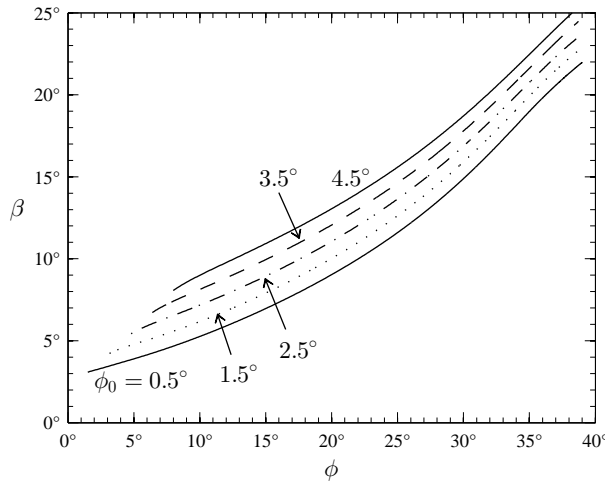

Figure 2.12: Kink band angle, β, as a function of fiber rotation, ϕ, with different initial fiber misalignment for the global analysis .

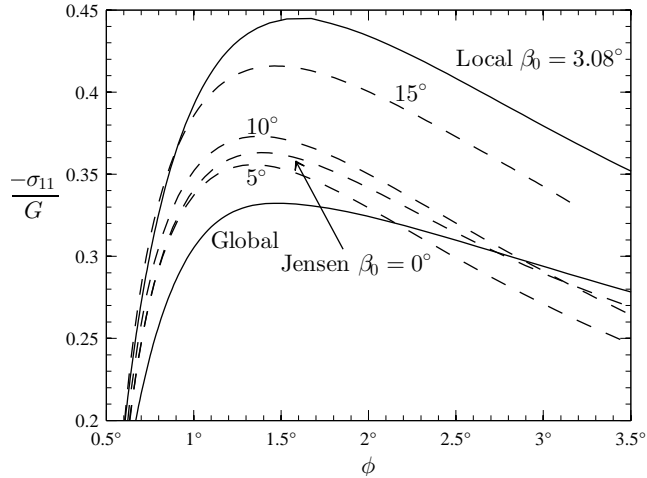parison can be seen in Figs. 2.13 and 2.14.   The tendency of the curves

Figure 2.13: Applied normalized stress as a function of fiber rotation, ϕ, for initial imperfection $\phi_0 = 0.5°$. Jensen is from Jensen and Christoffersen (1997).

is similar, but it can be observed that there is a difference in the values between the curves from Jensen and Christoffersen (1997) and the global and local analyses. The reason for this is due to the presence of a finite kink band width, b, in the global and the local analyses which is absent in Jensen and Christoffersen (1997).

A study on the kink band stress, σ_{11}^{cr}, as a function of initial misalignment angle, ϕ_0, was also made by Jensen and Christoffersen (1997). In addition, the critical kink band angle, β_0^{cr}, was observed. A comparison with present results can be seen in Figure 2.15. The global analysis works as a lower bound while the local analysis works as an upper bound. The reason for the increased deviation between the local and global analyses compared to Jensen and Christoffersen (1997) for small ϕ_0 is the J_2 flow rule used here. This results in a deviation compared to the J_2 deformation theory at very low imperfections which can also be seen in Jensen (1999). Like in Jensen and Christoffersen (1997) it can be observed that β_0^{cr} is in-

creasing with increasing ϕ_0. The critical kink band angle β_0^{cr} for the local analysis is measured at the same time as the critical kink band stress (stage (b) in Figure 2.4), while for the global analysis it is measured just as the kink band has localized i.e. where it is first possible to observe a kink band (stage (c) in Fig. 2.4). To clarify the relation between β_0^{cr} and ϕ_0, the relation is shown in Figure 2.16.

2.5 Conclusion

It was shown in the implementation of the constitutive model in a finite element scheme by Sørensen et al. (2009) that the postbuckling regime was mesh dependent in an applied stress vs. end shortening space. The reason for this is the fact that the mesh is the only length scale used in the constitutive model in a finite element scheme. Since the postbuckling load path is mainly controlled by the fiber bending stiffness, the big difference comes in because there is no bending stiffness included in the constitutive
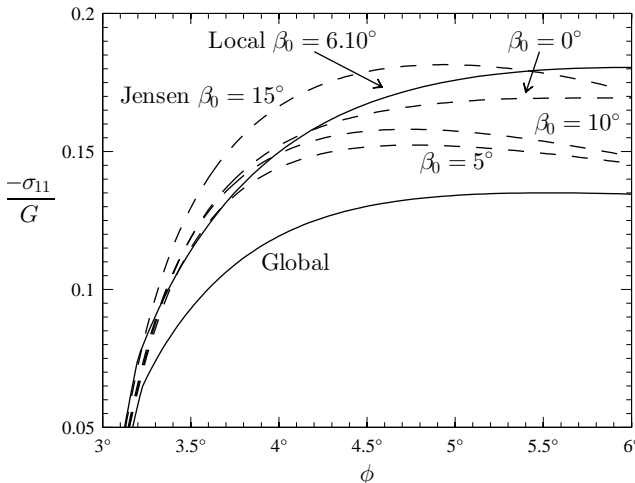
Figure 2.14: Applied normalized stress as a function of fiber rotation, ϕ, for initial imperfection $\phi_0 = 3°$. Jensen is from Jensen and Christoffersen (1997).
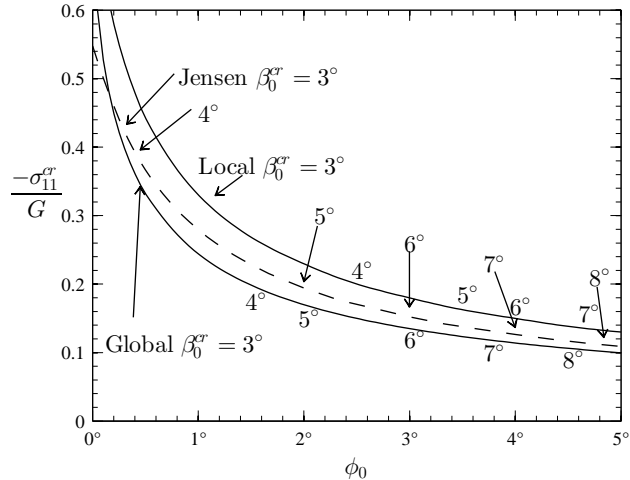
Figure 2.15: Applied normalized critical stress $-\sigma_{11}^{cr}$ as a function of initial fiber misalignment, ϕ_0, with critical kink band angle, β_0^{cr}, indicated. Jensen is from Jensen and Christoffersen (1997).

model.

The same bending stiffness dependency applies for the discretized model and is also due to the width of the kink band that forms. This controls the elastic unloading after the critical stress has been reached. The load path for the discretized model does converge towards the steady state load though. This makes good sense since this is mainly controlled by the material properties of the matrix. In this paper the fiber rotation is chosen instead of the end shortening for comparison, due to a fast convergence on the whole load path.

The comparison of the two models is made with the purpose of validating the constitutive model under plane strain conditions and a homogeneous compressive stress field in Figs. 2.13 - 2.16. The discretized finite element approach has previously shown to be in good agreement with experimental observations and is used as reference in the present work. A micromechanical discretized finite element model has the disadvantage that it is impossible to use in a large structure while the constitutive model used in
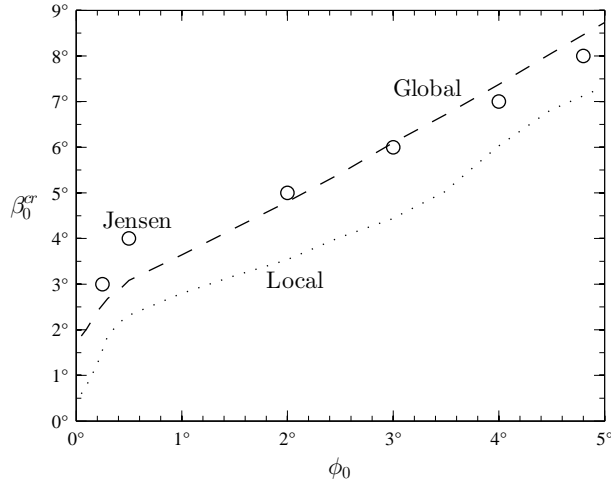
Figure 2.16: Critical kink band angle β_0^{cr} as a function of initial fiber misalignment. Jensen is from Jensen and Christoffersen (1997).

a finite element scheme is possible to use. Of course this comes with some assumptions which have been outlined.

The initial kink band width, b, in relation with the initial fiber angle, ϕ_0, determines the size of the initial imperfection. With this in mind, it is difficult to make a direct comparison of the constitutive model and the discretized model in the applied stress vs. fiber angle space due to lack of information on kink band width in the constitutive model. The approach of introducing a global and then a local imperfection afterwards is a way of letting the equilibrium from the global imperfection analysis determine the size of the local imperfection. The global imperfection analysis works as a lower bound for the critical stress while the local imperfection analysis works as an upper bound. This is valid for all values of ϕ_0 examined in the present work and indicates a good agreement between the two models.

Previous models, e.g. those by Jensen and Christoffersen (1997) and Fleck and Budiansky (1991), assume fixed initial kink band angles which may evolve with the general state outside the kink band. The present

33

results, where a less constrained rotation of the band with increasing fiber rotations is observed, could be applied in improved simplified models such as those by Jensen and Christoffersen (1997) and Fleck and Budiansky (1991).

Failure in a notched beam

Observing compressive failure in unidirectional composites is difficult. First of all the size of the failed region can be very small. Next, the failure can happen instantly with no opportunity of observing what is actually going on during failure. This rapid failure is mostly seen in unidirectional composites in homogeneous unidirectional loading in the fiber direction. A way of getting around this sudden failure is to make a lay-up of the composite with a $[0/90]_s$ stacking. The $90°$ layers then make the failure happen less sudden. Another way is to make the loading non-homogeneous. An example is a beam in bending which will force the compressive failure to happen at the edge of the beam where the compressive stress is highest. To make sure that the failure starts at a specific point, a notch can be introduced. This is what is done in this chapter. A beam in a four-point bend setup as shown in Fig. 3.1 is investigated. A setup like this will produce a
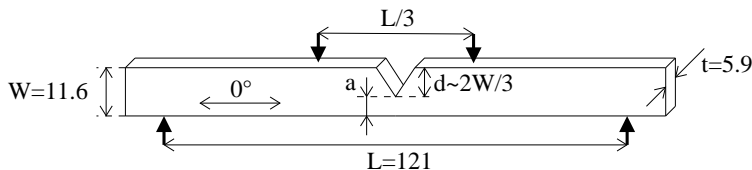

Figure 3.1: A beam in a four-point bend setup. Dimensions are in mm.

failure starting from the notch tip. Compressive initiation of failure and propagation at notches in unidirectional composites can be seen to behave as a material instability forming a kink band or as a crack-like manner. The usual definition of a crack is where an opening between two surfaces is present and the state of stress is dominated by tension. Guynn et al. (1989) violated this definition by introducing a "compressive crack" with a state of stress dominated by compression and a negative stress intensity factor. They viewed the damaged zone as a crack with a plastic zone in a carbon/epoxy composite. They applied the model introduced by Dugdale (1960) to predict the size of the buckled region in multilayered composites. In the Dugdale model a constant normal stress is applied in the damage zone. It was concluded that this did not accurately predict the size of the damaged zone. Soutis et al. (1991) applied a stress which varied linearly with the crack displacement which improved the accuracy.

Waas et al. (1990) introduced a circular hole in a rectangular multi-layered carbon/epoxy composite. This produced a stress gradient at the hole surface in which the failure initiated. The failure mode was fiber microbuckling in the $0°$ ply approximately perpendicular to the loading direction surrounded by delamination.

Sutcliffe and Fleck (1994) used a large scale bridging model for propagating microbuckles in uni-directional carbon/epoxy fiber composites with a rectangular hole using a constant bridging stress and a constant crack tip toughness. The mode of failure was an in-plane and out-of-plane microbuckle as mode II and mode I cracks. They compared the microbuckle displacement with experimental observations. To avoid splitting they cut a notch along the fiber direction. Fleck et al. (1997) further investigated the idea in multilayered composites both analytically and experimentally. The materials used were thermoplastic PEEK matrix reinforced by AS4 and IM8 carbon fibers and Toray T800 carbon fibers in epoxy. They discovered experimentally that the fiber strength had a minor effect in the propagation behavior as well.

Laffan et al. (2011) measured the negative fracture toughness associated with the $0°$ ply in a multilayered IM7/8552 composite. They used compact tension specimens to track down the critical notch tip radius for a correct

measurement of the fracture toughness. Laffan et al. (2012) used that information to measure the fracture toughness in a unidirectional IM7/8552 composite using a single-edge notch beam in a plane stress four-point bend setup.

To view the damaged zone as a crack is a way to observe what happens on macro-mechanical level. To find out what happens at the micromechanical level, modeling of the material instability of the fibers and matrix individually is an option. Ahn and Waas (2002) used a global-local approach to model the material instability in a square plate with a circular hole in a biaxial compression setup. They used a notched laminate of infinite extent to compute the displacement field of a rectangular local region. An imperfection was imposed as a scaling of the first modal vector from a linear eigenvalue analysis. The size of the scaling was determined by the maximum angle of the fibers. A similar approach was used by Davidson et al. (2013) in a rectangular plate with a circular cutout. The procedure was to use the displacement and forces on the boundaries of the local model from a global linear static analysis as an input to a local nonlinear static analysis.

Laffan et al. (2012) viewed the failure as a crack. The scope of this chapter is to see the failure as a material instability instead of a crack. The method is to detect initiation of fiber microbuckling experimentally in a unidirectional fiber composite. A stable failure is desired so the deformation at the composite on material level can be observed. A finite element model is presented to predict the failure initiation and to verify the failure initiation as fiber microbuckling.

3.1 Experiments

The test setup was a four-point bend setup following the standard ASTM D6272 - 10. The test was quasi-static using a loading rate of $0.6\,mm/min$. A picture of the setup can be seen in Fig. 3.2. To take pictures for digital image correlation (DIC) and post observations of deformation and failure during testing, a reflex camera was installed. A picture was taken every
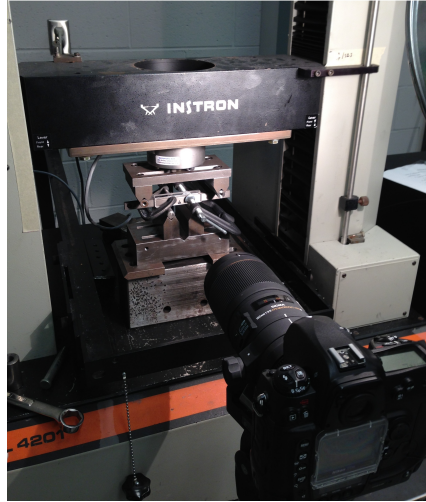
Figure 3.2: Four-point bend test setup.

1 second. The material system used was carbon fiber reinforced plastic IM7/8552 unidirectional prepreg. This material is widely used in aerospace structures. To find the configuration shown in Fig. 3.1, a design iteration was conducted. The first design is shown in Fig. 3.3(a) with $W/L = 0.21$. The outer geometry was cut using water jet technology. The notch was prepared using a water-cooled diamond disc saw making an almost square notch tip. The surface was spray painted so it was possible to track the deformation using DIC during testing. The failed specimen can be seen in Fig. 3.3(b). Because of an angled cut using water jet technology, the
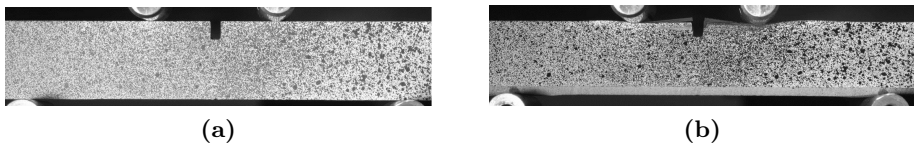

Figure 3.3: The first design failed by flipping and crushing.

specimen flipped before any failure happened at the notch tip. Besides this, a too high contact pressure under the rolls crushed the surface. The second design is shown in Fig. 3.4(a) with $W/L = 0.096$. In this setup, rubber patches were used under the rollers to lower the contact pressure. To avoid flipping, the bottom and top surfaces were made parallel using a water-cooled diamond-coated grinding disc. The notch was prepared using the same technique as in Fig. 3.3. This time the specimen did not flip as
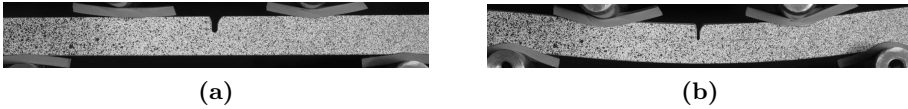

(a)   (b)

Figure 3.4: The second design failed by splitting.

can be seen in Fig. 3.4(b). Instead, splitting happened in the matrix layer. The splitting was observed as a big drop in the load/displacement curve but can also be seen as a line in both directions starting from the notch tip.

Since a kink band failure is wanted in this experiment, an attempt to get rid of the splitting was made. The focus was aimed at the notch tip. The hypothesis was that a higher stress concentration would encourage a kink band to happen instead of splitting. To get a higher stress concentration at only one location, a round notch tip was made instead of a square in the third design as shown in Fig. 3.5(a). This was done using a water-cooled diamond-coated band saw making a cut $\approx 650 \mu m$ wide with a tip radius $\approx 290 \mu m$. This time kinking happened instead of splitting. The failed specimen can be seen in Fig. 3.5(b). From the pictures taken during the test a video clip was made showing the load/displacement curve and the corresponding deformation of the specimen[1]. The applied load was measured using the load cell on the testing machine while the deformation was found using DIC. The first small change in stiffness on the load/displacement curve is where failure is initiated. Next a decrease in stiffness is seen until multiple small changes in the curve are observed. The deformed shape dur-

---

[1]`http://youtu.be/SNOn0e4DwWE`
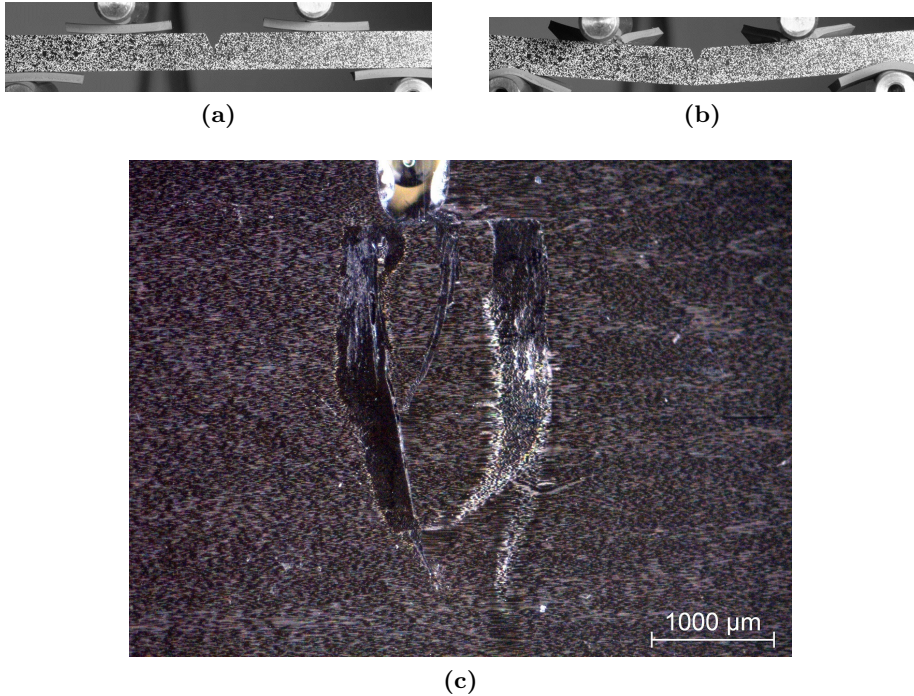
(a)

(b)

(c)

Figure 3.5: The third design failed by kink band formation.

ing testing is made into a video clip[2]. The deformation of a section line just beneath the notch tip is shown in the bottom left corner. In the beginning of the test, the section deforms like a normal beam. As failure kicks in, the deformation has a tendency of discontinuity under the notch tip. This indicates that the load bearing capacity of the section decreases. This is in good correlation with the decreasing of stiffness in the load/displacement curve. In Fig. 3.5(c), a picture of the failure using a microscope at the notch tip is seen. The specimen is unloaded and polished after testing. From the picture, it can be seen that several kink bands has formed. The question is what happened first? To answer this question the test must be

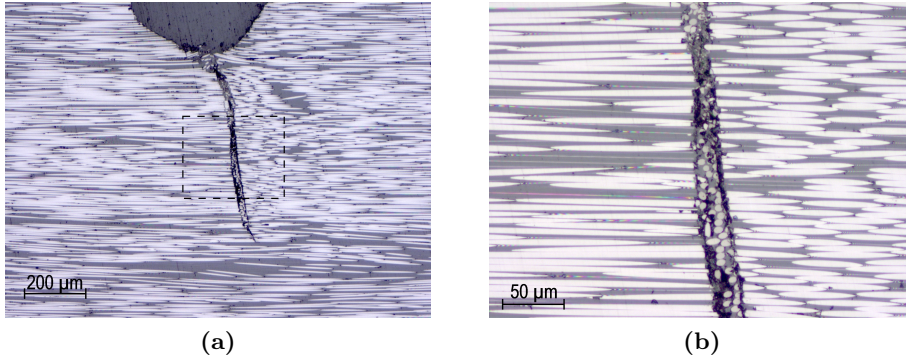---

[2]`http://youtu.be/Kr_LO7snvbg`

Figure 3.6: Failure when the test is stopped right after failure detection. Failure happens out-of-plane.

stopped just after the first sign of failure. This is done in Fig. 3.6 where the notch is prepared slightly differently in addition. The band saw in the third design turned out to be difficult to control. Instead, a slow rotating oil-cooled diamond-coated disc saw was used in the preparation. The cut was made at an angle forming a cusp-like shape of the notch as can be seen in Fig. 3.1. This time the notch tip is observed during testing through the lens on the camera. As soon as failure is seen, the test is stopped. It can be observed that the kinking is out-of-plane because the fibers are orientated out-of-plane in the kink band. From a practical point of view most kinking happens in-plane since 0° layers often are embedded in off-axis layers. To provoke in-plane kinking, glass plates were clamped on the sides inspired by Sutcliffe and Fleck (1994) as shown in Fig. 3.7. If the c-clamps are assumed rigid, a plane strain condition can now be assumed. Using glass gives the opportunity to continue observing failure. The disadvantage using standard c-clamps is that the clamping force in unknown and friction can play a part. By preliminary experiments, it was established that a small clamping force was enough to make the failure happen in-plane. The impact from the glass plates is assumed to have a minor effect on the results. Fig. 3.8 shows pictures from a test using glass plates. Now in-plane kinking
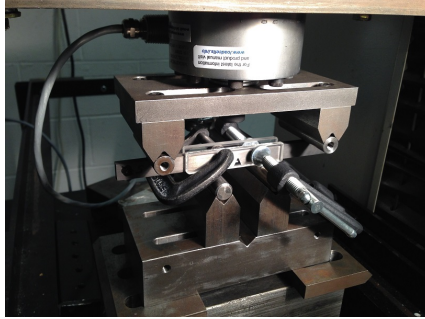
Figure 3.7: Four-point bend test setup with glass plates clamped on the sides using c-clamps.

| | |
| (a) | (b) |
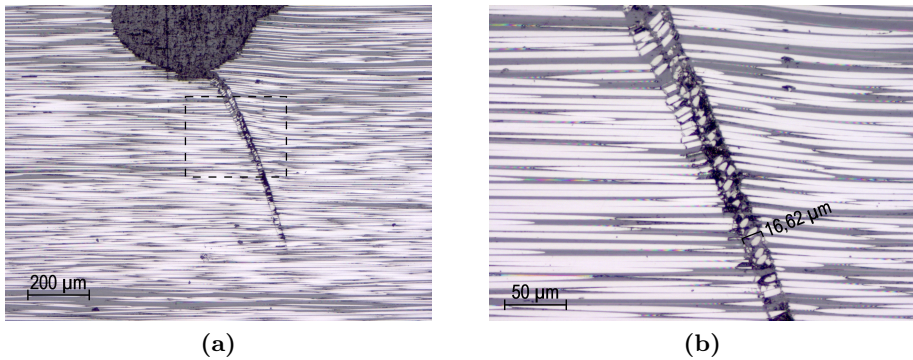
Figure 3.8: Failure when glass plates are clamped on the sides. Failure happens in-plane.

is present and a clearly marked kink band has formed at an angle where the fibers are broken at the edges. The width is constant and is measured to

$$b \approx 3.2 \, d^f \tag{3.1}$$

At the top section, a second kink band is formed adjacent to the first one with the same width.

In the design iteration, some samples failed by splitting. The hypothesis

was that the depth of the notch, d, had an influence on the failure mode. To verify this an investigation was made on the size of d. Three depths were examined; $d \approx W/3$, $d \approx W/2$ and $d \approx 2W/3$. It was found that splitting rarely happened in specimens with $d \approx 2W/3$, and so this configuration was chosen for further study.

Next, eight roughly similar specimens were prepared with a notch tip design as shown in Fig. 3.9. The cuts were made forming an angle at $\theta \approx 67°$. The shape of the disc and the angle of the cut determine the radius, ρ, at the notch tip. ρ was measured in a microscope to be $\rho = 196 \pm 15\mu m$. According to Laffan et al. (2011) the critical notch tip radius
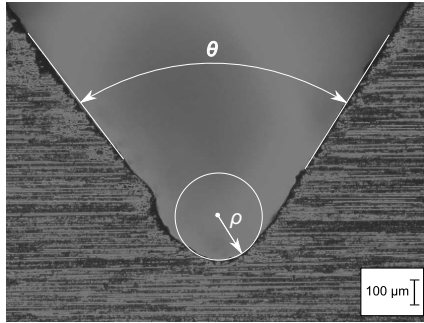

Figure 3.9: Picture taken by microscope before test showing notch tip.

for measuring compressive fracture toughness is $\rho \leq 250\mu m$. The depth of the cut expressed by the remaining width, a, was measured as well to be $a = 3.82 \pm 0.072mm$. The specimens were polished before the test for a better observation of the failure initiation.

The failure in all the tests happened rapidly which means that initiation was not possible to observe. The camera taking pictures during the test did not have sufficient magnification to observe micromechanical initiation. Post observation of the unloaded polished specimens showed one common indicator of initiation of failure in five cases; namely microbuckling at the notch tip. In the three other cases splitting happened before microbuckling. In Figs. 3.10(a), 3.10(b) and 3.10(d), a failure at the notch tip can be observed. It is believed that microbuckling happens first followed by different
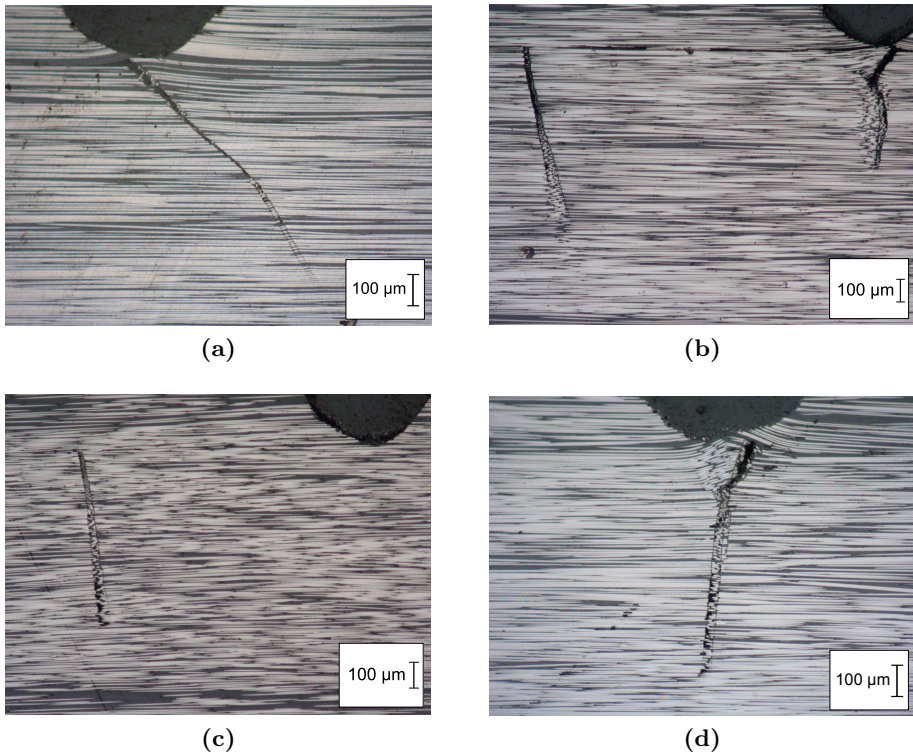
Figure 3.10: Four different types of failure after unloading.

types of postbuckling damage. In Fig. 3.10(a), a compression crack can be seen at an angle ≈ 45° which was also seen by Hancox (1975). Fig. 3.10(b) shows that microbuckling appeared first and was then followed by splitting. In Fig. 3.10(c), splitting happened before microbuckling and therefore microbuckling cannot be observed at the notch tip. In Fig. 3.10(d), the most common type of failure is seen; microbuckling at the notch tip followed by a kink band.

3.2   Analysis

In the experiments, it was shown that fibers break just after damage has initiated. It is assumed that fiber microbuckling happens before fiber breakage. The objective of this analysis is to predict the load, F, where fiber microbuckling appears, e.g. before fiber breakage. The geometry is made from the averaged dimensions of the test specimens, but since only small deviations are present in the measured value of ρ, θ and a, minor deviations in the results would be expected. A 2D plane strain finite element analysis is conducted using a two-step procedure as shown in Fig. 3.11. Step 1: The part is divided into two regions, beam and local. The beam

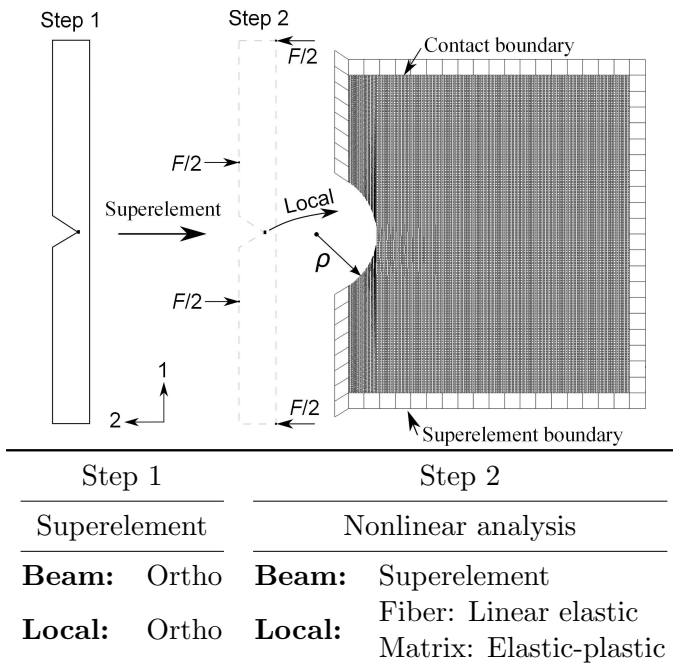|	Step 1		Step 2	
	Superelement		Nonlinear analysis	
Beam:	Ortho	**Beam:**	Superelement	
Local:	Ortho	**Local:**	Fiber: Linear elastic	
			Matrix: Elastic-plastic	

Figure 3.11: FEM workflow.

region is the whole part except for the local region. The beam region is discretized with a coarse mesh. The local region is a small region around

45

	Orthotropic	Isotropic
$E_{11}\,[MPa]$	131090	-
$E_{22}\,[MPa]$	72040	-
$G_{12}\,[MPa]$	48700	-
ν_{12}	0.34	-
$E_f\,[MPa]$	-	276000
$E_m\,[MPa]$	-	4080
ν_f	-	0.3
ν_m	-	0.38
$\sigma^y\,[MPa]$	-	90
n	-	4

Table 3.1: Material parameters used in orthotropic and isotropic analyses.

the notch tip discretized with one element per fiber and matrix individually. This is done in order to keep the same local mesh in step 2 due to the degree of freedom (DOF) numbering. Eight node bi-quadratic elements are used for both regions. The material parameters for both regions in step 1 are 2D orthotropic. The measured orthotropic material parameters for the composites can be seen in Table 3.1. The DOFs associated with the beam region are condensed except for the DOFs where F needs to be applied. The last band of elements from the beam region (and their DOFs) adjacent to the local region is kept as well. A superelement is made for use in step 2.

   In step 2, the previously established superelement is used as input. The superelement is linear and will stay linear in this nonlinear analysis. The superelement is attached to the nodes on the boundary of the last band of elements from the beam region shown in Fig. 3.11. A node-to-segment glued contact is made on the boundary between the local region and the last band elements. This approach prevents contact between the superelement and the local region. The mesh in the local region is the same as in step 1. The local region is built in a similar way as in Wind et al. (2014) where the fiber diameter, d^f, determines the width, W_0, of the local region in relation

with the number of fibers, n^f, and the fiber volume fraction. c^f. W_0 can be found as

$$W_0 = \frac{d^f n^f}{c^f} \tag{3.2}$$

where $c^f = 0.587$, $n^f = 100$ and $d^f = 5.2\mu m$ in this analysis. c^f and d^f is provided by Hexcel[3]. The length of the local region is $L_0 = 1mm$. The semi-circle cut-out is made by use of a perfect circle with tangents corresponding to the cut angle. The material parameters for the fibers are changed to linear elastic isotropic with parameters supplied by Hexcel[4]. The material parameters for the matrix are changed to isotropic elastic-plastic material behavior described by a uniaxial Ramberg-Osgood relation

$$\varepsilon = \frac{\sigma}{E_m} + \frac{3\sigma^y}{7E_m}\left(\frac{\sigma}{\sigma^y}\right)^n \tag{3.3}$$

By differentiation of (3.3), the tangent modulus is obtained,

$$E_m^t = \frac{7E_m}{3n\left(\frac{\sigma}{\sigma^y}\right)^{n-1} + 7} \tag{3.4}$$

which defines all necessary input to the material model. In order to determine material properties, the following approximate relation is applied

$$G_m^t = \frac{E_m^t}{2(1 + \nu_m)} \tag{3.5}$$

where ν_m is chosen according to table 3.1. E_m, σ_y and n are found by curvefitting using (3.5) to an in-situ measured shear stress vs. shear strain curve obtained from tensile tests on $[+45/-45]_s$ laminates. The fitting can be seen in Fig 3.12. Forces and constraints are applied on the DOFs that were kept from the condensation as can be seen in Fig. 3.11. The nonlinear commercial solver MSC Marc is used for the analysis. The arc-length algorithm introduced by Riks (1979) is used for the incremental solution. The J_2 flow theory of plasticity is applied.

---

[3]http://www.hexcel.com/Resources/DataSheets/Prepreg-Data-Sheets/8552_eu.pdf

[4]http://www.hexcel.com/resources/datasheets/carbon-fiber-data-sheets/im7.pdf
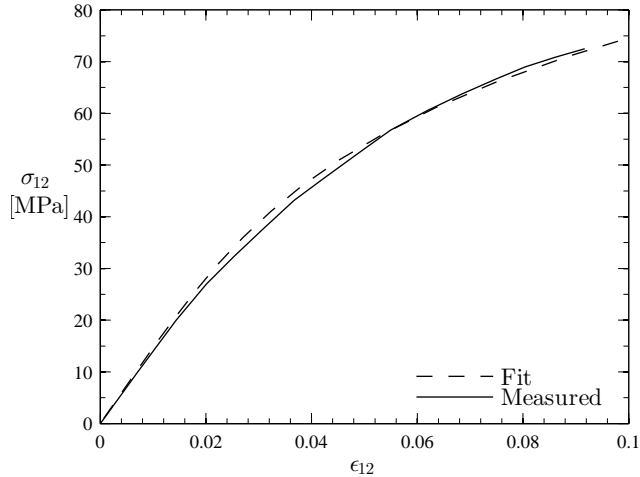
Figure 3.12: Curve fitting using (3.5) with measured in-situ matrix properties.

3.3 Results

In the post observations of the unloaded specimens from the experiments, two main types of failures were observed. Five specimens failed by microbuckling at the notch tip and in some cases followed by splitting while three specimens failed by splitting with no microbuckling at the notch tip observed. The competition between splitting and kinking has been addressed by Prabhakar and Waas (2013). The force at which damage initiates was found by looking at the pictures taken by the camera and compared with the time the picture were taken to be $F_{E,cr} = 765 \pm 41\,N$. A comparison between the forces, F_E, from the experiments and the critical force from the analysis with straight fibers, $F_{A,cr}$, can be seen in Fig 3.13. The force/displacement curve from the experiments has a stiffness drop in the beginning due to compliance of the test setup and crushing of the fibers under the rollers. It shows a degradation in bending stiffness when damage occurs when observing the externally applied force from the analysis with straight fibers, F_A, normalized with the critical average force from experi-
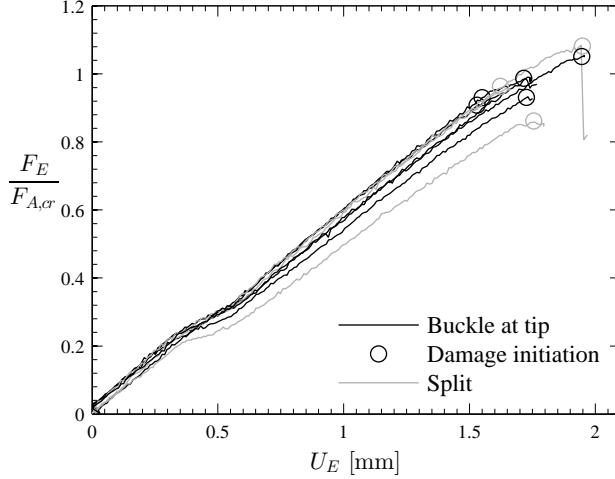
Figure 3.13: Externally applied force from experiments, F_E, normalized with critical force from the analysis, $F_{A,cr}$ with straight fibers vs. displacement tracked by the testing machine, U_E. The color shows if the failure was splitting or microbuckling.

ments, $F_{E,cr}$, in Fig. 3.14. This corresponds to a lowering of the moment of inertia of the beam. Due to this, the depth of the initial damage affects the remaining bending stiffness highly. As can be seen in Fig. 3.10 the damage depths in the experiments differ so the degradation of bending stiffness would not be directly comparable if the tests were continued after damage has initiated. A more clear indicator of when damage initiates is obtained by tracking the compressive force in the first fiber next to the notch tip. Since a contact condition is used between the beam and the local region, the contact force, F_C, is used as an indicator when damage initiates. F_C measured in the middle node in the fibers is shown as a function of position along the top contact edge in Fig. 3.15 for initial straight fibers and with an imperfection. The coordinate system is placed at the notch tip here. The measurement is made in the increment when the contact force is highest, i.e. when the critical externally applied force, $F_{A,cr}$, is reached. F_C is shown
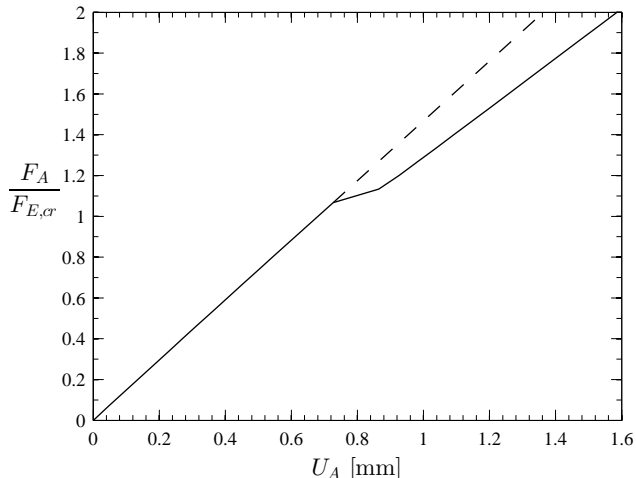
Figure 3.14: Externally applied force as a function of external displacement from the finite element analysis with straight fibers.

as a function of $F_A/F_{E,cr}$ for straight fibers and for fibers with a waviness in Fig. 3.16. Microbuckling occurs when the force drops and $F_{A,cr}$ can be noted. An imperfection is introduced to see what effect this has on the critical load and on the deformation profile. The imperfection is imposed as a fiber waviness in a specified region as shown in Fig. 3.17. The imperfection is applied as a decreasing cosine function in the area constrained by the height, b, and the offset from center, k, as

$$x_2 = \frac{h}{2}\left(1 - cos\left(\frac{2\pi x_1}{b}\right)\right)x_d \tag{3.6}$$

where h is determined from the misalignment angle, ϕ_0

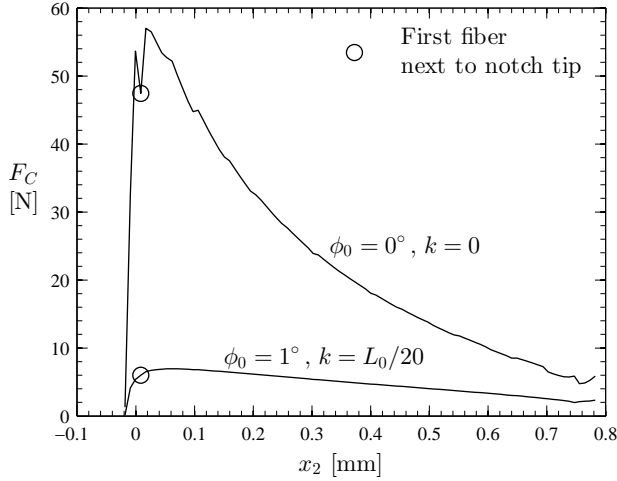$$h = \frac{2b\tan(\phi_0)}{\pi} \tag{3.7}$$

50

Figure 3.15: Contact force in the fibers as a function of position along the top contact edge measured in the increment when the contact force is highest.

and x_d is a decaying function similar to the one used by Kyriakides et al. (1995)

$$x_d = exp \left[\zeta \left(\frac{x_2}{\alpha W_0} \right)^2 \right] \tag{3.8}$$

Two types of imperfection are made; (I) centrally located imperfection ($k = 0$) and (II) imperfection offset from center with $k = L_0/20$. The reason for making an offset is to see if an asymmetric imperfection will result in a different critical load and deformation profile. Common parameters used are

$$b = 0.2 \quad , \quad \zeta = ln(0.01) \quad , \quad \alpha = 0.3 \tag{3.9}$$

It is clear that introducing a fiber waviness decreases the critical force. Introducing the offset of the waviness does not have a big effect on the results compared to no offset. It should be noted that changing the sign of ϕ_0 will result in a critical force comparable to the one with straight fibers.
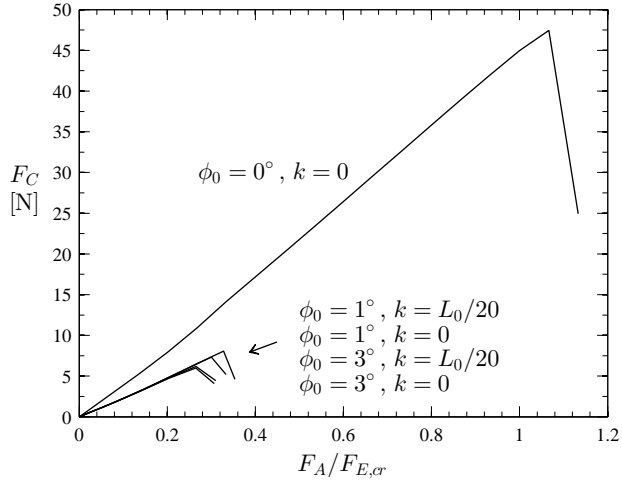
51

Figure 3.16: Contact force in the fiber just after the notch tip measured in the middle node as a function of externally applied force.

Comparison of the deformation profile of the specimens failed by microbuckling at the notch tip (e.g. Fig. 3.10(d)) and the analysis in Fig. 3.18 shows similar behavior. A microbuckle at the free edge in the notch tip can be observed in both figures. In the experimental pictures, the fibers are broken though, but the deformation profile is comparable to the deformation profile from the analysis. In the analysis with fiber waviness, the deformation profile at the critical force is comparable to the one with straight fibers.

3.3.1   Compressive crack approach

According to Laffan et al. (2012) the mode I critical energy release rate, $G_{I,cr}$, were found when treating the damage as a compressive crack under plane stress conditions. To compare this result with the critical load found in this study using plane strain condition, $F_{E,cr}$, the J-integral approach introduced by Rice (1968) is used. When a rounded crack tip is present,
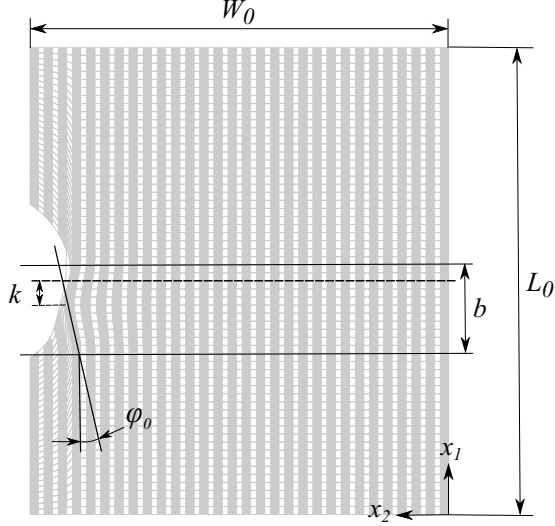
Figure 3.17: Imperfection parameters shown with 30 fibers.

the relation between the critical stress intensity factor $K_{I,cr}$ and the notch tip radius ρ is

$$K_{I,cr} \leq \sigma_{max}\sqrt{\rho} \tag{3.10}$$

If a constant stress along the edge exist, the equality in (3.10) holds true. Using the relation between $G_{I,cr}$ and $K_{I,cr}$ from Paris and Sih (1964)

$$G_{I,cr} = \frac{K_{I,cr}^2}{\sqrt{2E_{11}E_{22}}}\sqrt{\sqrt{\frac{E_{11}}{E_{22}}} + \frac{E_{11}}{2G_{12}} - \nu_{12}} \tag{3.11}$$

a comparison with the results by Laffan et al. (2012) can be made. The maximum stress at the rounded notch tip with the radius, ρ, is found using a Voigt estimate of Young's modulus for the composite, E^c, as

$$E^c = c^f E^f + c^m E^m \tag{3.12}$$

which is suitable in this analysis since the fibers are in the direction of the loading. For Poisson's ratio, a Voigt estimate is used as well. The critical
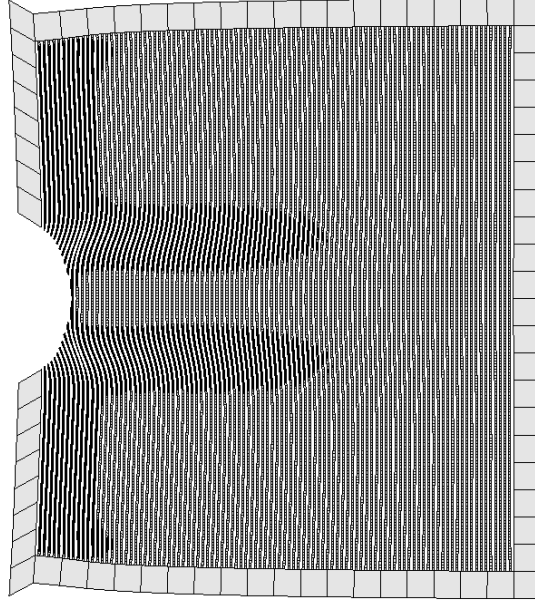
Figure 3.18: Deformation upscaled 3 times from the finite element analysis with straight fibers at critical force where fiber elements are hidden. The darker region indicates plastic strains in the matrix elements.

applied force from the analysis with straight fibers, $F_{A,cr}$, is applied to the model and a linear elastic analysis is conducted to extract the maximum stress, σ_{max}, at the notch tip boundary. The compressive stress profile at the notch tip boundary can be seen in Fig. 3.19. The maximum stress, σ_{max}, is noted and $G_{I,cr}$ can be calculated using (3.10) and (3.11) to be

$$G_{I,cr} = 28.3\,kJ/m^2 \tag{3.13}$$

This is a higher critical energy release rate than the averaged value established by Laffan et al. (2012) which is $25.9 \pm 4.8\,kJ/m^2$ but within the deviation. This result is very satisfying since two different approaches of calculating $G_{I,cr}$ and different experiments gives an almost identical result. Using (3.10) results in a lower bound of $K_{I,cr}$ but since the upper bound
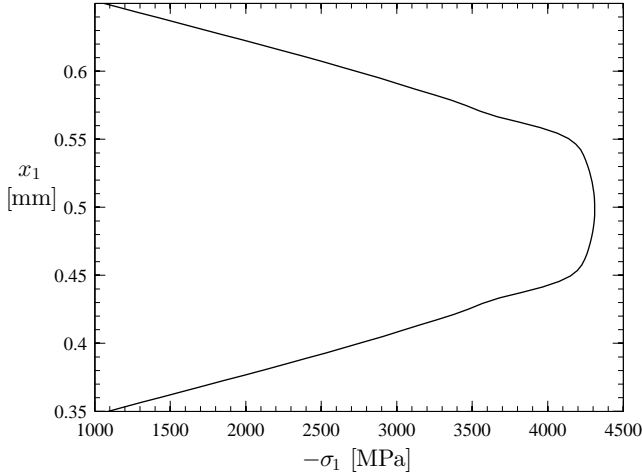
Figure 3.19: Compressive stress $-\sigma_{11}$ as a function of position x_1 in the notch tip.

estimate for E^c (Voigt estimate) is used in the extraction of σ_{max}, this will increase $K_{I,cr}$. If fiber waviness was introduced, a lower σ_{max} would also be observed.

3.4 Conclusion

By using a unidirectional lay-up of a composite single-edge notch beam in a four-point bend setup, it is shown that it is possible to observe a kink band instability across the fibers. In some cases splitting happened along the fibers at a load comparable with the fiber kinking load. In the setup used, fiber kinking would happen out-of-plane if plane stress conditions were used. To apply an approximately plane strain condition, glass plates were clamped on to the sides to provoke the kinking to happen in-plane. When kinking happens, the failure initiation shows indication of fiber instability at the notch tip followed by kink band formation with fiber breakage at the kink band boundary.

By observing the load/displacement curve, when splitting occurs a big load drop is observed. When kinking happens only a small load drop is seen. As a consequence of kinking, the stiffness of the beam decreases while the load bearing effective height is reduced.

Through the comparison of the experimental and the finite element analyses, it is shown that using an individual fiber and matrix discretized finite element model, it is possible to predict an initiation force when microbuckling occurs. The finite element analysis overestimates the critical force by 4% in the analysis with straight fibers compared to the experimental critical force for microbuckling which is very satisfying. When observing fibers near the notch tip before the test, it is only possible to observe very small fiber misalignment. If initial fiber waviness is introduced, a decrease in the critical force can be observed. This is only present if the waviness is made with ϕ_0 being positive in Fig. 3.17. If ϕ_0 was negative a critical force similar to the analysis with straight fibers is observed.

By using the maximum stress at the notch tip when the critical force is applied in the analysis, a comparison is made with the model of Laffan et al. (2012) where the damage is seen as a compressive crack. A 9% difference in the critical energy release rate for a mode I crack is calculated. This is again very satisfying since two different approaches and experiments provide similar results. This shows that the critical energy release rate for this system repeated by Laffan et al. (2012) appears to be accurate. Consequently, the four-point bend method, as analyzed, has been used to measure the "equivalent" critical energy release rate for a fiber-reinforced laminate.

Slenderness and imperfection sensitivity

A long slender column exposed to compression will result in column buckling also known as Euler buckling. This is an elastic macro buckling mode controlled by the aspect ratio of the geometry and the stiffness of the column. Euler buckling can occur for all types of materials and the failure mode is similar independent of the material. Increasing the aspect ratio will violate the assumptions describing a column and, as a consequence, plastic buckling can occur. This is still a macro buckling mode, and can also be seen for many types of materials. By further increasing the aspect ratio, a difference starts to show for different materials. An isotropic material like steel will fail by yielding, while a unidirectional fiber composite, with the fibers located in the direction of the load, will fail by a material instability in most cases. This can be either elastic- or plastic microbuckling as discussed in chapter 2.

The buckling stress in Euler buckling is known to be rather insensitive to imperfections while it was shown in chapter 2 that kinking stress was highly sensitive to imperfections. In this chapter an imperfection sensitivity study of different aspect ratios is conducted. The scope of this parametric study is to understand what happens in the transition from a long slender

column to a wide panel. The comparison parameter is the critical applied stress.

4.1 Analysis

It was found by Jensen (1999) that there was a deviation in the load/displacement curve when using J_2 flow theory compared to J_2 deformation theory for small imperfections. The deviation was localized near the critical load. It is well known that using J_2 flow theory in bifurcation analyses often overestimates the critical load in e.g. analysis of shells (Tvergaard, 1983). In this study small imperfections are considered so the J_2 deformation theory describing the plastic flow of the matrix is applied. In chapter 2, the commercial finite element code Marc from MSC Software was used. However, the J_2 deformation theory is not an option in Marc so in this chapter, a self-developed finite element code written in MATLAB is used instead.

The constitutive tensor for J_2 deformation theory for small strains described in Tvergaard (2001) is

$$L_{ijkl} = \frac{E_s}{1 + \nu_s} \left(\frac{1}{2} \left(\delta_{ik}\delta_{jl} + \delta_{il}\delta_{jk} \right) + \frac{\nu_s}{1 - 2\nu_s}\delta_{ij}\delta_{kl} \right.$$
$$\left. - \frac{3}{2} \frac{E_s/E_t - 1}{E_s/E_t - (1 - 2\nu_s)/3} \frac{s_{ij}s_{kl}}{\sigma_e^2} \right) \qquad (4.1)$$

where δ_{ij} is the Kronecker delta. E_t is the tangent modulus and E_s is the secant modulus. ν_s is a parameter defined by

$$\frac{\nu_s}{E_s} = \frac{\nu}{E} + \frac{1}{2} \left(\frac{1}{E_s} - \frac{1}{E} \right) \qquad (4.2)$$

A small strain theory is chosen here for simplicity and since the comparison parameter is the critical load, only small strains would be expected. The material parameters used in this chapter are consistent with those used in chapter 2. A Ramberg-Osgood relation was used for the matrix material described by

$$\varepsilon = \frac{\sigma}{E} + \frac{3\sigma^y}{7E} \left(\frac{\sigma}{\sigma^y} \right)^n \qquad (4.3)$$

The material parameters, fiber volume fraction and fiber diameter is shown in Table 4.1.

E^f/E^m	35
ν_f	0.263
ν_m	0.356
σ^y/E^m	0.013
n	4
c^f	0.6
d^f	$5.2\mu m$

Table 4.1: Parameters used in the analyses.

The model is similar to the model in chapter 2 but the geometry is different. The changing aspect ratio is defined by

$$\lambda = \frac{W_0}{L_0} \tag{4.4}$$

Since the size of λ is investigated, an algorithm changing λ in a way such that the results are comparable must be found. In Fig. 4.1, three different approaches are introduced where the fibers are orientated along the x_1 axis. In Fig. 4.1(a), the length, L_0, is kept constant while the width, W_0, increases. Keeping the fiber diameter, d^f, and the fiber volume fraction, c^f, constant therefore increases the number of fibers and due to this the number of elements. In Fig. 4.1(b), W_0 is kept constant while L_0 increases. For the results to be valid when λ is large a certain amount of fibers must be included. This increases the number of elements when λ is small. In Fig. 4.1(c) the area, A, is the same when λ is small and large. This means that the number of elements is approximately the same in every analysis controlled by the value of A. This is desirable since the analysis time will be similar for all values of of λ while still giving an accurate result. Due to this, configuration 4.1(c) is chosen for further study.

An imperfection is imposed in the same way as in chapter 2 by

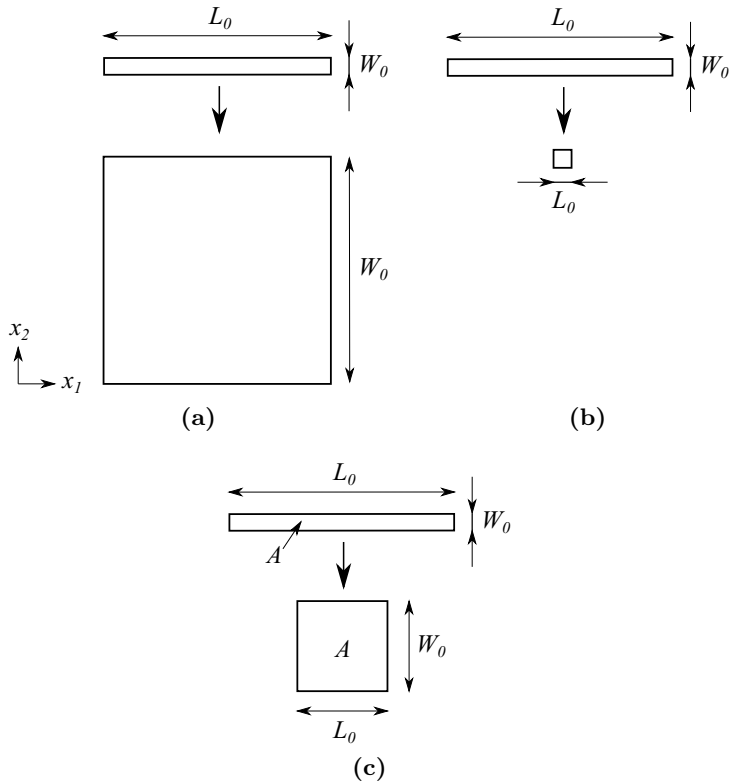$$x_2 = \frac{h}{2}\left(1 - cos\left(\frac{\pi x_1}{b}\right)\right) \tag{4.5}$$

Figure 4.1: Different approaches in changing the aspect ratio λ. In (a) L_0 is constant, in (b) W_0 is constant and in (c) the area A is constant.

which is the same equation as (2.25). b is the width of the kink band, and the amplitude, h, is determined from the initial misalignment angle, ϕ_0, as

$$h = \frac{2b\tan(\phi_0)}{\pi} \tag{4.6}$$

which is the same as (2.26). The imperfection is made as a *global* imperfection meaning that $b = L_0$ in all analysis. Using the method of constant A as shown in Fig. 4.1(c) will induce different values of h because b is

changing as λ is changing. This effect will be discussed in section 4.2.

The geometry of the model is calculated by A, λ and d^f which is pre-specified parameters. To get comparable results when changing λ, a fixed d^f is chosen in all analysis. W_0 is found by first introducing a specified value of λ^*

$$W_0^* = \sqrt{A\lambda^*} \tag{4.7}$$

which leads to the number of fibers in the model, n^f,

$$n^f = round\left(\frac{W_0^* c^f}{d^f}\right) \tag{4.8}$$

By the rounding to the nearest integer, the actual value of W_0 can be found by

$$W_0 = \frac{d^f n^f}{c^f} \tag{4.9}$$

and then the actual value of λ can be found by (4.4) using L_0 calculated as

$$L_0 = \sqrt{\left(\frac{A}{\lambda^*}\right)} \tag{4.10}$$

This means that λ is a function of a rounded value. When plotting the results, the actual λ is used instead of λ^*.

The edge at $x_1 = 0$ are fixed in the x_1 direction and the point $x_1 = y_1 = 0$ is fixed in the x_2 direction as well. The edge at $x_1 = L_0$ are fixed for rotation using Lagrange multipliers to enforce constraints (Cook, 2001). This means that when λ is small a deformed state similar to buckling of a fixed-fixed column, where symmetry applies at $x_1 = L_0$, is expected. The arc length solution technique is chosen again, so that it is possible to pass an eventual limit point.

4.2   Results

Initially, the size of A must be established. A convergence study is conducted in order to observe what effect changing A has on σ_{11}^{cr}. This is done
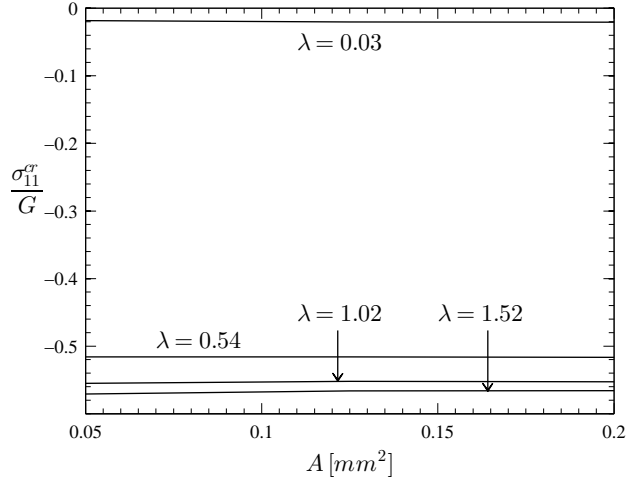
Figure 4.2: Convergence of the critical load as a function of model area for different aspect ratios.

for four different aspect ratios. The result is shown in Fig. 4.2 where it can be seen that changing A from $0.05mm^2$ to $0.2mm^2$ has a negligible effect on σ_{11}^{cr}. Due to these findings, A is chosen to be $0.05mm^2$.

In Fig. 4.3 the critical load as a function of the aspect ratio is shown for several initial fiber misalignment angles, ϕ_0. The critical Euler buckling stress, σ_{11}^{Euler}, for a fixed-fixed column is shown for comparison and is adopted from Chau and Rudnicki (1990) as

$$\sigma_{11}^{Euler} = -\frac{\bar{E}}{3}\gamma_m^2 \tag{4.11}$$

In the above expression, $\bar{E}$ was found in Pane and Jensen (2004) by using the Voigt estimate for σ_{11} as

$$\sigma_{11} = c^f \sigma_{11}^f + c^m \sigma_{11}^m \tag{4.12}$$

and then $\bar{E}$ becomes

$$\bar{E} = c^f \left(L_{1111}^f - \frac{L_{1122}^f{}^2}{L_{2222}^f} \right) + c^m \left(L_{1111}^m - \frac{L_{1122}^m{}^2}{L_{2222}^m} \right) \tag{4.13}$$
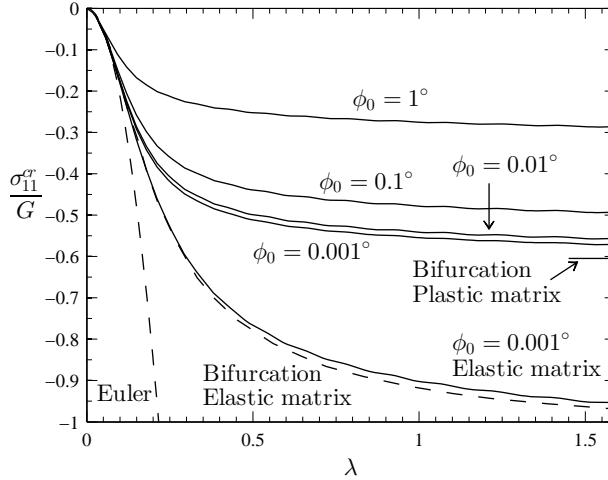
Figure 4.3: Variation of critical applied stress as a function of aspect ratio for different sizes of imperfection. An asymptotic value for the bifurcation kink band stress for plastic matrix found by Jensen and Christoffersen (1997) is included as well. A result with elastic matrix is included for comparison with a bifurcation analysis by Pane and Jensen (2004).

for small strains, elastic behavior and initial values of c^f and c^m. The constitutive values for elastic material parameters are found using Hooke's law. In (4.11), γ_m is the critical wave number given by

$$\gamma_m = \frac{\pi}{2}\lambda \tag{4.14}$$

From Fig. 4.3 it can be seen that for small values of λ the critical stress for all ϕ_0 is approximately equal to (4.11). This was expected since only geometrical nonlinearities are present leading to elastic Euler buckling. In Fig. 4.4(a) a part of the load/displacement curve for $\lambda = 0.027$ is shown with a zoom-in view in Fig. 4.4(b). For the small imperfections it is clear that a stable postbuckling behavior is reached shortly after the sharp bend in the curve, while the larger imperfections converge to the approximately same value by continuing the analysis. This is a well known behavior for
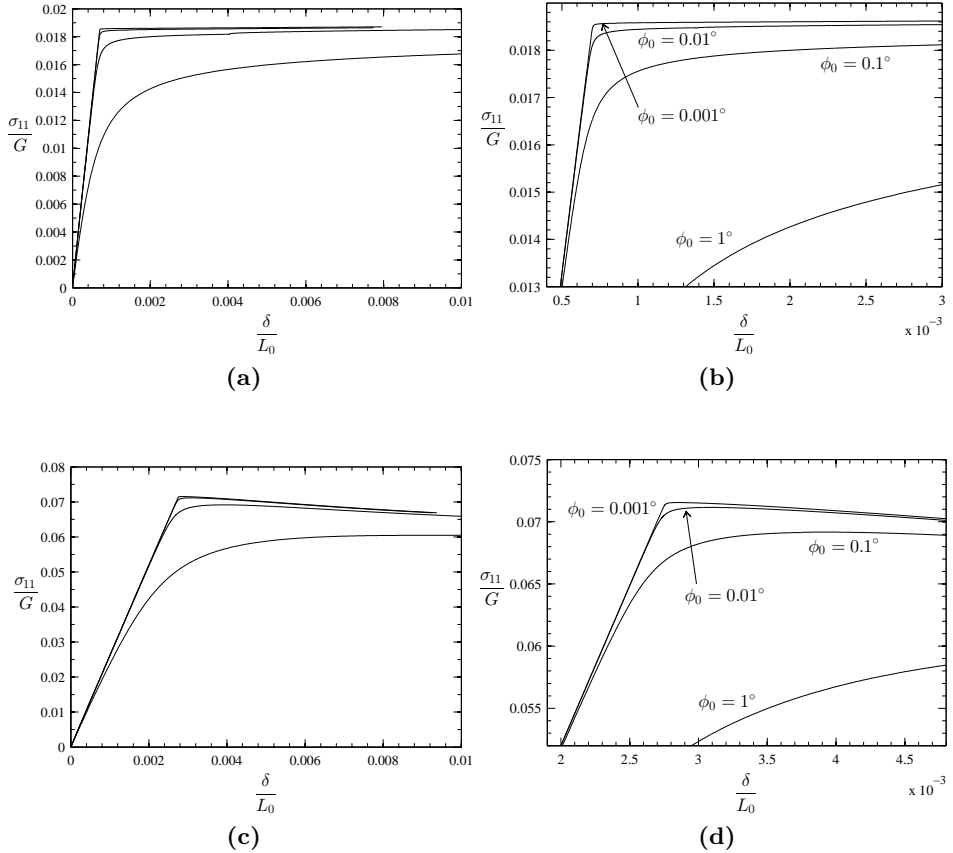
Figure 4.4: Applied stress as a function of end-shortening for $\lambda = 0.027$ in (a) and (b) and $\lambda = 0.057$ in (c) and (d).

Euler buckling event. Increasing the aspect ratio to $\lambda = 0.057$ in Fig. 4.4(c), with a zoom-in view in Fig. 4.4(d), shows the same tendency but this time the postbuckling is not stable, i.e. the applied stress decreases while the displacement increases. However, the deformation is still dominated by geometrical nonlinearities. σ_{11}^{cr} is a little lower than σ_{11}^{Euler} but still very

close when λ is close to 0 as can be seen in Fig. 4.3. Increasing the aspect
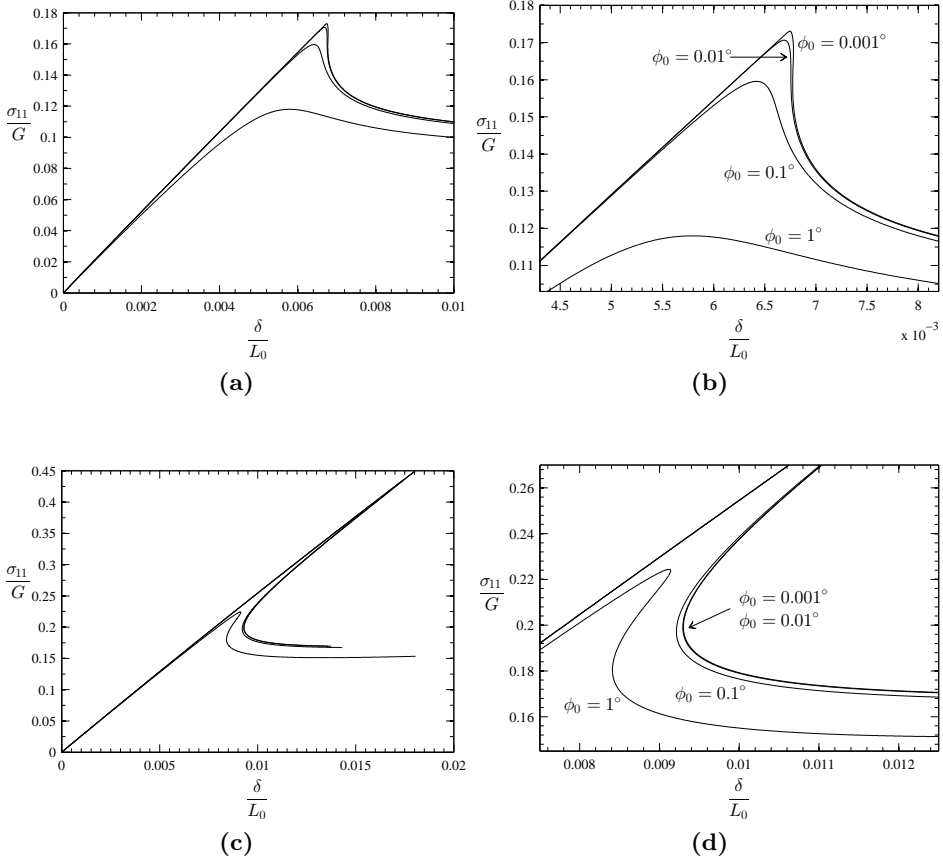
Figure 4.5: Applied stress as a function of end-shortening for $\lambda = 0.093$ in (a) and (b) and $\lambda = 0.29$ in (c) and (d).

ratio to $\lambda = 0.093$, σ_{11}^{cr} starts to deviate from σ_{11}^{Euler}. By observing the applied stress as a function of displacement in Fig. 4.5(a), with a zoom-in view in Fig. 4.5(b), a larger load drop after the critical stress is seen. This tendency looks more like a classical kink band load/displacement curve, and

by increasing λ to 0.29 this trend is even more evident as seen in Figs. 4.5(c) and 4.5(d). The well known snap-back behavior for kink band formation with small imperfections is also seen in Fig. 4.5(c). Continuing the analysis in Fig. 4.5(c) for all imperfections, a convergence to the same steady state load would be expected. This has been addressed by e.g. Kyriakides et al. (1995) and Sørensen et al. (2009), to be the case.

The critical applied stress still increases when λ increases as can be seen in Fig 4.3. In Jensen and Christoffersen (1997) they found the critical kink band stress to be $\sigma_{11}^{cr}/G = 0.61$ for a bifurcation analysis with the same material parameters as used here by using the constitutive model as described in chapter 2. Expanding the curve for $\phi_0 = 0.001°$ to larger values of λ a convergence close to the finding in Jensen and Christoffersen (1997) would be expected. The asymptotic value is marked in Fig. 4.3 as well.

In Fig. 4.3 two curves for elastic behavior of the matrix are shown. One for bifurcation analysis from Pane and Jensen (2004) using the constitutive
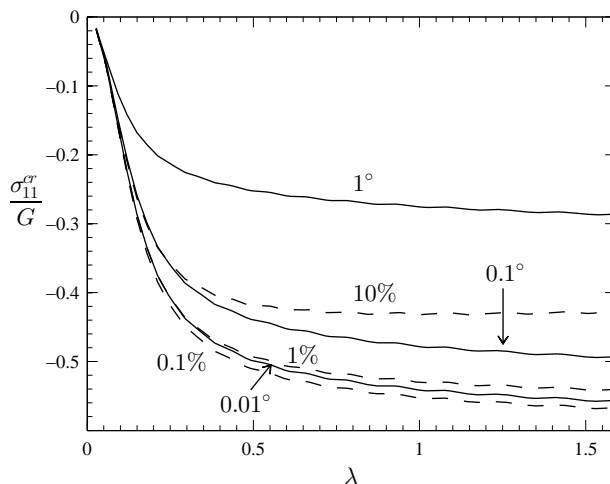

Figure 4.6: Variation of critical applied stress as a function of aspect ratio for initial imperfections by ϕ_0 and amplitude in % of fiber diameter d^f.

model explained in chapter 2 and one with $\phi_0 = 0.001°$ using the present analysis. The model with $\phi_0 = 0.001°$ has in general a little lower value of σ_{11}^{cr} than the bifurcation analysis. This is expected because a bifurcation analysis, in general, always give an upper limit for σ_{11}^{cr}. The two curves converge towards $\sigma_{11}^{cr}/G = 1$ for large values of λ which was the estimate by Rosen (1965) for a model with no imperfections and elastic material behavior.

By choosing the method in Fig. 4.1(c) for varying the aspect ratio of the geometry, the amplitude, h, in (4.6) will change as λ is changing. By specifying h directly a constant amplitude for all analysis can be derived. In Fig. 4.6 a suggestion is made by defining h as an initial percentage of d^f from 0.1% to 10%. Comparing the curves to the curves with a specified ϕ_0 there is not much difference in the tendency between the two types of initial fiber misalignment for small imperfections. The curve for 10% is less influenced by λ for values above 0.5 than the curves with a defined initial fiber misalignment angle.

4.3 Conclusion

The difference in the imperfection sensitivity is addressed by conducting a parametric study on the aspect ratio of the geometry and the size of imperfection. In the region of Euler buckling, where the failure is dominated by geometrical nonlinearities, it is shown that the imperfection sensitivity is small compared to the region dominated by kink band formation for unidirectional fiber composites. This observation is shown by a relation between the aspect ratio and the critical applied stress. The load/displacement curve for four different aspect ratios is shown, and a clear difference is seen. A stable post buckling in the Euler buckling regime is observed, while a large load drop and snap back behavior is observed in the kink band regime. In the transition between the two extremes the load/displacement curves show a combination of the two types.

A comparison is made with a bifurcation analysis using a constitutive model by Pane and Jensen (2004) for an elastic matrix material and a

plastic matrix material in the results by Jensen and Christoffersen (1997). A good correlation between the two models is observed for the applied stress vs. aspect ratio space.

Discussion and perspective

In structural calculations of composite materials, failure criterion is much more complex than for example a yield criterion for metals. Many composite failure criteria exist and they are often based on the state of stress or the strength of the material. In these failure criteria the micromechanics are disregarded and it is only possible to determine if the material fails or not. This means that simulating what is actually going on in a micromechanical perspective is not an option. This can be solved by modeling the fiber and matrix individually, for example in a small area of interest. Doing this will always increase the number of elements and will in some cases be impossible to solve. This encourages the need for a way to capture the failure but without a huge increase in elements. The constitutive model by Christoffersen and Jensen (1996) was a way to do this. If the developers of a commercial finite element softwares trust this model, enough to implement it in their code, the constitutive model is a success. This means that the model must be verified in different configurations to build this trust. The work done in this thesis is a way of verifying the model in a standard setup like a kink band analysis using an individual fiber and matrix discretized model.

Geometrical considerations in the kink band analysis concerning the outer geometry have not been taken into account. The aim was to simulate

a kink band of infinite width and to apply the load far away from where kinking occurs. If the width-to-height ratio is changed from a wide panel to a long slender beam, competing failure mechanism are observed. The Euler buckling and the kink band formation are well known in their respective extreme position. The information found in this thesis is useful in a better understanding of the micromechanics when there is not a clear indicator of which failure mode will occur.

The initiation of failure in a non-homogeneous stress field is discussed as well. In the single-edge notch beam used as example here, it was found that it was possible to predict the failure load using the individual fiber and matrix finite element model. It was very satisfying to compare the results with a compressive crack approach and the experiments and obtain almost similar results. These results help us understanding which mechanisms affect the failure initiation.

The superelement technique has had some trouble in finding its place in everyday use in structural finite element analyses. Mostly because of faster and faster computers with better and better equation solvers as these made the technique less interesting, especially in linear static analyses. The decrease in the system of equations that needs to be solved in the stiffness equation can rarely account for the matrix operations necessary for obtaining the superelement in linear static analyses. Using a superelement in a nonlinear static analysis puts the technique in a whole new perspective. By dividing the structure into small areas of interest and the rest into one or more superelements, it is possible to do complex nonlinear analyses without the need of tremendous amount of computational power. This will provide the degree of detail wanted while the stiffness from the rest of the structure is included. Of course this method should be used with caution but when the area of interest is well known and material or geometric nonlinearities do not affect the results, you are home safe.

In a perspective of the further development of this area of research, several things are interesting to address. First of all, it could be an idea to try to use the constitutive law in a finite element code in the single-edge notch beam. Since the experimental observations and the numerical results from the finite element analysis showed similar findings, this would

70

be a good place to test the constitutive model. In the work by Veluri and Jensen (2011) they used the constitutive model implemented in ABAQUS by Sørensen et al. (2009) as a user subroutine to track failure in geometries with holes. A similar approach could be used in the calculations of the critical load in the beam.

In the single-edge notch beam experiments, it was tried out to see if it was possible to find the state of strain at a very small ares at the notch tip using digital image correlation. The speckle pattern was made using spray paint, but the resolution was too poor to get a satisfying result. Motivated by this work, a similar experiment was later made where the speckle pattern was made just by sandblasting of the black carbon fiber-reinforced epoxy composite surface. This showed very promising results so this method is definitely worth investigating.

In a kink band analysis using an individual fiber and matrix in a finite element analysis it is necessary to have many layers of fibers and matrix to obtain satisfying results. Gutkin et al. (2010) and Romanowicz (2013) used an approach by introducing periodic boundary conditions. This reduces the number of fiber and matrix layers to one which reduce the computational time significantly. The disadvantage is that the kink band angle is locked at zero degrees. By using the findings in chapter 2 where the kink band angle is approximately half of the fiber angle, it may be possible to use this relation in the application of the periodic boundary conditions.

As mentioned in the introduction in chapter 1, there is a growing demand on the use of composite materials in many applications. That is why this area of research maintains its importance in the mechanical field. By a better understanding of the mechanisms of composite materials, a greater trust is achieved in the making of constructions with a lower safety factor. By observing the dramatic load drop in a kink band analyses, it is understandable why big safety factors are needed. Designing against the steady state load, which is in the area around 1/3 of the critical load, is also an option. If the loading and lay-up is well known, a lot of material could be saved and a lighter structure would be achieved which in many cases is the reason for producing the structure in composite material in the first place.

Bibliography

Ahn, J. H., Waas, A. M., 2002. Prediction of compressive failure in laminated composites at room and elevated temperature. AIAA journal 40 (2), 346–358.

Argon, A. S., 1972. Fracture of composites. Treatise on Materials Science and Technology 1, 79–114.

Arruda, E. M., Boyce, M. C., 1993. Evolution of plastic anisotropy in amorphous polymers during finite straining. International Journal of Plasticity 9, 697 – 720.

ASTM D6272 - 10, 2013. Standard Test Method for Flexural Properties of Unreinforced and Reinforced Plastics and Electrical Insulating Materials by Four-Point Bending.

Borg, U., 2003. Tryk og trækstyrke af fiberlaminat med porøsitet (in danish). Master's thesis, The Technical University of Denmark.

Budiansky, B., 1983. Micromechanics. Computers & Structures 16 (1-4), 3–12.

Chau, K. T., Rudnicki, J. W., 1990. Bifurcations of compressible pressure-sensitive materials in plane strain tension and compression. Journal of the Mechanics and Physics of Solids 38 (6), 875–898.

Christoffersen, J., Jensen, H. M., 1996. Kink band analysis accounting for the microstructure of fiber reinforced materials. Mechanics of Materials 24 (4), 305–315.

Cook, R. D., 2001. Concepts and Applications of Finite Element Analysis, 4th Edition. Wiley.

Davidson, P., Pineda, E. J., Heinrich, C., Waas, A. M., 2013. A Unified Model for Predicting the Open Hole Tensile and Compressive Strengths of Composite Laminates for Aerospace Applications. In: 54th AIAA/ASME/ASCE/AHS/ASC Structures, Structural Dynamics, and Materials Conference. pp. 1–26.

Dugdale, D. S., 1960. Yielding of steel sheets containing slits. Journal of the Mechanics and Physics of Solids 8 (2), 100–104.

Faruk, O., Bledzki, A. K., Fink, H. P., Sain, M., 2012. Biocomposites reinforced with natural fibers: 2000 - 2010. Progress in Polymer Science 37 (11), 1552–1596.

Fleck, N., Budiansky, B., 1991. Compressive failure of fibre composites due to microbuckling. Inelastic Deformation of Composite Materials, 235–274.

Fleck, N. A., 1997. Compressive failure of fibre composites. Advances in Applied Mechanics 33, 43–117.

Fleck, N. A., Shu, J. Y., 1995. Microbuckle initiation in fibre composites: a finite element study. Journal of the Mechanics and Physics of Solids 43 (12), 1887 – 1918.

Fleck, N. A., Sivashanker, S., Sutcliffe, M. P. F., 1997. Compressive failure of composites due to microbuckle growth. European Journal of Mechanics - A/Solids 16 (Special issue), 65–82.

Gutkin, R., Pinho, S. T., Robinson, P., Curtis, P. T., 2010. Micromechanical modelling of shear-driven fibre compressive failure and of fibre kinking for failure envelope generation in CFRP laminates. Composites Science and Technology 70 (8), 1214–1222.

Guynn, E. G., Bradley, W. L., Elber, W., 1989. Micromechanics of compression failures in open hole composite laminates. Composite Materials: Fatigue and Fracture, ASTM STP 1012 2, 118–136.

Hancox, N. L., 1975. The compression strength of unidirectional carbon fibre reinforced plastic. Journal of Materials Science 10 (2), 234–242.

Hutchinson, J. W., 1973. Finite Strain Analysis of Elastic-Plastic Solids and Structures. Numerical Solutions of Non-Linear Structural Problems 6, 17–29.

Hutchinson, J. W., Suo, Z., 1992. Mixed mode cracking in layered materials. Advances in Applied Mechanics 29, 63–191.

Jensen, H. M., 1999. Analysis of compressive failure of layered materials by kink band broadening. International Journal of Solids and Structures 36 (23), 3427–3441.

Jensen, H. M., Christoffersen, J., 1997. Kink band formation in fiber reinforced materials. Journal of the Mechanics and Physics of Solids 45 (7), 1121–1136.

Krenk, S., 2009. Non-linear Modeling and Analysis of Solids and Structures. Cambridge University Press.

Kyriakides, S., Arseculeratne, R., Perry, E. J., Liechti, K. M., 1995. On the compressive failure of fiber reinforced composites. International Journal of Solids and Structures 32 (617), 689–738.

Laffan, M. J., Pinho, S. T., Robinson, P., Iannucci, L., McMillan, A. J., 2012. Measurement of the fracture toughness associated with the longitudinal fibre compressive failure mode of laminated composites. Composites Part A: Applied Science and Manufacturing 43 (11), 1930–1938.

Laffan, M. J., Pinho, S. T., Robinson, P., McMillan, A. J., 2011. Translaminar fracture toughness: The critical notch tip radius of 0° plies in CFRP. Composites Science and Technology 72 (1), 97–102.

McMeeking, R. M., Rice, J. R., 1975. Finite-element formulations for problems of large elastic-plastic deformation. International Journal of Solids and Structures 11 (5), 601–616.

Moran, P. M., Liu, X. H., Shih, C. F., 1995. Kink band formation and band broadening in fiber composites under compressive loading. Acta Metallurgica et Materialia 43 (8), 2943–2958.

Moran, P. M., Shih, C. F., 1998. Kink band propagation and broadening in ductile matrix fiber composites: Experiments and analysis. International Journal of Solids and Structures 35 (15), 1709 – 1722.

Pane, I., Jensen, H. M., 2004. Plane strain bifurcation and its relation to kinkband formation in layered materials. European Journal of Mechanics - A/Solids 23 (3), 359–371.

Paris, P. C., Sih, G. C., 1964. Stress analysis of cracks. Fracture Toughness Testing and its Applications, ASTM STP 381 (1), 30 – 82.

Paterson, M. S., Weiss, L. E., 1966. Experimental deformation and folding in phyllite. Geological Society of America 77 (4), 343–374.

Prabhakar, P., Waas, A. M., 2013. Interaction between kinking and splitting in the compressive failure of unidirectional fiber reinforced laminated composites. Composite Structures 98, 85–92.

Rice, J. R., 1968. A path independent integral and the approximate analysis of strain concentration by notches and cracks. Journal of Applied Mechanics 35, 379–386.

Rice, J. R., 1976. The localization of plastic deformation. Theoretical and Applied Mechanics, W.T., Koiter ed. 1 (North-Holland Publishing Company), 207 – 220.

76

Riks, E., 1979. An Incremental Approach to the Solution of Snapping and Buckling Problems. International Journal of Solids and Structures 15 (7), 529–551.

Romanowicz, M., 2013. Initiation of kink bands from regions of higher misalignment in carbon fiber-reinforced polymers. Journal of Composite Materials 48 (19), 2387–2399.

Rosen, B. W., 1965. Mechanics of Composite Strengthening. In: Fiber Composite Materials. American Society for Metals, Metals Park, Ohio, pp. 37–75.

Soutis, C., Fleck, N. A., Smith, P. A., 1991. Failure prediction technique for compression loaded carbon fibre-epoxy laminate with open holes. Journal of Composite Materials 25 (11), 1476 – 1498.

Sørensen, K. D., Mikkelsen, L. P., Jensen, H. M., 2009. User subroutine for compressive failure of composites. In: Simulia Customer Conference, London. pp. 618–632.

Sutcliffe, M. P. F., Fleck, N. A., 1994. Microbuckle propagation in carbon fibre-epoxy composites. Acta Metallurgica et Materialia 42 (7), 2219–2231.

Tvergaard, V., 1983. Plastic buckling of axially compressed circular cylindrical shells. Thin-Walled Structures 1, 139–163.

Tvergaard, V., 2001. Plasticity and Creep in Structural Materials. Technical University of Denmark, Department of Mechanical Engineering, Solid Mechanics.

Veluri, B., Jensen, H. M., 2011. Simulation of post failure response in fiber composites. In: ASME 2011 International Mechanical Engineering Congress & Exposition, Denver, Colorado. Vol. 8. pp. 1–8.

Vogler, T. J., Kyriakides, S., 2001. On the initiation and growth of kink bands in fiber composites: Part I. experiments. International Journal of Solids and Structures 38, 2639–2651.

Waas, A. M., Babcock, C. D., Knauss, W. G., 1990. An experimental study of compression failure of fibrous laminated composites in the presence of stress gradients. International Journal of Solids and Structures 26 (9-10), 1071–1098.

Wadee, M. A., Völlmecke, C., Haley, J. F., Yiatros, S., 2012. Geometric modelling of kink banding in laminated structures. Philosophical Transactions. Series A, Mathematical, Physical, and Engineering Sciences 370 (1965), 1827–49.

Wind, J. L., Steffensen, S., Jensen, H. M., 2014. Comparison of a composite model and an individually fiber and matrix discretized model for kink band formation. International Journal of Non-Linear Mechanics 67 (December), 319–325.

Yurgartis, S. W., 1987. Measurement of small angle fiber misalignments in continuous fiber composites. Composites Science and Technology 30 (4), 279–293.

Zidek, R., Völlmecke, C., 2014. On the influence of material non-linearities in geometric modeling of kink band instabilities in unidirectional fiber composites. International Journal of Non-Linear Mechanics 62 (June), 23–32.

Paper I

Wind, J. L., Steffensen, S., Jensen, H. M., 2014. Comparison of a composite model and an individually fiber and matrix discretized model for kink band formation. International Journal of Non-linear mechanics 67 (December), 319-325.

Comparison of a composite model and an individually fiber and matrix discretized model for kink band formation

Jens Lycke Wind, Søren Steffensen, Henrik Myhre Jensen

Aarhus University, Department of Engineering, Inge Lehmanns Gade 10, 8000 Aarhus C, Denmark

Abstract

Failure by kink band instability in a unidirectional fiber composite is analyzed. A micro mechanical discretized finite element model is used and compared to an existing composite constitutive model. The comparison is made in a fiber angle vs. applied compressive stress space. An investigation on the relation between the kink band angle and the fiber angle is conducted in the post buckling regime. The critical kink band angle is examined for different initial fiber misalignment angles.

Keywords: Kink bands, Strain localization, Fiber composites

1. Introduction

Unidirectional fiber composites subjected to compressive stress may fail by several different modes [1]. One of the main failure modes is plastic micro buckling which leads to a kink band instability. At kinking, a narrow band is formed into which strains localize. The phenomenon is seen in different anisotropic materials, and was observed in phyllite by Paterson and Weiss [2]. In the early work on fiber kinking, models were formulated treating the fibers as beams on an elastic foundation. Rosen's [3] model leads to the critical compressive stress for kink band formation being equal to the shear modulus of the matrix. Later Argon [4] formulated a model using the shearing yield stress of the matrix and the fiber misalignment to determine the critical stress. Budiansky [5] incorporated the effect of an elastic ideally plastic matrix containing previous results as special cases.

To analyze kink bands, Christoffersen and Jensen [6] developed a rate constitutive equation accounting for the micro structure of a unidirectional fiber composite. They treated the problem in the framework of localization of deformation [7]. The model allowed for arbitrary elastic-plastic behavior of the constituents, and it will be reviewed briefly later in the paper. The model was applied in a study of initial fiber misalignments [8] and solutions were obtained by a numerical scheme by increasing the fiber angle incrementally and satisfying equilibrium.

Recently Wadee et al. [9] developed a geometrical kink band model founded on potential energy principles. It was further developed by Zidek and Völlmecke [10] to include nonlinear material behavior of the matrix.

Another way of attacking the kink band problem is by making an individual fiber and matrix discretized finite element analysis. This was first done by Guynn et al. [11] where they modeled a fiber misalignment and by using periodic boundary conditions on the free edges captured the kinking stress. The disadvantage of this is that the angle of the kink band is locked at $0°$, which was recently investigated by Romanowicz [12] to have a significant influence of the global response of the composite. The same type of periodic boundary conditions was used again by Gutkin et al. [13] where they continued the analysis into the post kinking regime.

In [14] a 2D finite element scheme was used to model fiber misalignment with free edges in a geometrical and material nonlinear analysis to capture the strain localization in a kink band. They investigated different types of fiber misalignments, variable matrix volume fraction and the effect of material nonlinearity of the fibers which was found to affect the critical strain only. In [15] and [16] they further developed the model to take 3D effects into consideration by individual discretization of fibers and matrix in a 3D representative volume element.

Alternative formulations of kink band instabilities include the model in [17] based on elastic planar finite

deformation analysis.

The aim of this paper is to compare and validate the constitutive model made by Christoffersen and Jensen [6] with a finite element model comparable to [14]. The comparison is made for the kinking stress, the global response, the fiber angle in the kink band and the kink band orientation for different initial fiber misalignments.

2. Constitutive equations

It was observed in [6] and [14] that the critical stress was only slightly affected by nonlinearity in the fibers. Due to these findings, it is assumed in this paper that only the matrix behaves elastic-plastic, while the fibers remain elastic. It should be emphasized that it does not impose difficulties in the present analysis to include fiber non-linearities. However, since the main purpose of the present analysis is to compare with previous results where fibers were assumed linear elastic, this assumption is also introduced here. The plasticity of the matrix material is described by the J_2-flow theory with isotropic hardening. The time-independent constitutive tensor L_{ijkl} relating the Jaumann rate of Kirchhoff stresses $\hat{\tau}_{ij}$ to strain rate $\dot{\varepsilon}_{ij}$ is

$$\hat{\tau}_{ij} = L_{ijkl}\dot{\varepsilon}_{kl} \tag{1}$$

where the constitutive tensor L_{ijkl} for J_2-flow theory from [18] using a finite strain formulation (total Lagrangian) as in [19] is

$$
\begin{aligned}
L_{ijkl} =& \frac{E}{1+\nu}\left(\frac{1}{2}\left(G_{ik}G_{jl}+G_{il}G_{jk}\right) + \frac{\nu}{1-2\nu}G_{ij}G_{kl}\right.\\
&\left. -\beta^*\frac{3}{2}\frac{E/E_t - 1}{E/E_t - (1-2\nu)/3}\frac{s_{ij}s_{kl}}{\sigma_e^2}\right)\\
&-\frac{1}{2}\left(G_{ik}\tau_{jl}+G_{jk}\tau_{il}+G_{il}\tau_{jk}+G_{jl}\tau_{ik}\right)
\end{aligned}
\tag{2}
$$

where G_{ij} are the components of the metric tensor of the deformed configuration, E is the Young modulus of elasticity and E_t is the tangent modulus. s_{ij} are the components of the deviatoric stress tensors and is defined by Kirchhoff stresses τ_{ij} as

$$s_{ij} = \tau_{ij} - \frac{1}{3}G_{ij}G^{kl}\tau_{kl} \tag{3}$$

σ_e is the equivalent von Mises stress

$$\sigma_e = \sqrt{\frac{3}{2}G^{ik}G^{jl}s_{ij}s_{kl}} \tag{4}$$

The relation between Kirchhoff and Cauchy stresses is

$$\sigma_{ij} = \sqrt{\frac{g}{G}}\tau_{ij} \tag{5}$$

where g and G are the determinants of the metric tensor of the undeformed and deformed configuration, respectively. β^* is determined by

$$\beta^* = \begin{cases} 1 & \text{for } \sigma_e = (\sigma_e)_{\max} \text{ and } \dot{\sigma}_e \geq 0 \\ 0 & \text{for } \sigma_e < (\sigma_e)_{\max} \text{ or } \dot{\sigma}_e < 0 \end{cases} \tag{6}$$

The relation between the uniaxial logarithmic strain ε and the uniaxial Cauchy stress σ is described as a Ramberg-Osgood relation for the matrix material by

$$\varepsilon = \frac{\sigma}{E} + \frac{3\sigma^y}{7E}\left(\frac{\sigma}{\sigma^y}\right)^n \tag{7}$$

where σ^y is the yield stress and n is the hardening index. The tangent modulus E_t is determined by differentiation of (7). The actual values for the material parameters shown later are motivated by experimental findings in [14] for in-situ PEEK reinforced by carbon fibers tested uniaxially as well as in shear.

3. The discretized model for fiber composites

The finite element model is built in a comparable scheme to [14]. The commercial finite element code Marc from MSC Software is used for the analysis. The numerical scheme is chosen as an updated Lagrangian formulation. The model is built of alternating fiber and matrix layers with one 8 node bi-quadratic plane strain element per individual fiber and matrix layer. It was observed by Borg [20] that using 1 element per layer compared to 3 gave a deviation on the kink stress by only 3 %. The grid in [14] is also made of 1 element per layer. A convergence study is conducted to determine the necessary number of fiber/matrix layers in a representative volume element that captures the kinking and the steady state post kinking stress accurately. An illustration of the model is shown in Figure 1. The imperfection to simulate a fiber misalignment is imposed as a cosine function in the area marked by the dashed lines in Figure 1

$$x_2 = \frac{h}{2}\left(1 - cos\left(\frac{\pi x_1}{b}\right)\right) \tag{8}$$

where h is determined from the misalignment angle ϕ_0

$$h = \frac{2b\tan(\phi_0)}{\pi} \tag{9}$$

and b is the width of the imperfection. The angle of the imperfection β determines in combination with b the area where the imperfection from (8) applies. The fibers outside this area are straight. When $b = L_0$ there are
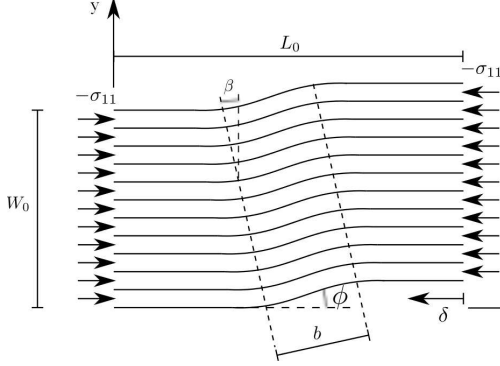
2

Figure 1: Numerical setup.

no straight fibers and the misalignment is applied to the whole model. This type of misalignment is in this paper referred to as *global* imperfection. When $b < L_0$, the misalignment is referred to as *local* imperfection.

The fiber volume fraction c^f determines the matrix volume fraction c^m by

$$c^f + c^m = 1 \qquad (10)$$

which may change during deformation as the strains and material properties in the fibers and matrix differ. The width, W_0, and the length, L_0, are fixed values in the analysis. This leads to the width of each individual fiber being a variable determined by the number of fibers in the model and c_f. The fiber width then controls the mesh of the model while the matrix width also is controlled by the fiber width.

Since the equilibrium path may experience snap-through and snap-back, the numerical technique for incremental solution is chosen as the arc-length method first introduced by Riks [21]. A linear constraint is chosen as described in [22] so that the sub-increment $(\delta u, \delta f)$ lies in a hyperplane orthogonal to the current total increment $(\Delta u, \Delta f)$ and is expressed by the condition

$$(\Delta u, \Delta f) \cdot (\delta u, \delta f) = 0 \qquad (11)$$

where (u) is the displacement vector and (f) is the force vector. This load factor increment is calculated as

$$\delta \xi = -\frac{\Delta u^T \delta u_r}{\Delta u^T \Delta u_1} \qquad (12)$$

where δu_r is the sub-increment residual displacement vector and Δu_1 is the initial displacement vector in the current increment.

4. The constitutive model for fiber composites

An expression is obtained for the composite moduli as a function of constituent moduli and volume fractions in [6]. The plane constitutive model is based on continuity and equilibrium across layer interfaces on a constituent level rather that on a global composite level. In the following superscript c denotes constituents (fiber or matrix) and properties without superscript denote composite properties. Assume that the fibers are orientated along the x_1 axis (see Figure 1) The constitutive relation between the nominal stress rates $\dot{s}_{ij}$ and the gradients of displacement rates $v_{i,j}$ is

$$\dot{s}_{ij}^c = C_{ijkl}^c v_{k,l}^c \ , \ i, j, k, l \in \{1, 2\} \qquad (13)$$

for the constituents (matrix and fiber individually) where C_{ijkl}^c is the tensor of nominal moduli. With the state of Cauchy stresses σ_{ij}^c of the fiber and matrix assumed known, the constitutive tensor can be expressed as

$$C_{ijkl}^c = L_{ijkl}^c - \tfrac{1}{2}\delta_{il}\sigma_{kj}^c - \tfrac{1}{2}\delta_{ik}\sigma_{lj}^c - \tfrac{1}{2}\sigma_{il}^c\delta_{kj} + \tfrac{1}{2}\sigma_{ik}^c\delta_{lj} \ (14)$$

written in an updated Lagrangian formulation. Symmetry conditions apply for L_{ijkl}^c as

$$L_{ijkl}^c = L_{ijlk}^c = L_{jikl}^c = L_{klij}^c \qquad (15)$$

Equation (13) may for convenience be written as

$$\dot{s}_\alpha^c = C_{\alpha\beta}^c v_{,\beta}^c \ , \ \alpha, \beta \in \{1, 2\} \qquad (16)$$

where the vectors $\dot{s}^c$ denotes the rates of nominal stresses by

$$\dot{s}_1^c = \begin{Bmatrix} s_{11}^c \\ s_{12}^c \end{Bmatrix} \ , \ \dot{s}_2^c = \begin{Bmatrix} s_{21}^c \\ s_{22}^c \end{Bmatrix} \qquad (17)$$

and the vector v^c is

$$v^c = \begin{Bmatrix} v_1^c \\ v_2^c \end{Bmatrix} \qquad (18)$$

The matrix $C_{\alpha\beta}$ is decomposed as

$$C_{11}^c = \begin{bmatrix} L_{1111}^c - \sigma_{11}^c & L_{1112}^c - \sigma_{12}^c \\ L_{1211}^c - \sigma_{12}^c & L_{1212}^c - \frac{\sigma_{22}^c - \sigma_{11}^c}{2} \end{bmatrix},$$

$$C_{12}^c = \begin{bmatrix} L_{1112}^c & L_{1122}^c \\ L_{1212}^c - \frac{\sigma_{22}^c + \sigma_{11}^c}{2} & L_{1222}^c \end{bmatrix},$$

$$C_{21}^c = \begin{bmatrix} L_{1211}^c & L_{1212}^c - \frac{\sigma_{11}^c + \sigma_{22}^c}{2} \\ L_{2211}^c & L_{2212}^c \end{bmatrix},$$

$$C_{22}^c = \begin{bmatrix} L_{1212}^c - \frac{\sigma_{11}^c - \sigma_{22}^c}{2} & L_{1222}^c - \sigma_{12}^c \\ L_{2212}^c - \sigma_{12}^c & L_{2222}^c - \sigma_{22}^c \end{bmatrix} \qquad (19)$$

Three assumptions are introduced in [6]:

3

(A) Material lines parallel with the fibers are subjected to common stretching and rotations.

(B) Planes parallel with the fibers transmit identical tractions.

(C) The material of the constituents is elastic or elastic-plastic.

Assumption (A) corresponds to a Voigt estimate for effective material properties parallel with the fibers. It corresponds to that the displacement gradients $v^c_{,1}$ is common to both constituents

$$v^f_{,1} = v^m_{,1} = v_{,1} \qquad (20)$$

using the notation $v_{,1}$ without superscript which corresponds to the overall displacement gradient. For overall compatibility of a representative volume element

$$c^f v^f_{,2} + c^m v^m_{,2} = v_{,2} \qquad (21)$$

where c^f and c^m have the relation shown in (10).

Assumption (A) is not realistic perpendicular to the fibers for which reason assumption (B) is imposed which is the Reuss estimate for composites. This means that

$$\dot{s}^f_2 = \dot{s}^m_2 = \dot{s}_2 \qquad (22)$$

and for overall equilibrium

$$c^f \dot{s}^f_1 + c^m \dot{s}^m_1 = \dot{s} \qquad (23)$$

Balances of forces together with assumption B gives us

$$c^f \sigma^f_{11} + c^m \sigma^m_{11} = \sigma_{11} \ , \ \sigma^f_{12} = \sigma^m_{12} = \sigma_{12} \ , \ \sigma^f_{22} = \sigma^m_{22} = \sigma_{22} \qquad (24)$$

Assumption (C) indicate that (13) and (16) are valid. By combination of (16) and (20) - (24) it is shown in [6] that the overall constitutive equations for the composite can be written as

$$C_{\alpha\beta} = c^f C^f_{\alpha\beta} + c^m C^m_{\alpha\beta} - c^f c^m \left(C^f_{\alpha 2} - C^m_{\alpha 2} \right) C^{*-1}_{22} \left(C^f_{2\beta} - C^m_{2\beta} \right) \qquad (25)$$

where C^{*-1}_{22} denotes the inverse of the matrix

$$C^*_{22} = c^m C^f_{22} + c^f C^m_{22} \qquad (26)$$

The first two terms of (25) is the Voigt estimate. The rest of the terms is a correction according to assumption (B) perpendicular to the fibers.

The equations (20) - (24) takes care of the continuity between the fiber and matrix. The use of (25) in a kink band analysis requires continuity equations between base material and kink band [23]. The continuity of displacement gradients across the boundary requires that

$$v'_{i,j} t'_j t'_i = v_{i,j} t_j t_i \qquad v'_{i,j} t'_j n'_i = v_{i,j} t_j n_i \qquad (27)$$

where a primed symbol relates to the base material coordinates and an unprimed to the kink band coordinates. t_i, t'_i n_i and n'_i are, respectively, the unit tangent and the unit normal of the boundary between base material and kink band expressed in the base material coordinates and the kink band coordinates. Continuity of traction rates between the two regions requires that

$$\dot{s}'_{ij} n'_i n'_j = \dot{s}_{ij} n_i n_j \qquad \dot{s}'_{ij} n'_i t'_j = \dot{s}_{ij} n_i t_j \qquad (28)$$

Note that the kink band analysis using (27) and (28) is carried out on the overall composite level using (25) as constitutive equation.

5. Results

In Figure 2 several different stages at the load-displacement curve is marked. This to illustrate the deformations. The applied stress, $-\sigma_{11}$, is normalized with the elastic shear modulus, G, of the composite

$$G = \frac{G^m G^f}{v^f G^m + v^m G^f} \qquad (29)$$

Stage 0 refer to the initial stage which is shown in Figure 1. The deformation stages in connection with Figure 2 are shown in Figure 3. Stage (a) is where the equivalent
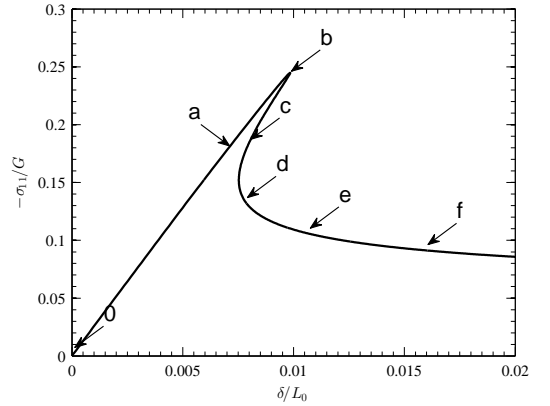

Figure 2: Applied normalized stress as a function of normalized end shortening.

von Mises stress of the matrix first exceeds the yielding stress. The zone of yielding is shown as plastic strains in the darker region for all the stages. At stage (b), the maximum stress is reached, i.e. the kinking stress.
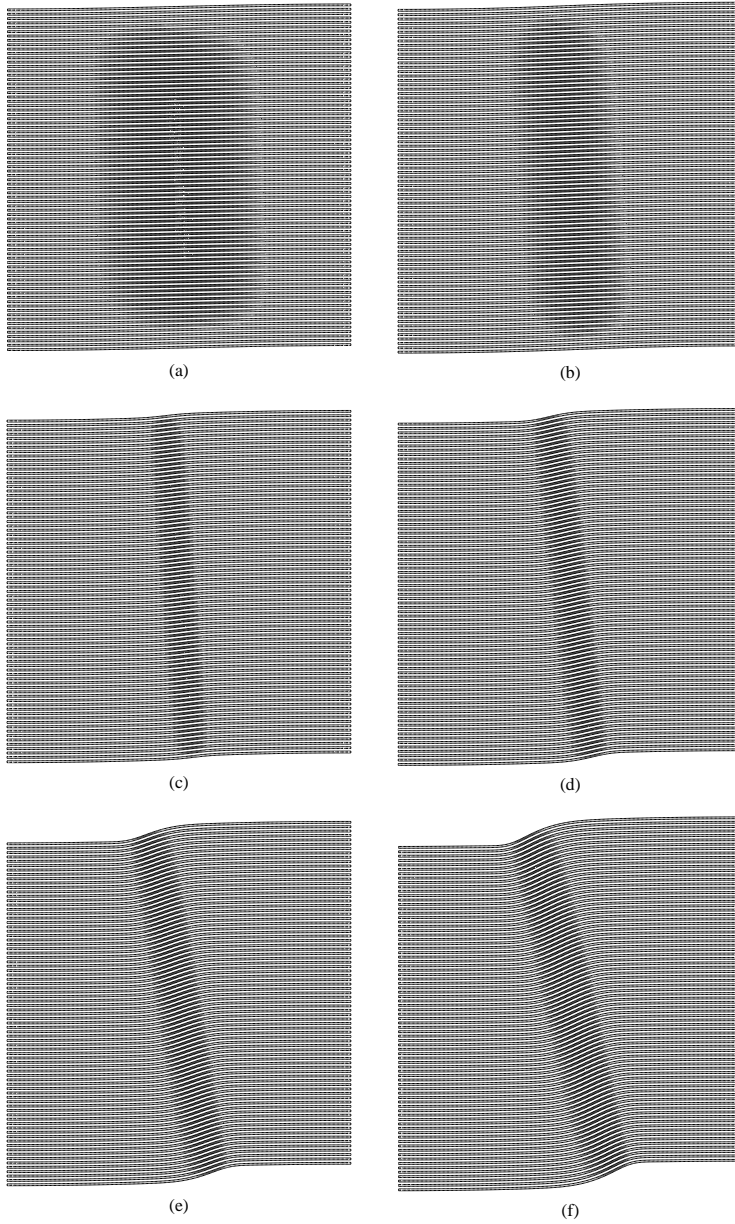
4

Figure 3: Deformation plots at different stages illustrating localization of deformation and rotation of kink band. The darker region is showing plastic strain in the matrix elements. The stages refer to Figure 2.

From stage (a) to (b) it is worth noting that the zone of plastic strains becomes smaller even before the kinking stress is reached. It is clear from Figure 2 that the load drops dramatically from stage (b) to (c) as well as the current length is increased due to snap-back behavior. This is due to the localization of deformation into a kink band which entails elastic unloading of the fibers outside the kink band. The amount of load drop and snap-back behavior is dependent on the imperfection but also on the material parameters of the matrix and the size of the specimen. In stage (c) the deformation is fully localized and the fibers start to rotate more rapidly. As the load keeps dropping from stage (c) to (d), the current length of the model decreases again. As the fibers rotate, the kink band angle β will also rotate. This is clear if a comparison is made between stage (c) and stage (f), for example. After stage (f) the load reaches a steady state value and a continuous compression will result in kink band broadening or a possible fiber breakage. In [24] and [25] they suggested a layered model in a friction layer context for predicting kink band broadening and kink band progression. Kink band broadening is also discussed in [23] and [26]. This is for further research and will be left out in the present work.

The material parameters used in the calculations are those obtained from [14] referring to a Ramberg-Osgood relation for the constituent uniaxial stress-strain curve in (7):

$$c^f = 0.6, \qquad E^f/E^m = 35, \qquad \nu^f = 0.263,$$
$$\nu^m = 0.356, \qquad \sigma^{y,m}/E^m = 0.013, \qquad n^m = 4 \quad (30)$$

To determine how many fibers n_f is necessary in the calculations, a convergence study is made in the applied stress $-\sigma_{11}$ as a function of fiber rotation ϕ space. The analysis is made with a global imperfection where $\phi_0 = 1°$. It can be seen in Figure 4 that only the critical load is slightly affected by n_f. A number of 100 fibers is chosen for the analysis.

5.1. Comparison with the constitutive model

In [8] it was shown that the critical kink band angle β_0^{cr} was not necessarily 0 in contrast to previous theoretical studies. Experimental obersevations also indicate inclined bands in most cases. This was shown in a $-\sigma_{11}$ vs ϕ plot for a fiber misalignment angle of $\phi_0 = 0.5°$ and $\phi_0 = 3°$. A comparison with this is made for a global and a local imperfection. The values of β_0 and b for the local imperfection was obtained by the following procedure: The global analysis was conducted, and the point where the kink band has localized was observed (stage (c) in Figure 2). Then β and b was noted at that stage
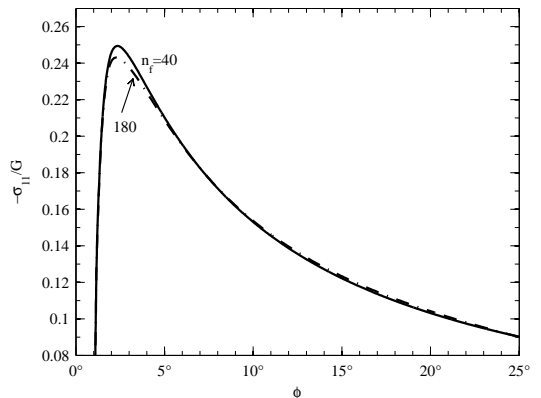

Figure 4: Applied normalized stress as a function of fiber rotation, ϕ, for two different number of fibers, $n_f = 40$ and $n_f = 180$. Only two curves are shown because $n_f = 80$ is almost identical to $n_f = 180$, so this is believed to be the converged curve.

and used as imperfection values for the local analysis. This means that the equilibrium from the global analysis controls the initial configuration of the local analysis. The comparison can be seen in Figures 5 and 6. The tendency of the curves is similar, but it can be observed that there is a difference in the values between the curves from [8] and the global and local analysis. The reason for this is due to the presence of a finite kink band width b in the global and the local analysis which is absent in [8].

A study on the kink band stress σ_{11}^{cr} as a function of initial misalignment angle ϕ_0 was also made by Jensen and Christoffersen [8]. In addition, the critical kink band angle β_0^{cr} was observed. A comparison with present results can be seen in Figure 7. The global analysis works as a lower bound, while the local analysis works as an upper bound. The reason for the increased deviation between the local and global analysis compared to [8] for small ϕ_0 is because of the J_2 flow rule used here. This results in a deviation compared to the J_2 deformation theory at very low imperfections which can also be seen in [23]. Like in [8] it can be observed that β_0^{cr} is increasing with increasing ϕ_0. The critical kink band angle β_0^{cr} for the local analysis is measured at the same time as the critical kink band stress (stage (b) in Figure 2), while for the global analysis it is measured just as the kink band has localized i.e. where it is first possible to observe a kink band (stage (c) in Figure 2).
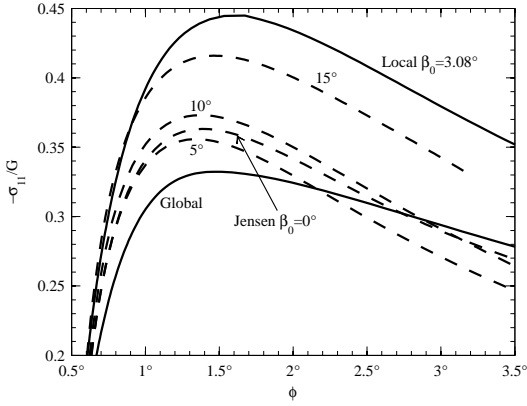
6

Figure 5: Applied normalized stress as a function of fiber rotation, ϕ, for initial imperfection $\phi_0 = 0.5°$. Jensen is from [8].
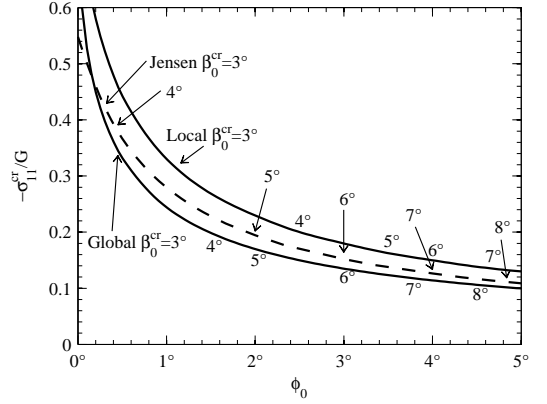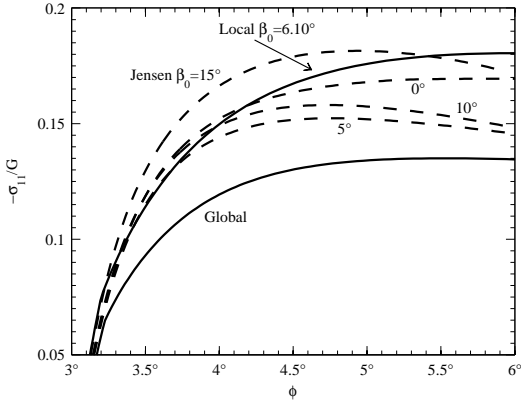

Figure 7: Applied normalized critical stress $-\sigma_{11}^{cr}$ as a function of initial fiber misalignment, ϕ_0, with critical kink band angle, β_0^{cr}, indicated. Jensen is from [8].

Figure 6: Applied normalized stress as a function of fiber rotation, ϕ, for initial imperfection $\phi_0 = 3°$. Jensen is from [8].
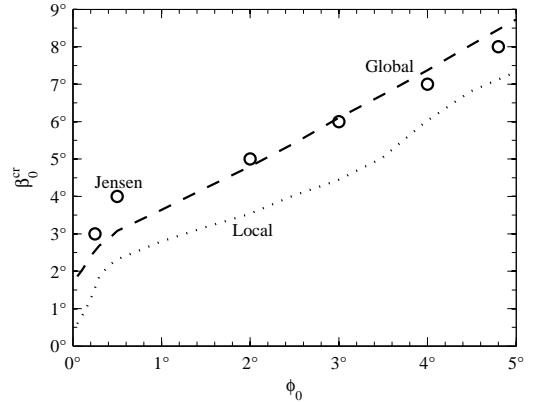
To clarify the relation between β_0^{cr} and ϕ_0 the relation is shown in Figure 8.

6. Discussion and conclusion

The relation between β and ϕ is shown in Figures 9 and 10 for the local and global analysis respectively. It can be observed in Figure 9 that β rotates with ϕ in a nearly linear manner when $\phi > 10°$ independent of

Figure 8: Critical kink band angle β_0^{cr} as a function of initial fiber misalignment. Jensen is from [8].

initial fiber misalignment ϕ_0. An approximate relation between β and ϕ has been observed experimentally in different materials to be [2]

$$\phi \approx 2\beta \qquad (31)$$

which is in good agreement with Figure 9 when $\phi > 10°$. For the global analysis in Figure 10 the same linearity can be observed. The relation in (31) thus only seems to apply for small initial fiber misalignment ϕ_0. Usually (31) is used as a lock-up condition corresponding to zero volumetric straining of the matrix material

[27]. In the large strain material response of the matrix there is no stiffening incorporated. Stiffening is known to happen for amorphous polymers (e.g. [28]) when exposed to large strain. With this effect included the relation between β and ϕ would act differently. This is beyond the scope of this paper and is left out.
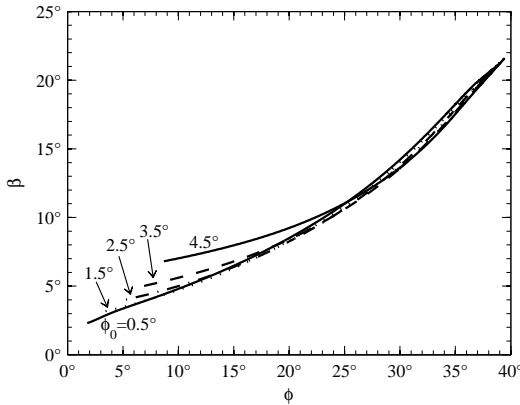

Figure 9: Kink band angle, β, as a function of fiber rotation, ϕ, with different initial fiber misalignment for the local analysis.
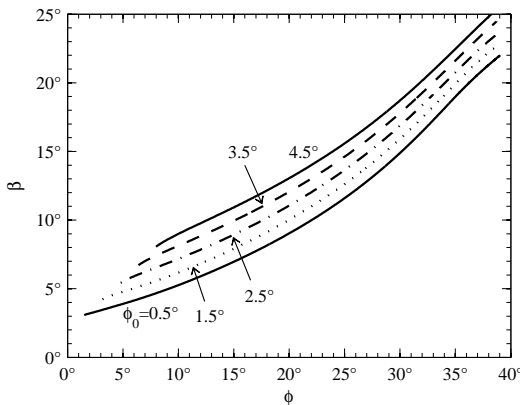

Figure 10: Kink band angle, β, as a function of fiber rotation, ϕ, with different initial fiber misalignment for the global analysis .

6.1. Comparison with the constitutive model

The comparison of the two models is made with that purpose of validating the constitutive model under plane strain conditions and a homogeneous compressive stress field in Figures 5 - 8. The discretized finite element approach has previously shown to be in good agreement with experimental observations and is used as a reference in the present work. A micro mechanical discretized finite element model has the disadvantage that it is impossible to use in a large structure while the constitutive model used in the finite element scheme is possible to use. Of course this comes with some assumptions, which have been outlined.

The width b in relation with the initial fiber angle ϕ_0 determines the size of the imperfection. With this in mind, it is difficult to make a direct comparison between the constitutive model and the discretized model in the applied stress vs. fiber angle space due to lack of information on kink band width in the constitutive model. The approach of introducing a global and then a local imperfection afterwards is a way of letting the equilibrium from the global imperfection analysis determine the size of the local imperfection. The global imperfection analysis works as a lower bound for the critical stress, while the local imperfection analysis works as an upper bound. This is valid for all values of ϕ_0 examined in the present work and indicates a good agreement between the two models.

It was shown in the implementation of the constitutive model in a finite element scheme by Sørensen et al. [29] that the post buckling regime was mesh dependent in an applied stress vs. end shortening space. The same applies for the discretized model and is due to the width of the kink band that forms. This controls the elastic unloading after the critical stress has been reached. The load path for the discretized model does converge towards the steady state load though. This makes good sense since this is mainly controlled by the material properties of the matrix. In this paper the fiber rotation is chosen instead of the end shortening as convergence parameter, due to a fast convergence on the whole load path.

Previous models e.g. [8] and [27] assume fixed initial kink band angles which may evolve with the general state outside the kink band. The present results, where a less constrained rotation of the band with increasing fiber rotations are observed, could be applied in improved simplified models such as these in [8] and [27].

8

References

[1] N. A. Fleck, Compressive failure of fibre composites, Advances in Applied Mechanics 33 (1997) 43–117.

[2] M. S. Paterson, L. E. Weiss, Experimental deformation and folding in phyllite, Geological Society of America 77 (4) (1966) 343–374.

[3] B. W. Rosen, Mechanics of Composite Strengthening, in: Fiber Composite Materials, American Society for Metals, Metals Park, Ohio, 1965, pp. 37–75.

[4] A. S. Argon, Fracture of composites, Treatise on Materials Science and Technology 1 (1972) 79–114.

[5] B. Budiansky, Micromechanics, Computers & Structures 16 (1-4) (1983) 3–12.

[6] J. Christoffersen, H. M. Jensen, Kink band analysis accounting for the microstructure of fiber reinforced materials, Mechanics of Materials 24 (4) (1996) 305–315.

[7] J. R. Rice, The localization of plastic deformation, Theoretical and Applied Mechanics, W.T., Koiter ed. 1 (North-Holland Publishing Company) (1976) 207 – 220.

[8] H. M. Jensen, J. Christoffersen, Kink band formation in fiber reinforced materials, Journal of the Mechanics and Physics of Solids 45 (7) (1997) 1121–1136.

[9] M. A. Wadee, C. Völlmecke, J. F. Haley, S. Yiatros, Geometric modelling of kink banding in laminated structures., Philosophical Transactions. Series A, Mathematical, Physical, and Engineering Sciences 370 (1965) (2012) 1827–49.

[10] R. Zidek, C. Völlmecke, On the influence of material non-linearities in geometric modeling of kink band instabilities in unidirectional fiber composites, International Journal of Non-Linear Mechanics (2014) 1–10.

[11] E. G. Guynn, O. O. Ochoa, W. L. Bradley, A Parametric Study of Variables That Affect Fiber Microbuckling Initiation in Composite Laminates: Part 1-Analyses, Journal of Composite Materials 26 (11) (1992) 1594–1616.

[12] M. Romanowicz, Initiation of kink bands from regions of higher misalignment in carbon fiber-reinforced polymers, Journal of Composite Materials 48 (19) (2013) 2387–2399.

[13] R. Gutkin, S. T. Pinho, P. Robinson, P. T. Curtis, Micro-mechanical modelling of shear-driven fibre compressive failure and of fibre kinking for failure envelope generation in CFRP laminates, Composites Science and Technology 70 (8) (2010) 1214–1222.

[14] S. Kyriakides, R. Arseculeratne, E. J. Perry, K. M. Liechti, On the compressive failure of fiber reinforced composites, International Journal of Solids and Structures 32 (617) (1995) 689–738.

[15] T. J. Vogler, S. Y. Hsu, S. Kyriakides, On the initiation and growth of kink bands in fiber composites. Part II: analysis, International Journal of Solids and Structures 38 (2001) 2653–2682.

[16] T. J. Vogler, S. Kyriakides, On the initiation and growth of kink bands in fiber composites: Part I. experiments, International Journal of Solids and Structures 38 (2001) 2639–2651.

[17] J. Merodio, T. J. Pence, Kink surfaces in a directionally reinforced neo-Hookean material under plane deformation: II. Kink band stability and maximally dissipative band broadening, Journal of Elasticity 62 (2) (2001) 145–170.

[18] R. M. McMeeking, J. R. Rice, Finite-element formulations for problems of large elastic-plastic deformation, International Journal of Solids and Structures 11 (5) (1975) 601–616.

[19] J. W. Hutchinson, Finite Strain Analysis of Elastic-Plastic Solids and Structures, Numerical Solutions of Non-Linear Structural Problems 6 (1973) 17–29.

[20] U. Borg, Tryk og trækstyrke af fiberlaminat med porøsitet (in danish), Master's thesis, The Technical University of Denmark (2003).

[21] E. Riks, An Incremental Approach to the Solution of Snapping and Buckling Problems, International Journal of Solids and Structures 15 (7) (1979) 529–551.

[22] S. Krenk, Non-linear Modeling and Analysis of Solids and Structures, Cambridge University Press, 2009.

[23] H. M. Jensen, Analysis of compressive failure of layered materials by kink band broadening, International Journal of Solids and Structures 36 (23) (1999) 3427–3441.

[24] M. A. Wadee, G. W. Hunt, M. A. Peletier, Kink band instability in layered structures, Journal of the Mechanics and Physics of Solids 52 (5) (2004) 1071–1091.

[25] M. A. Wadee, R. Edmunds, Kink band propagation in layered structures, Journal of the Mechanics and Physics of Solids 53 (9) (2005) 2017–2035.

[26] P. M. Moran, X. H. Liu, C. F. Shih, Kink band formation and band broadening in fiber composites under compressive loading, Acta Metallurgica et Materialia 43 (8) (1995) 2943–2958.

[27] N. Fleck, B. Budiansky, Compressive failure of fibre composites due to microbuckling, Inelastic Deformation of Composite Materials (1991) 235–274.

[28] E. M. Arruda, M. C. Boyce, Evolution of plastic anisotropy in amorphous polymers during finite straining, International Journal of Plasticity 9 (1993) 697 – 720.

[29] K. D. Sørensen, L. P. Mikkelsen, H. M. Jensen, User subroutine for compressive failure of composites, in: Simulia Customer Conference, London, 2009, pp. 618–632.

Paper II

Wind, J. L., Waas, A. M., Jensen, H. M. Initiation of failure at notches in unidirectional fiber composites. Submitted to Composite Structures.

Initiation of failure at notches in unidirectional fiber composites

Jens L. Wind[a], Anthony M. Waas[b], Henrik M. Jensen[a]

[a]*Aarhus University, Department of Engineering, Inge Lehmanns Gade 10, 8000 Aarhus C, Denmark*
[b]*University of Michigan, Aerospace Engineering, FXB Building, 1320 Beal Avenue, Ann Arbor, MI 48109-2140, USA*

Abstract

A four point bend setup is used in observing compressive damage initiation in a unidirectional carbon/epoxy single edge notch beam. Damage initiation is observed in 8 specimens with a camera during testing and the test is stopped when damage occurs. Post observation of the polished specimens showed a micro buckling instability at the notch tip in 5 specimens and splitting in 3. The damage initiation is modeled as an individually discretized fiber and matrix 2D plane strain finite element model. To reduce calculation time, the superelement approach is used to model the whole beam except a small local area at the notch tip. A good agreement of the critical force is found between the analysis and the experiments with a deviation of 4 %. A comparison is made with the compressive crack approach with a deviation of 9 % on the critical energy release rate.

Keywords: Fiber composites, Kink bands, Superelements, FEM based failure

1. Introduction

Unidirectional fiber composites subjected to compressive stress may fail by several different modes [1]. One of the main failure modes is plastic micro buckling which leads to a kink band instability. It is difficult to conduct a pure compression test in an un-notched unidirectional composite to observe a kink band and its propagation. When the critical kinking stress is reached, a dramatic load drop will in most cases result in a broken specimen. If a notched specimen is chosen, the stress concentration at the notch tip will force the failure to occur there, while there is still load bearing capacity left in the rest of the specimen.

Moran and Shih [2] succeeded in tracking the end-shortening as a function of applied stress in a pure compression setup in a single edge notched unidirectional IM7/PEEK composite. This behavior was similar to that observed by Kyriakides et al. [3], where they also individually modeled the fibers and the matrix in a unidirectional composite using a 2D finite element scheme. Vogler and Kyriakides [4] observed the same stable phenomenon in an AS4/PEEK composite in a biaxial test setup. They captured micrographs showing the evolution of the kink band as well.

Guynn [5] viewed the damaged zone as crack with a plastic zone in a carbon/epoxy composite. He applied the Dugdale [6] model to predict the size of the buckled region in multilayered composites. In the Dugdale model a constant normal stress is applied in the damage zone. It was concluded that this did not accurately predict the size of the damaged zone. Soutis et al. [7] applied a stress which varied linearly with the crack displacement and resulted in improved accuracy.

Waas et al. [8] introduced a circular hole in a rectangular multilayered carbon/epoxy composite. This produced a stress gradient at the hole surface in which the failure initiated. The failure mode was fiber microbuckling in the 0° ply approximately perpendicular to the loading direction surrounded by delamination.

Sutcliffe and Fleck [9] used a large scale bridging model for propagating microbuckles in unidirectional carbon/epoxy fiber composites with a rectangular hole using a constant bridging stress and a constant crack tip toughness. The model was an in-plane and out-of-plane microbuckle as mode II and mode I cracks, respectively. They compared the microbuckle displacement with experimental observations. To avoid splitting they cut a notch along the fiber direction. Fleck et al. [10] further investigated the idea in multilayered composites both analytically and experimentally. The materials used was thermoplastic PEEK matrix reinforced by AS4 and IM8 carbon fibers and Toray T800 carbon fibers in epoxy. They discovered experimentally that the fiber strength had a minor effect in the propagation behavior as well.

Laffan et al. [11] measured the fracture toughness associated with the 0° ply in a multi layered IM7/8552
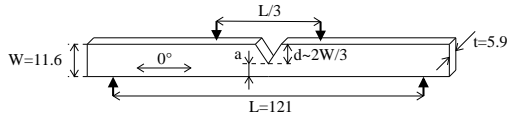
Figure 1: Four point bend specimen dimensions in mm.

composite. They used compact tension specimens to track down the critical notch tip radius for a correct measurement of the fracture toughness. Laffan et al. [12] used that information to measure the fracture toughness in a unidirectional IM7/8552 composite using a single edge notch beam in a plane stress four point bend setup.

To view the damaged zone as a crack is a way to observe what happens on a macro-mechanical level. To know what happens at the micro-mechanical level, modeling of the material instability of the fibers and matrix individually is an option. Ahn and Waas [13] used a global-local approach to model the material instability in a square plate with a circular hole in a biaxial compression setup. They used an approach of a notched laminate of infinite extent to compute the displacement field of the rectangular local region. An imperfection was imposed as a scaling of the first modal vector from a linear eigenvalue analysis. The size of the scaling was determined by the maximum angle of the fibers. A similar approach was used by Davidson et al. [14] in a rectangular plate with a circular cutout. The procedure was to use the displacement and forces on the boundaries of the local model from a global linear static analysis as an input to a local nonlinear static analysis.

In Laffan et al. [12] they viewed the failure as a crack. The scope of this paper is to see the failure as a material instability instead of a crack. The method is to experimentally detect initiation of fiber micro buckling in a unidirectional fiber composite. A stable failure is desired so the deformation of the composite at the material level can be observed. A finite element model is presented to predict the failure initiation and to verify the failure initiation as fiber micro buckling.

2. Materials and method

The material system used is carbon fiber reinforced plastic IM7/8552 unidirectional prepreg. Eight specimens were cut using a water jet in the dimensions shown in Fig. 1. Notched unidirectional carbon/epoxy composites in compression are prone to splitting. Before the present test, the depth, d, of the the notch was investigated to see what effect on splitting the depth has.
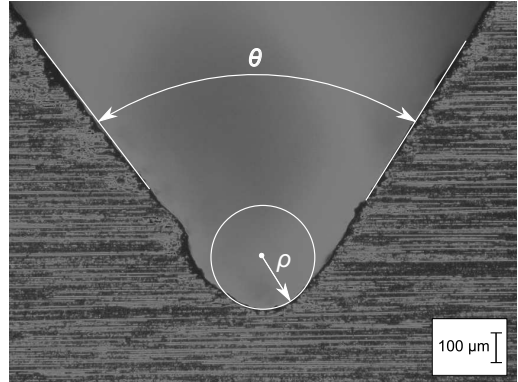

Figure 2: Picture taken by microscope before test showing notch tip.

Three depths were examined; $d \approx W/3$, $d \approx W/2$ and $d \approx 2W/3$. It was found that splitting happened rarely in specimens with $d \approx 2W/3$, and so this configuration was chosen for further study.

The notch was prepared using a slow rotating disc saw with a diamond coated disc. Two cuts were made forming an angle at $\theta \approx 67°$. The shape of the disc and the angle of the cut determines the radius, ρ, at the notch tip. ρ was measured in a microscope to be $\rho = 196 \pm 15\mu m$. In [11] the critical notch tip radius for measuring fracture toughness was found to be $\rho \leq 250\mu m$. The depth of the cut expressed by the remaining width, a, was measured as well to be $a = 3.82 \pm 0.072mm$. The specimens were polished before the test for a better observation of the failure initiation.

A four point bend (4PB) setup was implemented in an Instron testing machine. Glass plates was clamped on the sides using C-clamps for imposing a plane strain condition and to ensure that failure will happen in-plane. The clamping force is unknown, but preliminary tests showed that only a small clamping force was necessary for keeping the deformation in-plane. The test was quasi static using a loading rate of $0.6mm/min$. A camera was set up to take pictures of the notch tip every second for post observations of damage initiation. The test was stopped just after visual inspection of damage using the camera. After unloading of the specimen, the notch tip was polished and examined using a microscope.
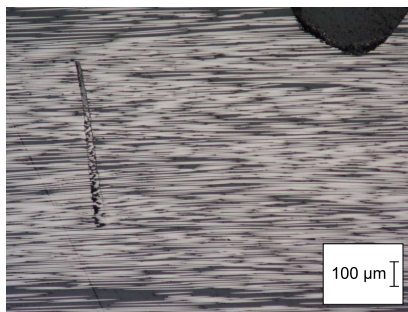
The failure in all the tests happened rapidly which means that initiation was not possible to observe. The camera taking pictures during the test did not have a sufficient magnification to observe micro mechanical initi-
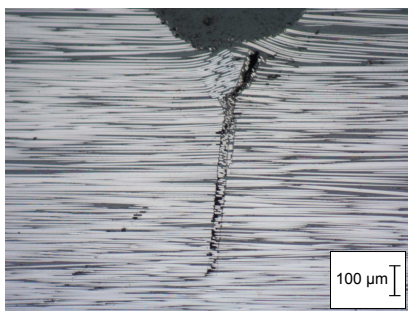
(a)

(b)

(c)

(d)

Figure 3: Four different type of failures after unloading.
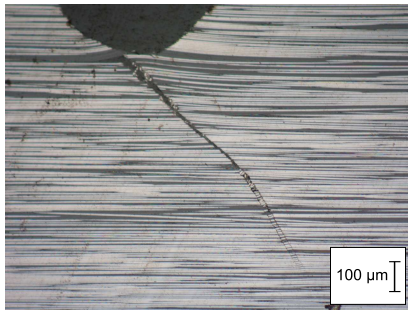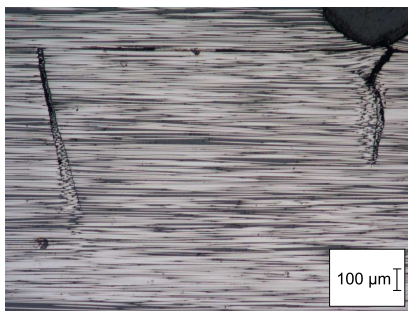
ation. Post observation of the unloaded polished specimens showed in five cases one common indicator of initiation of failure; namely micro buckling at the notch tip. In the three other cases splitting happened before micro buckling. In Fig. 3(a), 3(b) and 3(d), a failure at the notch tip can be observed. It is believed that micro buckling happens first followed by different types of subsequent post buckling damage. In Fig. 3(a) a compression crack can be seen at an angle $\approx 45°$ which was also seen by Hancox [15]. In Fig. 3(b) micro buckling appeared first followed by a subsequent splitting. In Fig. 3(c) splitting happened before micro buckling and therefore no micro buckling at the notch tip can be observed. In Fig. 3(d) the most common type of failure is seen; micro buckling at the notch tip followed by a kink band formation.

3. Analysis

In the experiments it was shown that fibers break just after damage has initiated. It is assumed that fiber micro buckling occurs before fiber breakage. The objective of this analysis is to predict the load, F, where fiber micro buckling appears, e.g. before fiber breakage. The geometry is made from the averaged dimensions of the test specimens, but since only small deviations are present in the measured value of ρ, θ and a, only minimal deviations in the results would be expected.

A 2D plane strain finite element analysis is conducted using a two step procedure as shown in Fig. 4.

Step 1: The part is divided into two regions; beam and local. The beam region is the whole part except for the local region discretized with a coarse mesh. The local region is a small region around the notch tip discretized with one element per fiber and matrix individually. This is done in order to keep the same local mesh in step 2 due to degree of freedom (DOF) numbering. Eight node bi-quadratic elements are used for both regions. The material parameters for both regions in step 1 is 2D orthotropic. The measured orthotropic material parameters for the composites can be seen in Table 1.

The DOFs associated with the beam region is being condensed except for the DOFs where F needs to be applied. The last band of elements from the beam region (and their DOFs) adjacent to the local region is being kept as well. A superelement is made for use in step 2.

In step 2 the previous established superelement is being used as input. The superelement is linear and will stay linear in this nonlinear analysis. The superelement is attached to the nodes on the boundary of the last band of elements from the beam region shown in Fig. 4. A

3
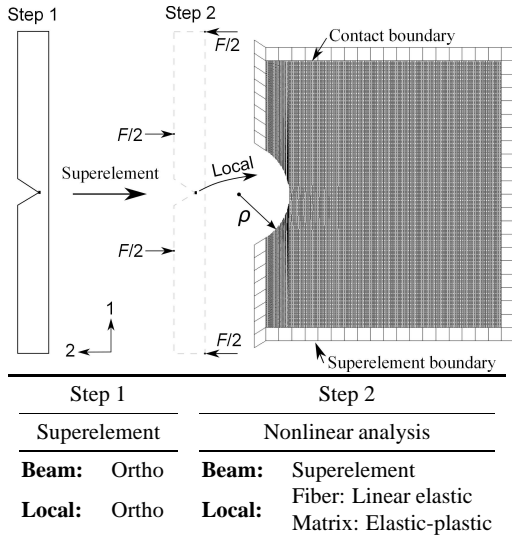
Figure 4: FEM workflow.

	Orthotropic	Isotropic
E_{11} [MPa]	131090	-
E_{22} [MPa]	72040	-
G_{12} [MPa]	48700	-
ν_{12}	0.34	-
E_f [MPa]	-	276000
E_m [MPa]	-	4080
ν_f	-	0.3
ν_m	-	0.38
σ^y [MPa]	-	90
n	-	4

Table 1: Material parameters used in orthotropic and isotropic ananlysis.

node-to-segment glued contact is made on the boundary between the local region and the last band elements. Applying this approach avoids contact between the superelement and the local region. The mesh in the local region is the same as in step 1. The local region is built in a similar way in [16] where the fiber diameter, d_f, determines in relation with the number of fibers, n_f, and the fiber volume fraction, c_f, the width, W_0, of the local region

$$W_0 = \frac{d_f n_f}{c_f} \tag{1}$$

where $c_f = 0.587$, $n_f = 100$ and $d_f = 5.2\mu m$ in this analysis. The length of the local region is $L_0 = 1mm$. The semi-circle cut-out is made by use of a perfect circle with tangents corresponding to the cut angle. The material parameters for the fibers are changed to linear elastic isotropic with parameters supplied by Hexcel[1]. The material parameters for the matrix is changed to isotropic elastic-plastic material behavior described by a uniaxial Ramberg-Osgood relation

$$\varepsilon = \frac{\sigma}{E_m} + \frac{3\sigma^y}{7E_m}\left(\frac{\sigma}{\sigma^y}\right)^n \tag{2}$$

By differentiation of (2), the tangent modulus is obtained,

$$E_m^t = \frac{7E_m}{3n\left(\frac{\sigma}{\sigma^y}\right)^{n-1} + 7} \tag{3}$$

and by linear relation

$$G_m^t = \frac{E_m^t}{2(1 + \nu_m)} \tag{4}$$

E_m, σ_y and n is found by curvefitting using (4) to an in-situ measured shear stress vs. shear strain curve obtained from tensile tests on $[+45/-45]_s$ laminates. The fitting can be seen in Fig 5. Forces and constraints are applied on the DOFs that was kept from the condensation as can be seen on Fig. 4. The nonlinear commercial solver MSC Marc is used for the analysis. The arc-length algorithm first introduced by Riks [17] is used for the incremental solution. The J_2 flow theory of plasticity is applied.

4. Results

In the post observation of the unloaded specimens from the experiments, two different types of failures was observed. Five specimens failed by micro buckling at
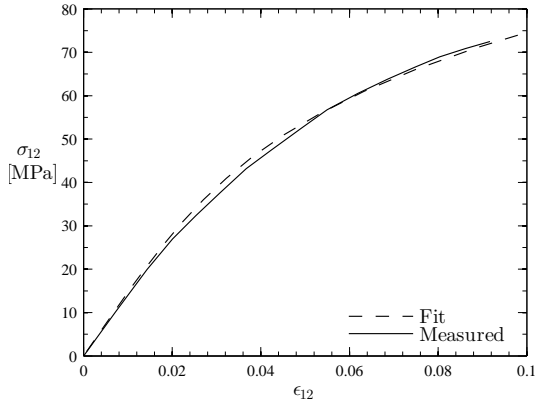
---

[1]http://www.hexcel.com/resources/datasheets/carbon-fiber-data-she

Figure 5: Curve fitting using (4) with measured in-situ matrix properties.

Figure 6: External applied force from experiments, F_E, normalized with critical force from the analysis, $F_{A,cr}$ with straight fibers, vs. displacement tracked by the testing machine, U_E. The color shows if the failure was splitting or micro buckling.

the notch tip and in some cases followed by splitting, while three specimens failed by splitting with no micro buckling at the notch tip observed. The force at which damage initiates was found by looking at the pictures taken by the camera to be $F_{E,cr} = 765 \pm 41\,N$. A comparison between the forces, F_E, from the experiments and the critical force from the analysis with straight fibers, $F_{A,cr}$, can be seen in Fig 6. The competition between splitting and kinking has been addressed by [18]. The force/displacement curve from the experiments has a stiffness drop in the beginning due to compliance of the test setup and crushing of the fibers under the rollers in the 4PB setup. Observing the external applied force from the analysis with straight fibers, F_A, normalized with the critical average force from experiments $F_{E,cr}$ in Fig. 7 shows a degradation in bending stiffness when damage occurs. This corresponds to a lowering of the moment of inertia of the beam. Due to this, the depth of the initial damage highly affects the remaining bending stiffness. As can be seen in Fig. 3 there is a difference between the damage depth in the experiments, so the degradation of bending stiffness would not be directly comparable if the tests was continued after damage has initiated. A more clear indicator of when damage initiates is by tracking the compressive force in the fiber just next to the notch tip. Since a contact condition is used between the beam and the local region, the contact force, F_C, is used as an indicator when damage initiates. F_C is measured as a function of $F_A/F_{E,cr}$ for straight fibers and for fibers with a waviness in Fig. 8. Micro buckling occurs when the force drops at the peak force.
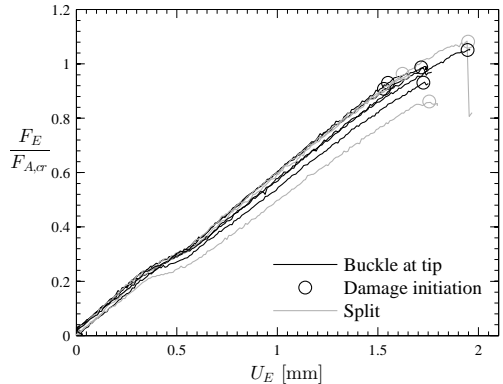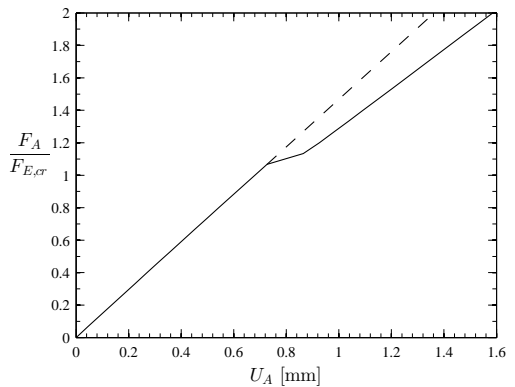

Figure 7: External applied force as a function of external displacement from finite element analysis with straight fibers.
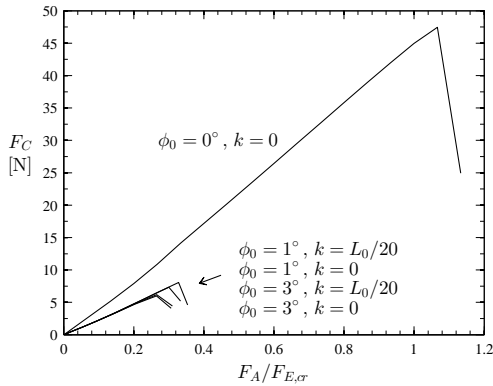
5

Figure 8: Contact force in the fiber just after the notch tip measured in the middle node as a function of external applied force.

Figure 9: Imperfection parameters shown with 30 fibers.

An imperfection is introduced to see what effect this has on the critical load and on the deformation profile. The imperfection is imposed as a fiber waviness in a specified region as shown in Fig. 9. The imperfection is applied as a decreasing cosine function in the area constrained by the height b and the offset from center k as

$$x_2 = \frac{h}{2}\left(1 - cos\left(\frac{2\pi x_1}{b}\right)\right)x_d \qquad (5)$$

where h is determined from the initial misalignment angle ϕ_0

$$h = \frac{2b\tan(\phi_0)}{\pi} \qquad (6)$$

x_d is a decaying function similar to the one used in Kyriakides et al. [3]

$$x_d = exp\left[\zeta\left(\frac{x_2}{\alpha W_0}\right)^2\right] \qquad (7)$$

Two types of imperfection are made; (I) central located imperfection ($k = 0$) and (II) imperfection offset from center with $k = L_0/20$. The reason for making an offset is to see if an asymmetric imperfection will result in a different critical load and deformation profile. Common parameters used are,

$$b = 0.2 \quad , \quad \zeta = ln(0.01) \quad , \quad \alpha = 0.3 \qquad (8)$$

It is clear that introducing a fiber waviness decreases the critical force. Introducing the offset of the waviness does not have a big effect on the results compared to no
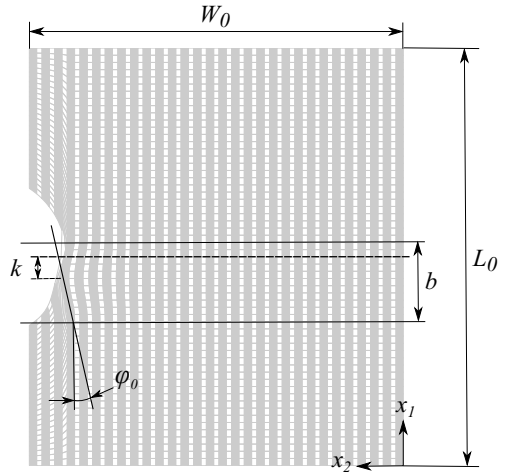
offset. It should be noted that changing the sign of ϕ_0 will result in a critical force comparable to the one with straight fibers.

Comparison of the deformation profile between the specimens failed by micro buckling at the notch tip (e.g. Fig. 3(d)) and the analysis in Fig. 10 shows similar behavior. A micro buckle at the free edge in the notch tip can be observed in both figures. In the experimental pictures the fibers are broken though, but the deformation profile is comparable to the deformation profile from the analysis. In the analysis with fiber waviness, the deformation profile at the critical force is comparable to the one with straight fibers.

5. Discussion

In [12] they found the mode I critical energy release rate when treating the damage as a compressive crack under plane stress conditions. To compare this result with the critical load $F_{E,cr}$ found in this study using plane strain condition, the J-integral approach introduced by Rice [19] is used. When a rounded crack tip is present, the relation between the critical stress intensity factor $K_{I,cr}$ and the notch tip radius ρ is

$$K_{I,cr} \leq \sigma_{max}\sqrt{\rho} \qquad (9)$$

If a constant stress along the edge exist, the equality in (9) holds true. Using the relation between $G_{I,cr}$ and $K_{I,cr}$
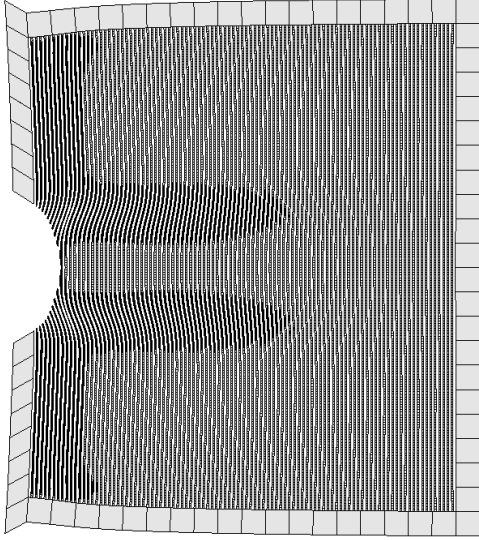
6

Figure 10: Deformation upscaled 3 times from finite element analysis with straight fibers at critical force where fiber elements are hidden. The darker region is showing plastic strain in the matrix elements.

from [20]

$$G_{I,cr} = \frac{K_{I,cr}^2}{\sqrt{2E_{11}E_{22}}} \sqrt{\sqrt{\frac{E_{11}}{E_{22}}} + \frac{E_{11}}{2G_{12}} - \nu_{12}} \quad (10)$$

a comparison with [12] can be made. The maximum stress at the rounded notch tip with the radius ρ is found using a Voigt estimate of Youngs modulus for the composite as E_c

$$E_c = c_f E_f + c_m E_m \quad (11)$$

which is suitable in this analysis since the fibers are in the direction of the loading. For Poisson's ratio a Voigt estimate is used as well. The critical applied force from the analysis with straight fibers $F_{A,cr}$ is applied to the model and a linear elastic analysis is conducted to extract the maximum stress σ_{max} at the notch tip boundary. The compressive stress profile at the notch tip can be seen in Fig. 11. The maximum stress, σ_{max} is noted and $G_{I,cr}$ can be calculated using (9) and (10) to be

$$G_{I,cr} = 28.3\,kJ/m^2 \quad (12)$$

This is a higher critical energy release rate than the averaged value from [12] which was $25.9 \pm 4.8\,kJ/m^2$ but
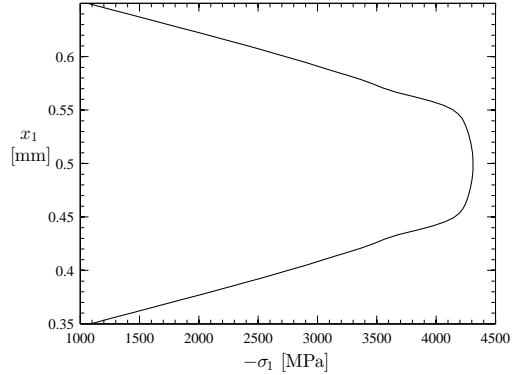

Figure 11: Compressive stress $-\sigma_1$ as a function of position x_1 in the notch tip.

within the deviation. This result is very satisfying since two different approaches of calculating $G_{I,cr}$ and different experiments gives an almost identical result. Using (9) results in a lower bound of $K_{I,cr}$ but since the upper bound estimate for E_C (Voigt estimate) in (11) is used in the extraction of σ_{max}, this will increase $K_{I,cr}$. If fiber waviness was introduced, a lower σ_{max} would also be expected.

6. Conclusion

Through comparison between the experimental and the finite element analysis, it is shown that using an individually fiber and matrix discretized finite element model, it is possible to predict an initiation force when micro buckling occurs. The finite element analysis overestimates the critical force by 4 % in the analysis with straight fibers compared to the experimental critical force for micro buckling. When observing fibers near the notch tip before the test it is only possible to observe very small fiber misalignment. If initial fiber waviness is introduced a decrease in the critical force can be observed. This is only present if the waviness is made with ϕ_0 being positive in Fig. 9. If ϕ_0 is chosen negative, a critical force similar to the analysis with straight fibers is observed.

By using the maximum stress at the notch tip when the critical force is applied in the analysis, a comparison is made with [12] where the damage is seen as a compressive crack. A 9 % difference in the critical energy release rate for a mode I crack is calculated. This shows that the critical energy release rate for this system repeated in [12] appears to be accurate. Consequently,

the four point bend method, as analyzed, have been used to measure the "equivalent" critical energy release rate for a fiber reinforced laminate.

Acknowledgements

References

[1] N. A. Fleck, Compressive failure of fibre composites, Advances in Applied Mechanics 33 (1997) 43–117.

[2] P. M. Moran, C. F. Shih, Kink band propagation and broadening in ductile matrix fiber composites: Experiments and analysis, International Journal of Solids and Structures 35 (15) (1998) 1709 – 1722.

[3] S. Kyriakides, R. Arseculeratne, E. J. Perry, K. M. Liechti, On the compressive failure of fiber reinforced composites, International Journal of Solids and Structures 32 (617) (1995) 689–738.

[4] T. J. Vogler, S. Kyriakides, On the initiation and growth of kink bands in fiber composites: Part I. experiments, International Journal of Solids and Structures 38 (2001) 2639–2651.

[5] E. G. Guynn, W. L. Bradley, W. Elber, Micromechanics of compression failures in open hole composite laminates, Composite Materials: Fatigue and Fracture, ASTM STP 1012 2 (1989) 118–136.

[6] D. S. Dugdale, Yielding of steel sheets containing slits, Journal of the Mechanics and Physics of Solids 8 (2) (1960) 100–104.

[7] C. Soutis, N. A. Fleck, P. A. Smith, Failure prediction technique for compression loaded carbon fibre-epoxy laminate with open holes, Journal of Composite Materials 25 (11) (1991) 1476 – 1498.

[8] A. M. Waas, C. D. Babcock, W. G. Knauss, An experimental study of compression failure of fibrous laminated composites in the presence of stress gradients, International Journal of Solids and Structures 26 (9-10) (1990) 1071–1098.

[9] M. P. F. Sutcliffe, N. A. Fleck, Microbuckle propagation in carbon fibre-epoxy composites, Acta Metallurgica et Materialia 42 (7) (1994) 2219–2231.

[10] N. A. Fleck, S. Sivashanker, M. P. F. Sutcliffe, Compressive failure of composites due to microbuckle growth, European Journal of Mechanics - A/Solids 16 (Special issue) (1997) 65–82.

[11] M. J. Laffan, S. T. Pinho, P. Robinson, A. J. McMillan, Translaminar fracture toughness: The critical notch tip radius of $0°$ plies in CFRP, Composites Science and Technology 72 (1) (2011) 97–102.

[12] M. J. Laffan, S. T. Pinho, P. Robinson, L. Iannucci, A. J. McMillan, Measurement of the fracture toughness associated with the longitudinal fibre compressive failure mode of laminated composites, Composites Part A: Applied Science and Manufacturing 43 (11) (2012) 1930–1938.

[13] J. H. Ahn, A. M. Waas, Prediction of compressive failure in laminated composites at room and elevated temperature, AIAA journal 40 (2) (2002) 346–358.

[14] P. Davidson, E. J. Pineda, C. Heinrich, A. M. Waas, A Unified Model for Predicting the Open Hole Tensile and Compressive Strengths of Composite Laminates for Aerospace Applications, in: 54th AIAA/ASME/ASCE/AHS/ASC Structures, Structural Dynamics, and Materials Conference, 2013, pp. 1–26.

[15] N. L. Hancox, The compression strength of unidirectional carbon fibre reinforced plastic, Journal of Materials Science 10 (2) (1975) 234–242.

[16] J. L. Wind, S. Steffensen, H. M. Jensen, Comparison of a composite model and an individually fiber and matrix discretized model for kink band formation, International Journal of Non-Linear Mechanics DOI: 10.1016/j.ijnonlinmec.2014.10.005.

[17] E. Riks, An Incremental Approach to the Solution of Snapping and Buckling Problems, International Journal of Solids and Structures 15 (7) (1979) 529–551.

[18] P. Prabhakar, A. M. Waas, Interaction between kinking and splitting in the compressive failure of unidirectional fiber reinforced laminated composites, Composite Structures 98 (2013) 85–92.

[19] J. R. Rice, A path independent integral and the approximate analysis of strain concentration by notches and cracks, Journal of Applied Mechanics 35 (1968) 379–386.

[20] P. C. Paris, G. C. Sih, Stress analysis of cracks, Fracture Toughness Testing and its Applications, ASTM STP 381 (1) (1964) 30 – 82.